

Modeling of atomic layer deposition on nanoparticle agglomerates

Jin, Wenjie

DOI

[10.4233/uuid:989257c4-0001-4f57-ad78-08f1180def7b](https://doi.org/10.4233/uuid:989257c4-0001-4f57-ad78-08f1180def7b)

Publication date

2017

Document Version

Final published version

Citation (APA)

Jin, W. (2017). *Modeling of atomic layer deposition on nanoparticle agglomerates*. [Dissertation (TU Delft), Delft University of Technology]. <https://doi.org/10.4233/uuid:989257c4-0001-4f57-ad78-08f1180def7b>

Important note

To cite this publication, please use the final published version (if applicable).
Please check the document version above.

Copyright

Other than for strictly personal use, it is not permitted to download, forward or distribute the text or part of it, without the consent of the author(s) and/or copyright holder(s), unless the work is under an open content license such as Creative Commons.

Takedown policy

Please contact us and provide details if you believe this document breaches copyrights.
We will remove access to the work immediately and investigate your claim.

MODELING OF ATOMIC LAYER DEPOSITION ON NANOPARTICLE AGGLOMERATES



Propositions

accompanying the dissertation

MODELING OF ATOMIC LAYER DEPOSITION ON NANOPARTICLE AGGLOMERATES

by

Wenjie JIN

1. The ALD saturation time of large nanoparticle agglomerates with fractal dimension D_f scales with the number of particles N as $N^{\frac{D_f-1}{D_f}}$.
This thesis
2. The ALD saturation time of a nanoparticle agglomerate is governed by four different time scales, the relative magnitudes of which depend on the agglomerate size and its fractal dimension.
This thesis
3. Due to the neglect of the diffusion time scale, Gordon's model for ALD coating of narrow pores exhibits incorrect asymptotic behavior for very low active surface site concentrations.
Chem. Vap. Deposition **9**, 73 (2003)
4. The statement by Sorenson that any proper expression for the scaling of fractal aggregate mobility with aggregate size N must exhibit correct $N = 1$ limit is incorrect.
Aerosol Sci. Technol. **45**, 765 (2011)
5. The porosity of a fractal agglomerate cannot be defined.
6. Humans can learn creativity from artificial intelligence.
7. Open source is the most promising direction for operating system software development.
8. A large population is an important driving force for the economy of a country.
9. The main challenge in future education is to bridge the growing gap between human knowledge and the knowledge of a new born baby.
10. Regular supply of pie and cake to a research group will boost its scientific productivity.

These propositions are regarded as opposable and defensible, and have been approved as such by the promoters, prof. dr. ir. C. R. Kleijn and prof. dr. ir. J. R. van Ommen.

Stellingen

behorende bij het proefschrift

MODELING OF ATOMIC LAYER DEPOSITION ON NANOPARTICLE AGGLOMERATES

door

Wenjie JIN

1. De ALD-verzadigingstijd van grote agglomeraten met fractale dimensie D_f schaalt met het aantal deeltjes N als $N^{\frac{D_f-1}{D_f}}$. *Dit proefschrift*
2. De ALD-verzadigingstijd van een agglomeraat van nanodeeltjes wordt bepaald door vier verschillende tijdsschalen, waarvan de relatieve grootte afhankelijk is van de afmetingen en de fractale dimensie van het agglomeraat. *Dit proefschrift*
3. Omdat in het model van Gordon de diffusie-tijdschaal is verwaarloosd, vertoont dit model voor ALD coating van nauwe gaten incorrect asymptotisch gedrag in het geval van zeer lage concentraties actieve oppervlaktesites.
Chem. Vap. Deposition **9**, 73 (2003)
4. De stelling van Sorenson dat iedere regel voor de schaling van de mobiliteit van een agglomeraat met de grootte N van dat agglomeraat de correcte $N = 1$ limiet moet vertonen is incorrect. *Aerosol Sci. Technol.* **45**, 765 (2011)
5. De porositeit van een fractaal agglomeraat kan niet worden gedefinieerd.
6. Mensen kunnen creatieve vaardigheden leren van artificiële intelligentie.
7. Open-source is de meest veelbelovende richting voor de ontwikkeling van besturingssystemen.
8. Een grote bevolking is een belangrijke drijvende kracht voor de economische ontwikkeling van een land.
9. De voornaamste uitdaging voor toekomstig onderwijs betreft het dichten van de groeiende kloof tussen de menselijke kennis, en de kennis van een pasgeborene.
10. Een frequente aanvoer van cake en taart aan een onderzoeksgroep verhoogt de wetenschappelijke productiviteit.

Deze stellingen worden oponeerbaar en verdedigbaar geacht en zijn als zodanig goedgekeurd door de promotoren prof. dr. ir. C. R. Kleijn en prof. dr. ir. J. R. van Ommen.

MODELING OF ATOMIC LAYER DEPOSITION ON NANOPARTICLE AGGLOMERATES

Proefschrift

ter verkrijging van de graad van doctor

aan de Technische Universiteit Delft,

op gezag van de Rector Magnificus prof. ir. K.C.A.M. Luyben,

voorzitter van het College voor Promoties,

in het openbaar te verdedigen op woensdag 29 november 2017 om 10:00 uur

door

Wenjie JIN

Mechanical Engineer
Tsinghua University, China
geboren te Yanji, China

This dissertation has been approved by the

promotor: Prof. dr. ir. Chris R. Kleijn
copromotor: Prof. dr. ir. J. Ruud van Ommen

Composition of the doctoral committee:

Rector Magnificus,
Prof. dr. ir. Chris R. Kleijn
Prof. dr. ir. J. Ruud van Ommen

chairman
Technische Universiteit Delft
Technische Universiteit Delft

Independent members:

Prof. dr. ir. Michiel T. Kreutzer
Prof. dr. ir. Andreas Schmidt-Ott
Prof. dr. Christophe Detavernier
Dr. ir. Arjan J. H. Frijns
Dr. ir. Johan T. Padding
Prof. dr. Robert F. Mudde

Technische Universiteit Delft
Technische Universiteit Delft
Ghent University
Technische Universiteit Eindhoven
Technische Universiteit Delft
Technische Universiteit Delft, reservellid

This work was carried out within the framework of the NanoNextNL.

Copyright © 2017 by Wenjie Jin

ISBN 978-94-6186-866-4

All rights reserved. Parts of this thesis are published in scientific journals and copyright is subjected to different terms and conditions.

*To know what you know and what you do not know,
that is true knowledge.*

Confucius



CONTENTS

Summary	xi
1 Introduction	1
1.1 Nanoparticles and Surface Modification	2
1.2 Atomic Layer Deposition	2
1.3 Fluidization	3
1.3.1 Agglomerates	3
1.4 Modeling and Simulations	5
1.4.1 Gas Rarefaction	6
1.4.2 Numerically Generated Agglomerates	6
1.5 Research Objective	7
1.6 Outline	8
1.7 Funding of This PhD Thesis	9
References	9
2 Numerical method	13
2.1 DSMC Method	14
2.1.1 Overview	14
2.1.2 OpenFoam DSMC	15
2.1.3 Initialization	15
2.1.4 Parcel Movement	16

2.1.5	Parcel Collisions	18
2.1.6	Validation of ALD reaction model	19
2.2	Tunable Algorithms for Generating Fractal Agglomerates	23
2.2.1	Sequential Algorithm	24
2.2.2	Cluster-cluster Aggregation Algorithm	25
2.2.3	Intrinsic Randomness and Discontinuity at Small N	26
	References	27
3	A new cut-cell algorithm for DSMC simulations of rarefied gas flows around immersed moving objects	31
3.1	Introduction	32
3.2	Cut-cell algorithm in DSMC.	34
3.2.1	Overlap volume computation algorithm	35
3.3	Validation with drag computation.	38
3.3.1	Computational setup	38
3.3.2	Kn dependence	39
3.3.3	Comparison with body-fitted mesh DSMC.	40
3.3.4	Stationary and moving sphere with immersed boundaries.	42
3.4	Conclusion	43
	References	44
4	Simulation of atomic layer deposition on nanoparticle agglomerates	47
4.1	Introduction	48
4.1.1	Numerical construction of fractal agglomerates	49
4.1.2	Direct Simulation Monte Carlo.	50
4.1.3	Modeling ALD surface reaction	50

4.2	Computational Setup	51
4.3	Results and Discussions.	52
4.3.1	Influence of Pressure on coating time	52
4.3.2	Influence of agglomerate size on coating time	55
4.3.3	Influence of fractal dimension on coating time	59
4.4	Summary and conclusions	60
	References	61
5	Moving Reaction Fronts in Fractal Nanoparticle Agglomerates	67
5.1	Introduction	68
5.2	Theory	69
5.3	Simulations	73
5.4	Conclusion	77
	References	79
	Appendices	83
5.A	Simplification of Expressions for t_F and t_M	83
5.B	Influence of the relaxation of the particle attachment criteria.	84
5.C	Influence of the sticking coefficient	84
5.D	Evolution of surface coverage in time	86
6	Conclusions and Outlook	89
6.1	Conclusions.	90
6.2	Opportunities for future research	91
6.2.1	First Order Reaction on Fractals in Rarefied Gas Regime	91
6.2.2	Agglomerate movement in a gas flow	92

6.2.3	Dynamic agglomeration	93
6.2.4	Polydisperse Nanoparticles	94
	References	95
	List of Publications	97
	Acknowledgements	99
	Curriculum Vitæ	101

SUMMARY

Nanoparticles are increasingly applied in a range of fields, such as electronics, catalysis, energy and medicine, due to their small sizes and consequent high surface-volume ratio. In many applications, it is attractive to coat the nanoparticles with a layer of different materials in order to gain new functionalities. For instance, a coated layer can modify the chemical properties of the nanoparticles, protect the core material resulting in increased stability, facilitate the biofunctionalization, etc.

Atomic layer deposition (ALD) is a gas-phase technique that can form an ultrathin solid film on a range of substrates. It utilizes two self-limiting surface reactions applied in an alternating sequence. By controlling the number of applied cycles, the thickness of the coated layer can be controlled with nanometer precision. Several experimental reports in literature have shown that applying ALD to nanoparticles using a fluidized bed is a promising way of producing large quantities of coated nanoparticles. Fluidization is a gas-phase technique that can process large quantities of particles by suspending them in an upward gas stream. It provides good gas-solid mixing, scale-up potential, and allows continuous processing.

However, due to the strong cohesive forces between particles, nanoparticles cluster into large agglomerates when fluidized. These agglomerates have a complex, hierarchical structure, which has been commonly described as fractal for their self-similarity under different length scales. During the ALD process, the precursors have to diffuse into such structures to reach the surface of inner particles.

In this thesis we focus on the influence of nanoparticle agglomerate structures on the ALD coating process. We use numerical simulations as the main tool to study the ALD coating on different nanoparticle agglomerates, and we have developed theoretical models which predict the scaling of ALD coating time of nanoparticle agglomerates based on the fractal characteristics of these agglomerates.

We first developed and implemented a new cut-cell method in conjunction with direct simulation Monte Carlo (DSMC) method, which allows simulating rarefied gas flows that physically and chemically interact with immersed nanoparticles. We have validated this new method by computing the drag force on a (moving) sphere, and the results agree very well with analytical solutions found in literature.

Using this new method, we have simulated ALD on fractal nanoparticle agglomer-

ates, consisting of up to 10^4 mono-sized nanoparticles. Our simulations account for a self-limiting ALD half cycle reaction, gas diffusion in the gas rarefied regime, and fully resolved fractal nanoparticle agglomerates. Based on these simulations, we studied the influence of the gas pressure, agglomerate size and fractal dimension on the overall coating time.

We also developed a theoretical model for nanoparticle agglomerate ALD coating times, by deriving a generalized form of an earlier model from literature, which was originally proposed by Gordon and coworkers (2003) for ALD coating within a simple cylindrical hole or trench. Our model predicts the ALD coating time within fractal agglomerates, with two model constants. By comparing the model predictions with our simulation results, we found good agreements in general, while some deviations are observed for lower fractal dimensions.

Based on this model, we took a step further to develop a closed form theory, showing the scaling of the coating time, due to the interplay between Knudsen diffusion and self-limiting gas-surface reactions. This model takes three main features of a fractal agglomerate as input, viz. its fractal dimension, its gyration radius and the diameter of the constituting nanoparticles. We identified four main time scales that contribute to the overall coating time, and came up with a regime map that teaches the scaling behavior of the coating time for different combinations of number of particle and fractal dimensions. We again validated this model with our simulation results and found good agreement for all the studied cases.

Finally, we conclude this thesis with a summary of our main findings and a discussion of how our findings can be of use for the future research.

SAMENVATTING

Dankzij hun kleine formaat en grote oppervlakte-volume ratio zijn de toepassingsmogelijkheden van nanodeeltjes groot en groeiende, in bijvoorbeeld elektronica, katalyse, energie en farmaceutica. Het coaten van nanodeeltjes met een dunne laag van een ander materiaal biedt mogelijkheden om het palet aan functionaliteiten van nanodeeltjes uit te breiden. Een voorbeeld hiervan is het aanbrengen van een coating die de chemische eigenschappen van de deeltjes verandert, om het kernmateriaal te beschermen, de stabiliteit van het materiaal te vergroten, of afstoting door het menselijk lichaam te voorkómen.

Atomic Layer Deposition (ALD) is een techniek om ultradunne lagen materiaal op een substraat aan te brengen middels depositie van atomen of moleculen vanuit de gasfase. Door twee zelflimiterende oppervlaktereacties te alterneren kan de laagdikte met nanometer-precisie worden geregeld. Een gefluïdiseerd bed is een reactortype waarin een grote hoeveelheid deeltjes kan worden bewerkt door ze in de gasfase te suspenderen. Meerdere experimentele studies hebben reeds laten zien dat de toepassing van ALD in een gefluïdiseerd bed een veelbelovende methode is om grote hoeveelheden gecoate nanodeeltjes te produceren. Een dergelijke aanpak zorgt voor een uitstekende menging van de vaste- en de gasfase, is relatief eenvoudig op te schalen, en is toepasbaar als continu proces.

De sterke cohesiekrachten tussen de nanodeeltjes zorgen echter in een gefluïdiseerde reactor voor het clusteren van die deeltjes tot grote agglomeraten. Deze agglomeraten hebben complexe hiërarchische structuren, die, vanwege hun zelfgelijkende structuren op verschillende lengteschalen, typisch worden beschreven als fractalen. Gedurende het coatingproces moeten ALD-precursormoleculen deze agglomeraten in diffunderen, om de oppervlakten van de meest centrale deeltjes te kunnen bereiken.

In dit proefschrift bestuderen we de invloed van de geometrische structuur en de grootte van een agglomeraat op de karakteristieke tijdschalen in het ALD-proces, dat wil zeggen de tijdschaal die benodigd is om alle deeltjes in het agglomeraat van een coating te voorzien. We gebruiken numerieke simulaties als de voornaamste methode om het coatingproces voor verschillende agglomeraatstructuren in kaart te brengen. Op basis hiervan zijn theoretische schalingsregels ontwikkeld die de coatingtijd van agglomeraten voorspellen als functie van hun grootte en fractale structuur.

Allereerst hebben we een nieuwe cut-cell methode ontwikkeld die het mogelijk maakt

om, wanneer gecombineerd met de Direct Simulation Monte-Carlo (DSMC) techniek, de (chemische) interactie tussen ijle gassen en nanodeeltjes te simuleren. Deze methode is met succes gevalideerd door het bepalen van de wrijvingskracht op een bewegend bolvormig deeltje.

Met deze nieuwe methode is vervolgens het ALD-proces voor fractale agglomeraten gesimuleerd. De bestudeerde agglomeraten bestonden uit maximaal 10^4 bolvormige nanodeeltjes met gelijke diameter. Onze simulaties zijn gebaseerd op een volledige geometrische beschrijving van de agglomeraten, en modelleren een zelflimiterende ALD-halfreactie in combinatie met ijle gasdiffusie. De simulaties zijn gebruikt om de invloed van de gasdruk, het formaat en de fractale dimensie van agglomeraten op de coatingtijd te bestuderen.

Verder hebben we, op basis van een gegeneraliseerde vorm van een eerder door Gordon et al. (2003) gepubliceerd model voor ALD coatingprocessen in een cilindrische porie, een theoretisch model ontwikkeld om de ALD coatingtijd van fractale agglomeraten van nanodeeltjes te voorspellen. Dit model bevat twee modelconstanten. We observeren een goede overeenkomst tussen numerieke simulaties en modelvoorspellingen, al zijn er afwijkingen te zien voor lage fractale dimensies.

Bovengenoemd model vormde de basis voor een verdere theoretische ontwikkeling richting een volledig gesloten model, waarin de schaling van de coatingtijd wordt gebaseerd op de wisselwerking tussen Knudsen-diffusie en zelflimiterende oppervlaktereacties. Dit model neemt de drie voornaamste geometrische aspecten van een agglomeraat als basis, d.w.z. de fractale dimensie en de omwentelingsstraal van het agglomeraat, en de diameter van de nanodeeltjes waaruit het agglomeraat is opgebouwd. Vier relevante tijdschalen die bijdragen aan de coatingtijd zijn geïdentificeerd op basis van dit model; de verschillende schalingsregimes voor de coatingtijd konden hiermee in een regime-map worden weergegeven. Deze regime-indeling is door middel van numerieke simulaties succesvol gevalideerd.

Tot slot presenteren we in dit proefschrift een samenvatting van de gevonden resultaten, tezamen met een discussie betreffende de implicaties van dit werk voor vervolgonderzoek.

1

INTRODUCTION

1.1. NANOPARTICLES AND SURFACE MODIFICATION

Nanoparticles have, by definition, all three dimensions under 100 nm. Due to the special properties arising from their small sizes, e.g. high surface to volume ratio, nanoparticles are widely applied in many fields, such as catalysis, medicine, energy and electronics [1–6]. The production of nanoparticles can generally fall into three categories: (i) condensation from vapor, (ii) synthesis by chemical reaction, and (iii) solid-state processes such as milling [7]. After production, nanoparticles often require certain surface modifications to achieve additional functionalities required for particular end applications. For instance, in biomedical applications the drug nanoparticles can be coated with a selective material that exclusively attaches to specific cell surface, thus achieving targeted drug delivery [8]. In electronics, coating ceramic nanoparticles with a thin polymer layer increases the dielectric constant compared to the pure polymer [9, 10]. These two examples, among many others, show the importance of the surface modification on nanoparticles.

1.2. ATOMIC LAYER DEPOSITION

Atomic layer deposition (ALD) is one such method that can modify the nanoparticle surface by coating a thin film layer on the surface [12]. Figure 1.1 shows a TEM image of one ALD coated nanoparticle [11]. ALD is a gas-phase coating technique originating from the semi-conductor industry, and is well known for its high precision, conformality and controllability. It utilizes two different precursors, *A* and *B*, that react with the substrate surface in an alternating sequence. Both reactions are self-limiting, meaning that no more reaction can take place when all the available surface sites have been occupied. During an ALD process, precursor *A* is first introduced to the system, and reacts with the substrate surface until it is fully saturated. Then the excess *A* is purged out with an inert

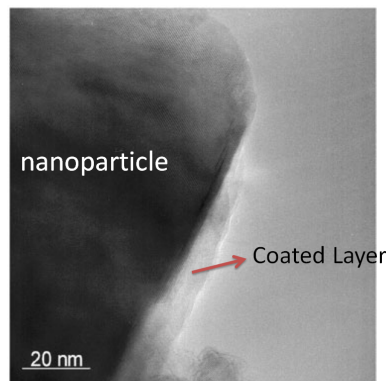


Figure 1.1: TEM image of a coated nanoparticle [11].

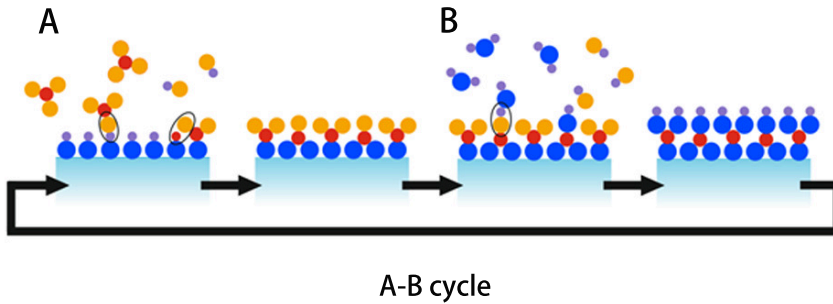


Figure 1.2: Schematic representation of ALD A-B cycle.

gas such as nitrogen. After that, precursor *B* is introduced and reacts to the surface and makes it again reactive to *A*. The final layer thickness can be precisely controlled by the number of cycles applied in this process. Figure 1.2 illustrates this process with simple schematics.

1.3. FLUIDIZATION

Fluidization is a widely applied technique for processing large quantities of particles [13]. In a fluidized bed, particles are suspended in an upward gas stream and exhibit a fluid-like behavior as the name fluidization implies. The dynamic movements of particles result in a good solid-gas mixing which is beneficial for many gas-phase processes including ALD. However, not all particles can be fluidized and this has been summarized in Geldart's diagram which is based on the particle size and gas-solid density difference [14]. As shown in Fig 1.3, this diagram suggests that nanoparticles belong to the group C and thus are impossible to fluidize. However, many experiments [15–17] have shown that nanoparticles can be fluidized, with two different types: bubbling and homogeneous fluidization.

1.3.1. AGGLOMERATES

The main reason for this contradiction to Geldart's diagram is that nanoparticles in a fluidized bed form large agglomerates, due to the strong cohesive interparticle forces such as the van der Waals forces. Therefore, in a fluidized bed nanoparticles are suspended as large agglomerates instead of single particles. Wang et al. [18] first presented TEM and SEM images of agglomerates sampled from a fluidized bed. As shown in Fig 1.4, the nanoparticles first form complex netlike structures, which then form simple agglomerates of several tens of microns. Again, the simple agglomerates aggregate and form large

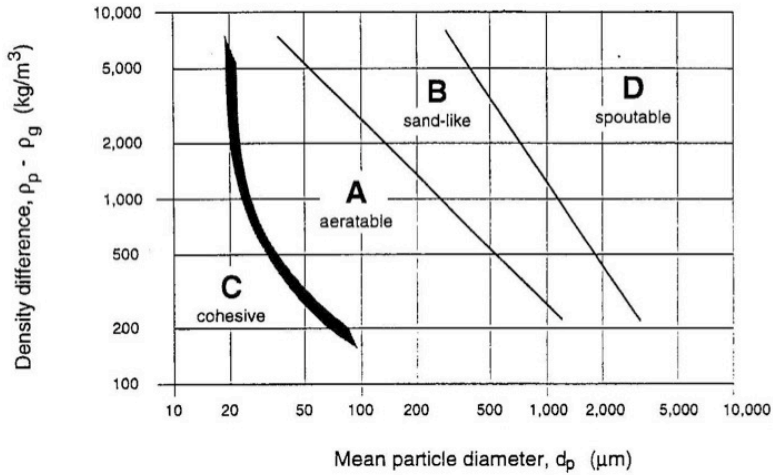


Figure 1.3: Gerdart's classification of fluidization behavior of fine particles, adopted from [14]

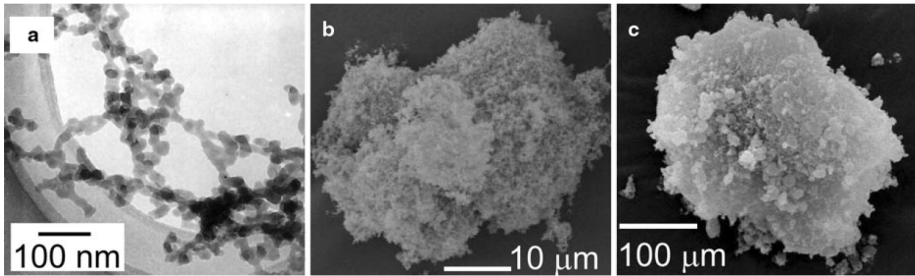


Figure 1.4: Structure of agglomerates at different length scales [18].

agglomerates that are larger than $100 \mu\text{m}$. This suggests that agglomerates in a fluidized bed have hierarchical complex structures over a broad span of length scales.

After the introduction by Mandelbrot in 1975 [19], the concept of fractal geometry has been widely used to study nanoparticle agglomerates [20–22]. By definition, a fractal structure has self-similarity under different length scales, which is also called scale invariance. This concept enables us to quantify an agglomerate structure as following:

$$N = k_f \left(\frac{R_g}{a} \right)^{D_f} \quad (1.1)$$

where N is the number of nanoparticles in an agglomerate, k_f is an $O(1)$ constant, R_g is the gyration radius of the agglomerate, a is the primary particle radius, and D_f is the fractal dimension which indicates how the mass of an agglomerate scales against its size. Note that real nanoparticle agglomerates do not exactly but statistically fulfill Eq. (1.1),

and therefore they are often called fractal-like agglomerates.

Experimental studies on fluidization of nanoparticle agglomerates so far have mainly focused on determining the agglomerate size and fractal dimension. There are ex-situ measurements with sampled agglomerates [18, 23], as well as in-situ measurements based on settling agglomerates [20, 24], splash zone recording [21, 25], X-ray micro-tomography [26] and so on. However, there is relatively large scatter among the reported results due to the different methods and operating conditions. Thus a consensus on the agglomerate size or structure has not been achieved. Even less is known about the detailed mechanism of how the fluidization properties affect the agglomerate size and structure.

In order to apply ALD on large quantities of nanoparticles in a fluidized bed reactor, it is important to study the influence of agglomerates on the mass transfer and precursor utilization efficiency. The large agglomerates determine (1) how many nanoparticles are directly exposed to the precursors and (2) the time required for the precursor molecules to diffuse into the structures to meet the inner nanoparticles. Moreover, these agglomerates undergo a dynamic process of breakup and re-agglomeration, which makes the problem more difficult to understand.

1.4. MODELING AND SIMULATIONS

Computational modeling and simulations are powerful tools for gaining new insights in this problem. Different methods have been developed for simulating fluidized beds [27]. The most important methods are categorized in Table 1.1, based on the different approaches to the gas and solid phase. The Eulerian approach models the phase as continuum fluid despite the discrete nature of the particles (solid phase) or molecules (gas phase). On the other hand, the Lagrangian approach explicitly tracks the trajectories of the discrete particles, molecules or gas bubbles. By different combination of these two approaches, each simulation method can resolve down to a certain length scale, beyond which it requires a closure from smaller scale models that take into account detailed gas-solid interactions. For instance, the two-fluid model treats both gas and solid as a continuum fluid, and takes the drag exerted by particles with different volume fractions as closure to the governing equations.

Name	Gas phase	Solid phase	Scale
Discrete bubble model	Lagrangian	Eulerian	Industrial (10 m)
Two-fluid model	Eulerian	Eulerian	Engineering (1 m)
Discrete particle model	Eulerian	Lagrangian	Laboratory (0.1 m)
Particle based method	Lagrangian	Lagrangian	Mesoscopic (< 0.001 m)

Table 1.1: Summary of different simulation methods used for gas fluidization [27].

In the literature of nanoparticle fluidization, almost all the modeling and simula-

tions are performed with the Eulerian–Lagrangian approach. However, they do not resolve down to the scale of individual nanoparticles, but rather model entire agglomerates as perfect spheres with fixed diameter [28–31]. Therefore, the simulated systems become essentially identical to that of micron sized particles. This is the main limitation of the previous approaches, as they cannot take into account the detailed complex fractal structures of individual agglomerates, despite that this information is crucial for the ALD process as explained earlier.

1.4.1. GAS RAREFACTION

One important issue for simulations resolving down to the individual nanoparticle, is the gas rarefaction. A fluid is regarded as a continuous medium if the smallest significant volume includes a sufficient number of molecules. Then macroscopic properties can be obtained from the average of molecular properties at any location of the fluid [32]. The conservation of mass, momentum and energy together with constitutive equations for shear, stress and heat flux, such as Navier-Stokes equations, yield a numerical solution for the flow fields. However, immersed nanoparticles, with sizes less than 100 nm, introduce a length scale that is small enough to change this situation, as the mean free path in a gas at atmospheric pressure and temperature is $O(100)$ nm, and is even larger at reduced pressures and elevated temperatures. More precisely, when the Knudsen number $Kn = \frac{\lambda}{L} > 0.1$, where λ is the molecular mean free path and L is the relevant length scale, the transport terms in Navier-Stokes equations fail and thus the gas phase should be modeled as discrete molecules instead of a continuous medium. Therefore, a Lagrangian-Lagrangian approach becomes necessary in this regime.

Direct simulation Monte Carlo (DSMC) [33] is one such method that simulates rarefied gas flow by tracking the movements of individual (quasi) molecules. It is a well-developed and widely applied technique for simulating rarefied gas flows, such as in outer atmosphere aerospace applications [34] and in microscale gas flow devices [35, 36]. Detailed description about this method and its implementation is provided in Chapter 2.

1.4.2. NUMERICALLY GENERATED AGGLOMERATES

By including many nanoparticles in a DSMC simulation of rarefied gas flow, accounting for correct inter-particle cohesive forces, it is possible to simulate the formation of realistic agglomerates. However, to the best of our knowledge, such simulations are not performed yet in literature, probably due to the high complexity and computational cost.

Alternatively, agglomerate formation can be mimicked by modeling the movement of particles, in the absence of gas flow [37]. For instance, one can simulate the particles with diffusive or ballistic movements, and let the particles collide to form agglom-

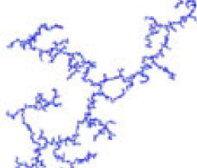
	Reaction-limited	Ballistic	Diffusion-limited
Particle-cluster	 $D_f = 3.00$	 $D_f = 3.00$	 $D_f = 2.50$
Cluster-cluster	 $D_f = 2.09$	 $D_f = 1.95$	 $D_f = 1.80$

Figure 1.5: Agglomerates generated by different mechanism [37].

erates. Upon collision, a permanent bond is formed between the two particles with a preset probability. Depending on this probability, these numerically generated agglomerates can be categorized into two classes: diffusion limited and reaction limited. Also, in such simulations, agglomerates can be generated starting from either a single particle or from a number of movable clustered particles, which are called the particle-cluster and cluster-cluster classes respectively. Figure 1.5 shows the agglomerates generated from various methods and their fractal dimension D_f . Since all these agglomerates are generated based on certain assumptions, including the motion of the particles, how closely they are related to the actual agglomerates in a fluidized bed still remains as a question.

Another way of generating agglomerates is the so-called tunable numerical generation method, which generates agglomerates with any prescribed D_f and k_f [38, 39]. In contrast to the above mimicking method, this tunable algorithm assumes that the fractal scaling law is exactly fulfilled for any size of the agglomerate and therefore directly imposes the fractal scaling law [Eq. (1.1)] when aggregating particles. More details about this tunable method are provided in Chapter 2.

1.5. RESEARCH OBJECTIVE

As discussed before, nanoparticle fluidization is feasible by virtue of the agglomeration of the particles. The time required to completely coat an agglomerate by ALD strongly depends on the agglomerate size and morphology due to the distribution of the reactive

surfaces and the time required for the precursor molecules to diffuse into the agglomerate. The objective of this thesis is to understand by which factors and to which extent the ALD coating time of nanoparticle agglomerates is determined.

We use numerical simulations as the main tool to study this problem. For this, the DSMC method is chosen as it is the most flexible method capable of handling the aforementioned gas rarefaction effect. Since currently no DSMC code is available that can handle the presence of moving agglomerated nanoparticles immersed in the rarefied gas, the first step in this work is to investigate new numerical algorithms within the DSMC framework which enable such simulations. This leads to our first research question:

1. Can we model the physical and chemical interaction between gas molecules and arbitrarily shaped nanoparticles moving in a rarefied gas flow using a DSMC framework?

Using the developed DSMC simulation framework, we will subsequently address the following two research questions:

2. How do the fractal structure (size and fractal dimension) and the operation regime (pressure) influence the ALD coating time of an agglomerate?
3. Can we derive scaling relations for the ALD coating time of fractal nanoparticle agglomerates as a function of their size and structural characteristics?

1.6. OUTLINE

This thesis consists of six chapters. Following this introduction chapter, Chapter 2 provides relevant details about the numerical methods, as these are only briefly recaptured in the subsequent chapters. Chapter 3 addresses the first research question by demonstrating the implementation of an immersed boundary method within a DSMC code, allowing for the simulations of rarefied gas drag on an arbitrarily shaped moving object. Chapter 4 addresses the second research question with a detailed parameter study on the ALD coating time of static nanoparticle agglomerates. It also presents our first attempt on quantitative prediction of the ALD coating time. Chapter 5 further improves the theoretical model proposed in Chapter 4 and validates it with extensive simulations with various differently generated agglomerates, which addresses the third research question. Finally, Chapter 6 gives our main conclusions and discusses the opportunities for future research.

1.7. FUNDING OF THIS PHD THESIS

This work was supported by NanoNextNL, a micro and nanotechnology consortium of the government of the Netherlands and 130 partners.

REFERENCES

- [1] J. Li, X. Liang, D. M. King, Y.-B. Jiang, and A. W. Weimer, *Highly dispersed Pt nanoparticle catalyst prepared by atomic layer deposition*, *Applied Catalysis B: Environmental* **97**, 220 (2010).
- [2] S. Xuan, Y.-X. J. Wang, J. C. Yu, and K. C. Leung, *Preparation, Characterization, and Catalytic Activity of Core/Shell Fe₃O₄@Polyaniline@Au Nanocomposites*, *Langmuir* **25**, 11835 (2009).
- [3] H. Yin, Z. Ma, M. Chi, and S. Dai, *Heterostructured catalysts prepared by dispersing Au@Fe₂O₃ core/shell structures on supports and their performance in CO oxidation*, *Catalysis Today* **160**, 87 (2011).
- [4] A. Goulas and J. R. van Ommen, *Scalable Production of Nanostructured Particles using Atomic Layer Deposition*, *KONA Powder and Particle Journal* **31**, 234 (2014).
- [5] W. E. Bawarski, E. Chidlow, D. J. Bharali, and S. A. Mousa, *Emerging nanopharmaceuticals*, *Nanomedicine: Nanotechnology, Biology and Medicine* **4**, 273 (2008).
- [6] J. W. Elam, N. P. Dasgupta, and F. B. Prinz, *ALD for clean energy conversion, utilization, and storage*, *MRS Bulletin* **36**, 899 (2011).
- [7] R. Ghosh Chaudhuri and S. Paria, *Core/Shell Nanoparticles: Classes, Properties, Synthesis Mechanisms, Characterization, and Applications*, *Chemical Reviews*, *Chem. Rev.* **112**, 2373 (2012).
- [8] S. Laurent, D. Forge, M. Port, A. Roch, C. Robic, L. Vander Elst, and R. N. Muller, *Magnetic Iron Oxide Nanoparticles: Synthesis, Stabilization, Vectorization, Physicochemical Characterizations, and Biological Applications*, *Chem. Rev.* **108**, 2064 (2008).
- [9] A. Maliakal, H. Katz, P. M. Cotts, S. Subramoney, and P. Mirau, *Inorganic Oxide Core, Polymer Shell Nanocomposite as a High K Gate Dielectric for Flexible Electronics Applications*, *J. Am. Chem. Soc.* **127**, 14655 (2005).
- [10] B. C. Das and A. J. Pal, *Core Shell Hybrid Nanoparticles with Functionalized Quantum Dots and Ionic Dyes: Growth, Monolayer Formation, and Electrical Bistability*, *ACS Nano* **2**, 1930 (2008).

- [11] R. Beetstra, U. Lafont, J. Nijenhuis, E. M. Kelder, and J. R. van Ommen, *Atmospheric Pressure Process for Coating Particles Using Atomic Layer Deposition*, *Chemical Vapor Deposition* **15**, 227 (2009).
- [12] S. M. George, *Atomic Layer Deposition: An Overview*, *Chemical Reviews*, *Chem. Rev.* **110**, 111 (2010).
- [13] M. Horio, *Fluidization science, its development and future*, *Particuology* **8**, 514 (2010).
- [14] D. Geldart, *Types of gas fluidization*, *Powder Technology* **7**, 285 (1973).
- [15] J. Chaouki, C. Chavarie, D. Klvana, and G. Pajonk, *Effect of interparticle forces on the hydrodynamic behaviour of fluidized aerogels*, *Powder Technology* **43**, 117 (1985).
- [16] J. Jung and D. Gidaspow, *Fluidization of Nano-size Particles*, *Journal of Nanoparticle Research*, **4**, 483 (2002).
- [17] C. Zhu, Q. Yu, R. N. Dave, and R. Pfeffer, *Gas fluidization characteristics of nanoparticle agglomerates*, *AIChE Journal* **51**, 426 (2005).
- [18] W. Yao, G. Guangsheng, W. Fei, and W. Jun, *Fluidization and agglomerate structure of SiO₂ nanoparticles*, *Powder Technology* **124**, 152 (2002).
- [19] B. B. Mandelbrot, *The fractal geometry of nature*, 1st ed. (W.H. Freeman, 1982).
- [20] J. M. Valverde, M. A. S. Quintanilla, A. Castellanos, and P. Mills, *The settling of fine cohesive powders*, *Europhysics Letters (EPL)* **54**, 329 (2001).
- [21] L. F. Hakim, J. L. Portman, M. D. Casper, and A. W. Weimer, *Aggregation behavior of nanoparticles in fluidized beds*, *Powder Technology* **160**, 149 (2005).
- [22] L. de Martín, A. Fabre, and J. R. van Ommen, *The fractal scaling of fluidized nanoparticle agglomerates*, *Chemical Engineering Science* **112**, 79 (2014).
- [23] C. H. Nam, R. Pfeffer, R. N. Dave, and S. Sundaresan, *Aerated vibrofluidization of silica nanoparticles*, *AIChE J.* **50**, 1776 (2004).
- [24] X. S. Wang, V. Palero, J. Soria, and M. J. Rhodes, *Laser-based planar imaging of nano-particle fluidization: Part II—mechanistic analysis of nanoparticle aggregation*, *Chemical Engineering Science* **61**, 8040 (2006).
- [25] J. M. Valverde, M. A. S. Quintanilla, A. Castellanos, D. Lepek, J. Quevedo, R. N. Dave, and R. Pfeffer, *Fluidization of fine and ultrafine particles using nitrogen and neon as fluidizing gases*, *AIChE J.* **54**, 86 (2008).
- [26] O. Gundogdu, P. M. Jenneson, and U. Tuzun, *Nano particle fluidisation in model 2-D and 3-D beds using high speed X-ray imaging and microtomography*, *Journal of Nanoparticle Research*, *Journal of Nanoparticle Research* **9**, 215 (2007).

- [27] M. A. van der Hoef, van Sint Annaland, N. G. Deen, and J. A. M. Kuipers, *Numerical Simulation of Dense Gas-Solid Fluidized Beds: A Multiscale Modeling Strategy*, Annual Review of Fluid Mechanics **40**, 47 (2008).
- [28] L. Huilin, W. Shuyan, Z. Jianxiang, D. Gidaspow, J. Ding, and L. Xiang, *Numerical simulation of flow behavior of agglomerates in gas-cohesive particles fluidized beds using agglomerates-based approach*, Chemical Engineering Science **65**, 1462 (2010).
- [29] S. Y. Wang, Y. R. He, H. L. Lu, J. X. Zheng, G. D. Liu, and Y. L. Ding, *Numerical Simulations of Flow Behaviour of Agglomerates of Nano-Size Particles in Bubbling and Spouted Beds with an Agglomerate-Based Approach*, Food and Bioproducts Processing **85**, 231 (2007).
- [30] X. S. Wang, F. Rahman, and M. J. Rhodes, *Application of discrete element method simulation for studying fluidization of nanoparticle agglomerates*, The Canadian Journal of Chemical Engineering **86**, 514 (2008).
- [31] D. Liu, B. G. M. van Wachem, R. F. Mudde, X. Chen, and J. R. van Ommen, *An adhesive CFD-DEM model for simulating nanoparticle agglomerate fluidization*, AIChE Journal **62**, 2259 (2016).
- [32] G. A. Bird, *Recent advances and current challenges for DSMC*, Computers & Mathematics with Applications **35**, 1 (1998).
- [33] G. A. Bird, *Molecular gas dynamics and the direct simulation of gas flows*, 2nd ed. (Clarendon Press, 2003).
- [34] E. S. Oran, C. K. Oh, and B. Z. Cybyk, *DIRECT SIMULATION MONTE CARLO: Recent Advances and Applications*, Annual Review of Fluid Mechanics **30**, 403 (1998).
- [35] Z. C. Hong, C. E. Zhen, and C. Y. Yang, *Fluid Dynamics and Heat Transfer Analysis of Three Dimensional Microchannel Flows with Microstructures*, Numerical Heat Transfer, Part A: Applications **54**, 293 (2008).
- [36] H. Akhlaghi, E. Roohi, and S. Stefanov, *A new iterative wall heat flux specifying technique in DSMC for heating/cooling simulations of MEMS/NEMS*, International Journal of Thermal Sciences **59**, 111 (2012).
- [37] S. K. Friedlander, *Smoke, dust, and haze : fundamentals of aerosol behavior* (Wiley, 1977).
- [38] A. V. Filippov, M. Zurita, and D. E. Rosner, *Fractal-like Aggregates: Relation between Morphology and Physical Properties*, Journal of Colloid and Interface Science **229**, 261 (2000).
- [39] K. Skorupski, J. Mroccka, T. Wriedt, and N. Riefler, *A fast and accurate implementation of tunable algorithms used for generation of fractal-like aggregate models*, Physica A: Statistical Mechanics and its Applications **404**, 106 (2014).



2

NUMERICAL METHOD

2.1. DSMC METHOD

2.1.1. OVERVIEW

2

As described in Chapter 1, the gas rarefaction effect becomes important at small length scales involved in the case of nanoparticle agglomerates. Direct Simulation Monte Carlo (DSMC) [1] is the most commonly applied technique for simulating rarefied gas flows where conventional continuum flow solvers are not applicable. Originated from the kinetic theory of gases [2], it computes the flow by tracking a large number of simulated parcels, including their inter-collisions, with each parcel representing a usually very large number of real gas molecules. Therefore, a real flow of gas molecules is simulated with a much smaller number ($O(10^5 - 10^8)$) set of parcels which is still sufficiently large to statistically capture the flow physics. One essential assumption of DSMC is the decoupling between the molecular movement and molecular collision over a time interval that is small compared to the molecular mean collision time. In each DSMC time step, the computed parcels first undergo ballistic movement, and then exchange momentum and energy with nearby parcels. The computation of the parcel movement is deterministic, based on the current velocity and position, whereas the collision step is stochastic in both pair selection and momentum and energy exchange.

In DSMC, the computational domain is divided into a number of grid cells, wherein the parcel collision partners are selected, collisions are computed, and flow properties are sampled. More precisely, the collision pairs are selected among the parcels within each cell and the flow properties are sampled over all the parcels in each cell. Although in principle one can have two distinct sets of grid cells each serving the two purposes, usually one set is sufficient and thus it determines the space resolution for both cases.

This discretization in time and space introduces errors since in reality both time and space are continuous. In order to ensure that errors are within an acceptable range, DSMC requires both time step Δt and grid size Δx to be sufficiently small. As a general rule of thumb, Δt and Δx should fulfill $\Delta t < \frac{1}{8}\lambda/c_m$ and $\Delta x < \frac{1}{3}\lambda$, where λ is the gas mean free path and c_m is the molecular mean thermal velocity [3, 4]. Another source of the error is introduced by the fact that a usually very large number of molecules in a cell is represented by a small number of parcels. Since the entire spectrum of the molecular states is represented by a few parcels, the high energy states may be completely neglected due to their low probability of occurrence. Thus it has been suggested that a cell should contain on average at least $N = 10$ parcels in order to achieve a well resolved DSMC simulation [4]. Finally, it has been proven that when, for $\Delta t \rightarrow 0$, $\Delta x \rightarrow 0$ and $N \rightarrow \infty$, these errors approach to 0, the solution of DSMC converges to that of the Boltzmann equation [5].

2.1.2. OPENFOAM DSMC

In this work, we have used the software package OpenFOAM. OpenFOAM is an open source computational fluid dynamics (CFD) toolbox written in C++, and it provides a DSMC solver called `dsmcFoam` which has been extensively validated against multiple benchmark tests [6]. The main features that distinguish it from other available DSMC codes are the arbitrary 3D geometry and the unlimited parallel processing capability. In a parallel process, the computational domain is divided into a number of subdomains, with each of them assigned to a different processor. At each time step, each processor only takes care of the DSMC parcels that are contained in its subdomain, and hands over the parcels that end up in another subdomain (after the streaming step) to the corresponding processor with the standard Message Passing Interface (MPI). Therefore, having subdomains with roughly the same number of parcels can help equally distribute the total computational load, whereas the parallel efficiency depends on the number of interchanged parcels between processors.

Detailed descriptions on each step of the DSMC procedure and its implementation in OpenFOAM are provided next.

2.1.3. INITIALIZATION

Before running a DSMC simulation, the meshed computational domain needs to be pre-filled with parcels with pre-specified positions and velocities. Since DSMC simulations are inherently transient, a carefully chosen initialization can help shorten the total simulation time for reaching the steady state. In OpenFOAM, the required properties for the initialization are gas molecule number density ρ_n , mass averaged velocity \mathbf{u}_{ma} and temperature T . The initialization utility loops over all the cells and computes the number of required parcels in each cell based on the cell volume and ρ_n . The parcels are then initialized in random positions inside each cell and assigned with velocities that are randomly sampled from a Maxwellian distribution $f(\mathbf{u})$ as given below [7]

$$f(\mathbf{u}) = \left(\frac{m}{2\pi k_b T}\right)^{\frac{3}{2}} \exp\left[-\frac{m(\mathbf{u} - \mathbf{u}_{ma}) \cdot (\mathbf{u} - \mathbf{u}_{ma})}{2k_b T}\right] \quad (2.1)$$

where m is the molecular mass and k_b is the Boltzmann constant.

Note that the current implementation only supports a uniform initial parcel density throughout the domain. However, a more advanced one that allows non-uniform parcel density (for instance, an increasing parcel density along one dimension) could be beneficial for future applications.

2.1.4. PARCEL MOVEMENT

The computation of the parcel movement is rather straightforward. A parcel that starts at position \mathbf{x}_t with velocity \mathbf{u} will end up at location $\mathbf{x}_{t+\Delta t}$ after a time step Δt , as

$$\mathbf{x}_{t+\Delta t} = \mathbf{x}_t + \mathbf{u}\Delta t \quad (2.2)$$

However, due to this movement a parcel might go across a domain boundary, and in this case, what happens to this parcel depends on the different types of boundaries.

OPEN BOUNDARY

An open boundary is the interface between the simulated flow domain and the outside of the simulated flow domain. Gas molecules, and thus parcels, can freely move through the open boundaries, and after escaping the computational domain via an open boundary are simply being removed from the system. On the other hand, new parcels are injected into the system from the open boundaries at every time step. The procedure for generating new parcels are similar to the initialization step, but instead of initializing inside the cells, parcels are produced on the boundaries. An open boundary can be called either an inlet or outlet, depending on the direction of the pre-specified mass averaged velocity, but in either case, the parcels can freely penetrate from both sides.

The main idea behind an open inlet boundary is somewhat similar to that of the Dirichlet boundary condition in continuum flow solvers. It directly imposes ρ_n , \mathbf{u}_{ma} and T (which are often the free stream properties) of parcels entering the domain through the boundaries, implying that the flow outside the boundary is nearly unaffected by what is happening inside the computational domain. The current implementation in OpenFOAM does not allow setting different properties on inlet and outlet. For instance a pressure driven flow between inlet and outlet is not supported. However, this can be easily solved by implementing an additional utility that distinguishes the inlet and outlet by the face ID from OpenFOAM mesh data, and manually specifying different properties on each.

One thing worth mentioning here is the artifacts arising from this boundary condition. When new parcels are generated, they are injected from the same plane with different velocities, which means that those with higher velocities would possibly skip the first couple of cells and end up in cells that are further away from the boundary. Therefore, the cells right next to the boundary might have a lower number density, and one should avoid placing regions of interest right next to the open boundaries.

WALL BOUNDARY

When a solid surface is a part of the flow boundary, it is called a wall boundary. When a parcel strike on a wall boundary, it will either be bounced back or attach to and remain at the surface (e.g. physisorption or surface reaction).

For a parcel bouncing back, the two most common models are specular reflection and diffuse reflection, originally proposed by Maxwell [7]. In specular reflection, the parcel velocity component that is normal to the surface is reversed after the collision while the tangential component remain unchanged. This indicates a perfectly elastic surface regarding the impinging molecules and its functionality is identical to a symmetry plane. On the other hand, in diffuse reflection, the impinging parcels are re-emitted with velocities randomly sampled from a Maxwellian distribution at the wall temperature and directed away from the surface. In other words, the reflected parcel has no memory about its initial velocity and has reached a complete thermal equilibrium with the surface.

In reality, the reflection of a molecule is neither strictly specular nor strictly diffusive, and the exact interaction with the surface highly depends on the nature of the gas molecules and of the solid wall. While the extension and improvement of the simple specular and diffusive wall models have been the topic of ongoing research for many years [8–10], there is no single model that can quantitatively describe the gas-surface interactions for a wide range of materials, as denoted in [1]. So apart from complex models developed for a particular combination of gas and surface, perhaps the best approximation is a linear combination of specular and diffuse reflection, assuming a real interaction can be approximated as an intermediate between them. This combination utilizes an accommodation coefficient α ($0 \leq \alpha \leq 1$), which is defined as the fraction of molecules that reflect diffusively. So when a parcel collides with a surface, the code will generate a random number $R_{[0,1]}$ in the range of $[0, 1]$, and if $R_{[0,1]} \leq \alpha$ then diffuse reflection is selected, otherwise specular reflection is selected. In the limit of $\alpha = 1$ and $\alpha = 0$, this algorithm recovers to pure diffuse and specular reflection, respectively.

Reactive Surface When the impinging molecules can react with the solid surface, the most common approach for describing the reaction probability is by utilizing a single sticking coefficient γ . Similar to the procedure with α , the code generates a random number $R_{[0,1]}$, and if $R_{[0,1]} \leq \gamma$, the impinging parcel reacts on the surface and otherwise it is (diffusively or specularly) reflected back to the flow.

While the simplicity of using a sticking coefficient γ greatly facilitates a wide range of applications, it cannot adequately model ALD type surface reactions. The main problem is the self-limiting behavior of ALD, meaning that the reaction probability also depends on whether the reactive sites have already been occupied. In order to address this problem, we use a similar methodology as adopted in earlier publications [11–13] based on the surface book-keeping approach. In this model, the surface is partitioned into a number of surface elements. If one DSMC parcel, which represents F_N real molecules, has reacted with a surface element, then the corresponding number of sites will be marked as “reacted” and extracted from the list of available sites of the element. Thus, for a parcel that hits a surface element, the probability P_{rct} of it reacting with the element is

$$P_{rct} = f_i \cdot \gamma \quad (2.3)$$

where f_i is the number fraction of unoccupied sites among the total number of sites in the i th surface element. Therefore, when $f_i = 0$, the surface element is completely saturated and no more DSMC parcels can react with this element. We have implemented this model in OpenFOAM version 2.3, and a validation case is shown later in this chapter.

2

It should be noted that realistic ALD surface chemistry is rather complex including nonideal ALD behavior, such as the readsorption of gaseous products [14] and non-self-limiting behavior due to the decomposition of the surface species [15]. However, as the aim of this thesis is to study the influence of fractal structure of agglomerates and gas rarefaction on the overall ALD coating time, these complex phenomena are not considered in our model.

2.1.5. PARCEL COLLISIONS

In the parcel collision step, collision pairs are randomly selected among all the parcels within each cell. So if there are N parcels in a cell, then the total number of possible collision pairs N_{pair} is,

$$N_{pair} = \frac{N(N-1)}{2} \quad (2.4)$$

and for each potential collision pair, the collision probability P_{col} is computed as,

$$P_{col} = F_N \sigma_T c_r \Delta t / V_c \quad (2.5)$$

where F_N is the number of real molecules that is represented by one parcel, σ_T is the total collision cross-section, c_r is the relative velocity between the two molecules and V_c is the volume of the cell. So P_{col} is basically the ratio of the swept volume caused by the parcel relative movement to the total volume of the cell, and it does not take into account whether the parcel trajectories are actually intersected. This is why the cells should be kept small, and thus avoid nonphysical long range interaction between parcels.

With Eqs. (2.4) and (2.5), one may intuitively loop over all N_{pair} pairs and using P_{col} and a random number $R_{[0,1]}$ to decide whether a collision should happen. However, this algorithm scales with N^2 and suffers from low computational efficiency. Because most of the looped pairs would be rejected due to the usually very small P_{col} , OpenFOAM instead implements a method called No Time Counter (NTC) [16] to overcome this problem. In NTC, the number of collision candidates in a cell is reduced to

$$N_{pair} = \frac{1}{2} N^2 F_N (\sigma_T c_r)_{max} \Delta t / V_c \quad (2.6)$$

where $(\sigma_T c_r)_{max}$ is the maximum value of all possible $(\sigma_T c_r)$ combinations in the cell, and updated at the beginning of each time step. On the other hand, the collision probability is increased to

$$P_{col} = \frac{\sigma_T c_r}{(\sigma_T c_r)_{max}} \quad (2.7)$$

so that the total product of $(N_{col}P_{col})$ remains the same except for the fact that now $N(N-1)$ in Eq. (2.4) is replaced by N^2 in Eq. (2.6). This replacement can be explained by taking into account the true physics. In reality, there are $F_N N$ molecules in a cell and the number of collision pairs is $F_N N(F_N N - 1)$. Since $F_N N$ is usually extremely large, $F_N N(F_N N - 1)$ can be accurately approximated as $F_N^2 N^2$. So this scaling with N agrees with Eq. (2.6). In fact, the term $N(N-1)$ in Eq. (2.4) rises solely from the artifact that two molecules cannot collide with each other if they are represented by one parcel.

When selecting N_{pair} collision pairs, OpenFOAM uses a sub-cell method which divides a cell into 2 by 2 by 2 sub-cells, and gives priority to the pairs of which two parcels are from the same sub-cell. This further ensures the short distance between colliding parcels, and only when the total number of pairs in all sub-cells is lower than N_{pair} , it starts to pair parcels from different sub-cells.

COLLISION MODEL

When two parcels collide, we need a collision model to redistribute the momentum and energy between the parcels. Variable Hard Sphere (VHS) [17] and Variable Soft Sphere (VSS) [18] are the two most commonly applied collision models. Both models describe the molecular collisions based on the collision cross section area σ_T and the deflection angle χ defined as the angle between the relative velocities before and after the collision.

For a gas, the viscosity μ can be expressed as a function of temperature T as,

$$\frac{\mu}{\mu_{ref}} = \left(\frac{T}{T_{ref}}\right)^\omega \quad (2.8)$$

with $\mu = \mu_{ref}$ at $T = T_{ref}$, where ω is called the viscosity index, and μ_{ref} and T_{ref} are the reference viscosity and temperature respectively.

In the VHS model, σ_T is a function of c_r , ω , T_{ref} and μ_{ref} (μ_{ref} is included indirectly through molecular reference diameter, which is not covered in this thesis), and $\cos(\chi)$ is randomly drawn from a uniform distribution between 0 and 1. By directly taking the macroscopic properties (ω , T_{ref} and μ_{ref}) as input, the VHS model tunes the molecular collisions such that the first approximation to the viscosity from the Chapman-Enskog theory [19] renders the correct μ as in Eq. (2.8). In comparison to VHS, VSS includes one additional parameter α in the selection of $\cos(\chi)$, which ensures accurate prediction of the gas diffusivity. A detailed description and derivation of VHS and VSS models can be found in [1].

2.1.6. VALIDATION OF ALD REACTION MODEL

In this section, we validate our implemented ALD reaction model by simulating 1D gas flow reacting on a flat substrate, as shown in Fig. 2.1 (left). In OpenFOAM, the 1D prob-

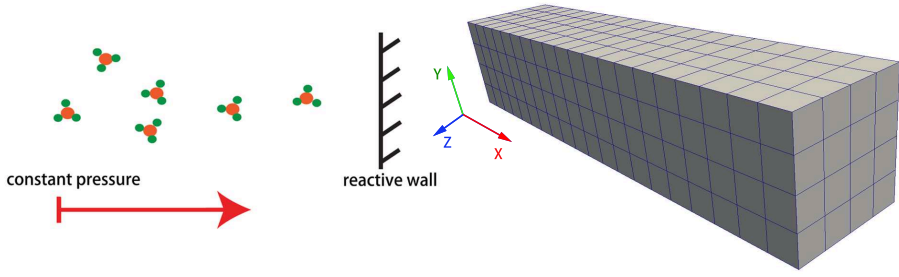


Figure 2.1: Left: schematic representation of the 1D gas flow reacting on a flat wall. Right: computational domain with grid mesh.

lem is actually simulated on a 3D mesh, as shown in Fig 2.1 (right). In this case, two species of gas, one with a low concentration being the reactive gas, and the other with a high concentration being the inert carrier gas, are supplied from one side of the computational domain. This side is set as an open boundary so that the number density, and thus the pressure, of the gas is fixed. The opposite side of the domain is set as a reactive wall with diffuse reflection, and the rest of the boundaries are set as symmetry planes.

THEORY

In a stationary gas, if the molecular number density of a gas species n_s at the surface is known, then the number of molecules J_s that strike on a unit surface area in a unit time can be expressed as

$$J_s = \frac{1}{4} n_s c_m \quad (2.9)$$

If the molecules react to the surface with sticking coefficient γ , then the reaction rate R_s , defined as the number of molecules that react with the wall in a unit time, can be approximated as

$$\begin{aligned} R_s &= J_s \gamma \frac{1}{1 - \gamma/2} \\ &= \frac{1}{4} n_s c_m \gamma \frac{1}{1 - \gamma/2} \end{aligned} \quad (2.10)$$

Here $\frac{1}{1 - \gamma/2}$ is a correction factor [20] that accounts for the fact that the gas is not stationary but has a non-zero velocity towards the surface. It is stated that Eq. (2.10) is only accurate when either the number fraction of the reacting species is very small, or γ is close to zero.

For an ALD surface reaction, if there are initially θ_0 available sites in a unit area, and

$\theta(t)$ still available at time t , then using Eq. (2.3) the reaction rate $R_s(t)$ can be written as,

$$R_s(t) = \frac{1}{4} n_s c_m \frac{\theta(t)}{\theta_0} \gamma \frac{1}{1 - \frac{1}{2} \frac{\theta(t)}{\theta_0} \gamma} \quad (2.11)$$

Also, we have

$$\frac{d\theta(t)}{dt} = -R_s(t) \quad (2.12)$$

By combining Eqs. (2.11) and (2.12), we get

$$\ln \theta(t) - \frac{\gamma}{2\theta_0} \theta(t) + \frac{1}{4} n_s c_m \frac{\gamma}{\theta_0} t + C = 0 \quad (2.13)$$

where the constant $C = -\ln \theta_0 + \frac{1}{2} \gamma$ stems from the initial condition that $\theta(t) = \theta_0$ at $t = 0$. Therefore, $\theta(t)$ can be computed for any given t by solving this nonlinear equation.

SIMULATIONS

For the sake of simplicity, O_2 and N_2 are chosen as the reactive and carrier gas respectively, regardless of the real ALD chemistry. The VHS collision model is used in this simulation and the molecular properties of both species are taken from [1]. Figure 2.1 (right) shows the domain mesh with 4 by 4 by 20 grid cells. In this case, the wall surface elements coincide with the cell faces, i.e., the wall boundary is also divided into 4 by 4 surface elements. For this particular problem, the number of surface elements does not matter since the surface sites have equal probability of receiving a parcel. In other words, there is no surface inhomogeneity that needs to be resolved by surface elements. The parameters for the computational setups are listed below:

1. domain length L : 20 mm
2. domain width W : 4 mm
3. cell size: 1 mm
4. temperature: 300 K
5. pressure at the open boundary: 1 Pa, corresponding to a molecular number density $n_{total} = 2.41 \times 10^{20} \text{ m}^{-3}$
6. number of molecules represented by one parcel: $F_N = 2.4 \times 10^7$
7. gas composition (number fraction): 1% O_2 (reactive) and 99% N_2
8. sticking coefficient $\gamma = 0.6$
9. computational time step Δt : $4 \times 10^{-7} \text{ s}$

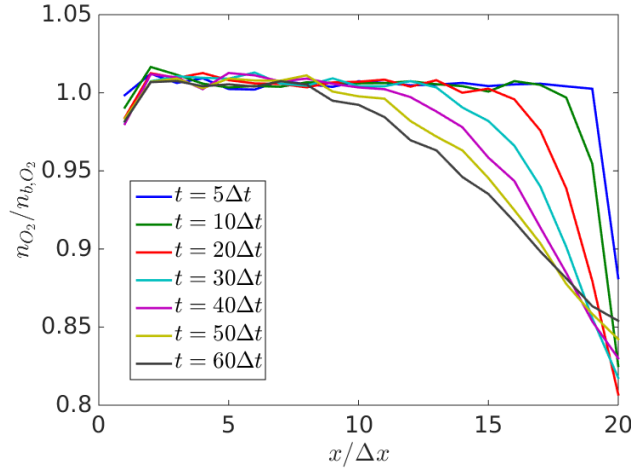


Figure 2.2: O_2 number density n_{O_2} , normalized by n_{b,O_2} , at different streamwise locations. Different lines denote the data at different time steps, as indicated in the plot.

The above settings result in about 10000 DSMC parcels (with 1% representing O_2) in each cell. The molecular number density of O_2 at the open boundary n_{b,O_2} is

$$n_{b,O_2} = 1\% \cdot n_{total} = 2.41 \times 10^{18} \quad (2.14)$$

Fig. 2.2 shows O_2 molecular number density n_{O_2} , normalized by n_{b,O_2} , at different streamwise locations, with each data point being averaged over 100 different runs in order to suppress statistical noise. As the simulation starts, n_{O_2} quickly drops at the wall due to the surface reaction, and at around $t = 20\Delta t$ it reaches its minimum and starts to increase again until all the reactive sites are occupied. This qualitatively agrees with the expected dynamics at the wall. Note that the slightly lower number density near $x = 0$ is due to the aforementioned open boundary artifact.

For a quantitative analysis, we compare the fraction of total reacted sites $(\theta_0 - \theta(t))/\theta_0$ at different time $t/\Delta t$, with the analytical results from Eq. (2.13). Since n_{s,O_2} varies inbetween 80% and 100% of n_{b,O_2} as shown in Fig. 2.2, we compute the analytical values of $\Theta(t)$ based on these two limits as reference. The comparison is shown in Fig. 2.3. The results from DSMC simulations agree very well with the general trend predicted by Eq. (2.13).

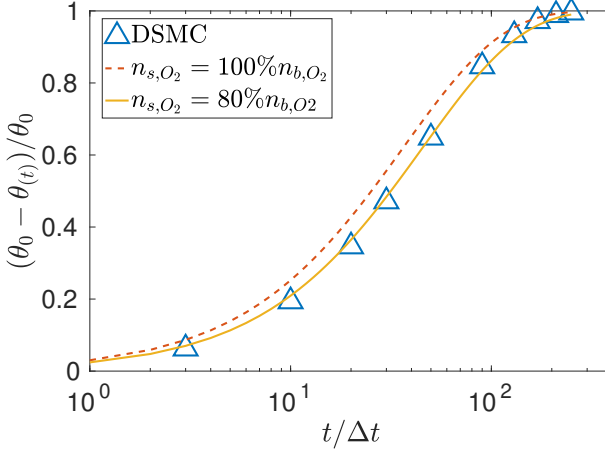


Figure 2.3: Fraction of reacted sites $(\theta_0 - \theta(t))/\theta_0$ at different time steps. Blue triangles denote the DSMC results, red dashed line and yellow solid line denote the theoretical results assuming $n_{s,O_2} = 100\%$ and 80% n_{b,O_2} , respectively.

2.2. TUNABLE ALGORITHMS FOR GENERATING FRACTAL AGGLOMERATES

In this section we discuss in detail the tunable algorithms, proposed by Filippov et al. [21], that generate fractal agglomerates based on the prescribed k_f , D_f and N .

A fractal agglomerate with N particles can be characterized by the following scaling law

$$N = k_f \left(\frac{R_g}{a} \right)^{D_f} \quad (2.15)$$

The gyration radius R_g in Eq. (2.15) is defined as

$$R_g^2 = \frac{1}{N} \sum_{i=1}^N (r_i - r_c)^2 \quad (2.16)$$

where r_i and r_c are coordinates of the i th particle center and the agglomerate mass center respectively.

A tunable algorithm constructs agglomerates using a bottom-up approach with multiple steps of adding new particle(s), and at each step the following three conditions are fulfilled:

1. The newly generated agglomerate exactly satisfies Eq. (2.15).

2. Particles do not overlap with each other.
3. Each particle is attached to at least one other particle.

Depending on how many particles are added at a time, tunable algorithms are classified into two categories: (1) sequential algorithm, and (2) cluster-cluster aggregation algorithm.

2.2.1. SEQUENTIAL ALGORITHM

A sequential algorithm starts with a dimer, i.e. two particles attached to each other, and adds one particle at a time. If an agglomerate with $N - 1$ particles is already constructed, then for the N th particle Eq. (2.15) leads to

$$(r_N - r_{c,N-1})^2 = \frac{N^2 a^2}{N-1} \left(\frac{N}{k_f}\right)^{\frac{2}{D_f}} - \frac{N a^2}{N-1} - N a^2 \left(\frac{N-1}{k_f}\right)^{\frac{2}{D_f}} \quad (2.17)$$

where r_N and $r_{c,N-1}$ are the coordinates of the N th particle center and the mass center of the first $N - 1$ particles respectively. Thus Eq. (2.17) fixes the distance L_N between the N th particle center and the mass center of the first $N - 1$ particles, which renders a surface of a sphere with radius L_N for all possible positions of the N th particle center. We call this sphere surface S_N .

The N th particle is then randomly placed on S_N fulfilling the other two conditions, i.e. touching with at least one of the first $N - 1$ particles while not overlapping with any of them. This can be achieved by first finding a set of particles which satisfy $L_N - a \leq |r_i - r_{c,N-1}| \leq L_N + a$ from the first $N - 1$ particles [22]. This set of particles serve as candidates for attaching the N th particle, since they are located within the range $[-a, a]$ from S_N . Next, we randomly select a particle from the candidates and attach the N th particle while keeping the center of the N th particle on S_N . This renders a circle for all the possible positions of the N th particle center. Now we discretize this circle with around 20 points equally distributed along this circle, and then randomly loop over these points to place the N th particle. After each placement, we check for the overlap. If there is no overlap, then we stop and the current selected point becomes the position of the N th particle. If an overlap is detected, then we continue until either a point with no overlap is found or all the points have been checked. In the later case, we remove the current selected particle from the candidate list and repeat the above procedure until we find a position with no overlap for the N th particle.

Figure 2.4 shows an agglomerate generated from the sequential algorithm with $k_f = 1.3$, $D_f = 1.8$ and $N = 1000$. It shows a highly ramified agglomerate structure with long branches starting near the center of the agglomerate. This structure does not resemble the agglomerates found from natural processes, and thus Filippov et al. [21] discourage

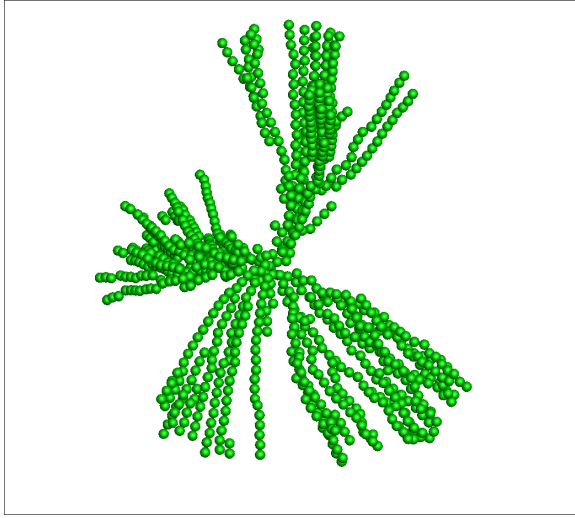


Figure 2.4: A numerically generated agglomerate using the sequential algorithm, with $k_f = 1.3$, $D_f = 1.8$ and $N = 1000$.

the use of this sequential algorithm for any further analysis on agglomerates, despite that they exactly fulfill the fractal scaling law.

2.2.2. CLUSTER-CLUSTER AGGREGATION ALGORITHM

The cluster-cluster aggregation algorithm combines two sub-agglomerates at each step, instead of adding a single particle. The initial sub-agglomerates are small aggregates of very few, typically 5-8, particles, generated with sequential algorithm or even dimers. When combining any two sub-agglomerates containing N_1 and N_2 particles and having gyration radius $R_{g,1}$ and $R_{g,2}$ respectively, Eq. (2.15) leads to

$$(N_1 + N_2)R_g^2 = N_1R_{g,1}^2 + N_2R_{g,2}^2 + \frac{N_1N_2}{N_1 + N_2}L_{1,2}^2 \quad (2.18)$$

where R_g is the gyration radius of the generated agglomerate and $L_{1,2}$ is the distance between the mass center of the two sub-agglomerates. We can derive from Eq. (2.18) a necessary and sufficient condition for fulfilling the fractal scaling law as,

$$L_{1,2}^2 = \frac{a^2(N_1 + N_2)}{N_1N_2} \left(\frac{N_1 + N_2}{k_f} \right)^{\frac{2}{D_f}} - \frac{N_1 + N_2}{N_2}R_{g,1}^2 - \frac{N_1 + N_2}{N_1}R_{g,2}^2 \quad (2.19)$$

Similar to Eq. (2.17), Eq. (2.19) fixes the distance between the mass centers of the two sub-agglomerates. So if we set the coordinates on the mass center of one of the

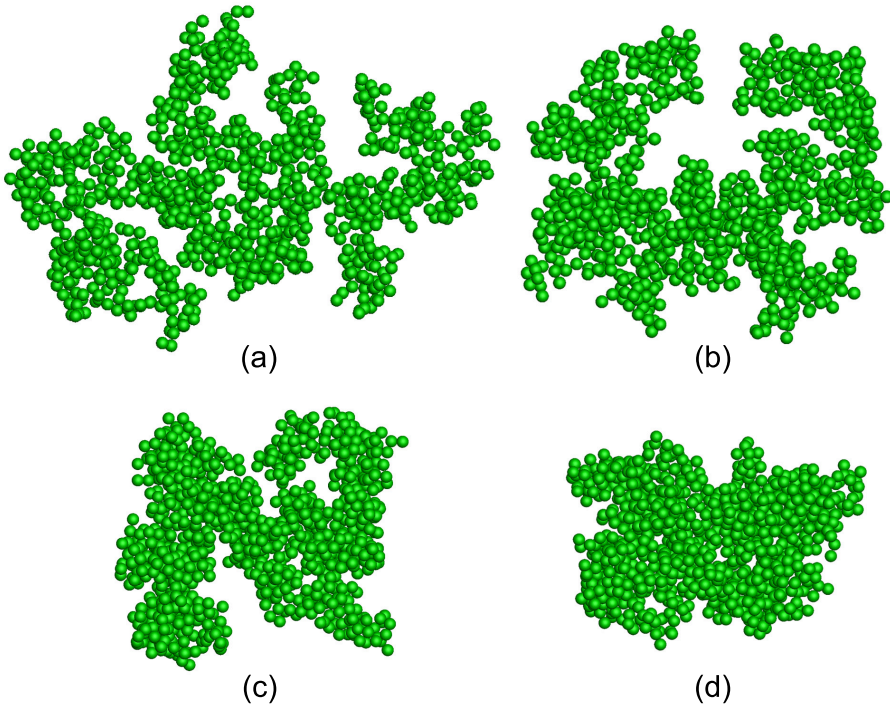


Figure 2.5: Numerically generated agglomerates using the cluster-cluster aggregation algorithm, with $N = 1024$, $k_f = 1.1$, $D_f = 2.2$ (a), 2.3 (b), 2.4 (c), and 2.5 (d).

sub-agglomerates, then finding the position for the other sub-agglomerate mass center becomes very similar to finding position for the N th particle in the sequential algorithm, except that we need to change the orientation of the second sub-agglomerate multiple times when checking for the overlap.

Figure 2.5 shows agglomerates generated from the cluster-cluster aggregation algorithm, with $N = 1024$, $k_f = 1.1$ and $D_f = 2.2 - 2.5$. Note that a higher fractal dimension results in a more densely packed agglomerate. In contrast to the SA generated agglomerate, no central part or long branches can be noticed, and the generated agglomerates look similar to the ones generated from "mimicking" algorithms described in Chapter 1.

2.2.3. INTRINSIC RANDOMNESS AND DISCONTINUITY AT SMALL N

It is important to note that the fractal scaling law [Eq. (2.15)] does not uniquely define one single agglomerate. In fact, an infinite number of different agglomerates can be generated with the same k_f , D_f , N and a . In a 3D Euclidean space one needs $O(3N)$ pa-

rameters to fully determine the structure of an agglomerate for given N and a . However, in this work, we set only three parameters for an agglomerate, namely k_f , D_f and R_g . Although these three parameters should not be directly seen as three of the $3N$ parameters due to fact that the fractal scaling is applied multiple times on different length scales, it still leaves many unknown parameters for fully determining an agglomerate for $N \gg 1$. The cluster-cluster aggregation algorithm takes these unknowns as purely random variables, as indicated by the stochastic procedures mentioned earlier. This randomness in the numerical procedure also echoes the intrinsic randomness in agglomerates produced from natural process.

Another important issue is the discontinuity of the fractal scaling law, i.e. Eq. (2.15), at $N = 1$ and 2.

When $N = 1$, Eq. (2.16) yields $R_g = 0$, and thus Eq. (2.15) does not hold, no matter what k_f and D_f we choose. More fundamentally, the fractal dimension D_f describes the scaling of the number of particles against the agglomerate size which is a measure of the distances between particles. For instance, we can intuitively consider D_f as an indication of how widely the particles are spread out in a Euclidian space. Therefore, it is meaningless to discuss Eq. (2.15) for a single particle, as there is no second particle to indicate how far they are separated from each other. As a result, any scaling analysis of physical properties based on Eq. (2.15) should not aim at having a correct limit at $N = 1$.

When $N = 2$, Eq. (2.16) yields $R_g = a$ for two particles that are attached together. Thus, the only way to satisfy Eq. (2.15) is to set $k_f = 2$, whereas any $k_f \neq 2$ would result in discontinuity at $N = 2$. One way to overcome this discontinuity is to remove the condition that particles should be in contact with at least one other particle. This allows an additional degree of freedom to adjust the distance between the two particles so that Eq. (2.15) can be exactly satisfied for various prescribed k_f and D_f at $N = 2$. Chapter 5 utilizes this approach to generate random agglomerates, and provides a detailed discussion on the resulting simulated ALD coating times.

REFERENCES

- [1] G. A. Bird, *Molecular gas dynamics and the direct simulation of gas flows*, 2nd ed. (Clarendon Press, 2003).
- [2] S. Chapman, T. G. Cowling, and D. Burnett, *The mathematical theory of non-uniform gases : an account of the kinetic theory of viscosity, thermal conduction and diffusion in gases* (Cambridge Univ. Press, 1999).
- [3] A. L. Garcia and W. Wagner, *Time step truncation error in direct simulation Monte Carlo*, *Physics of Fluids* **12**, 2621 (2000).

- [4] Z.-X. Sun, Z. Tang, Y.-L. He, and W.-Q. Tao, *Proper cell dimension and number of particles per cell for DSMC*, *Computers & Fluids* **50**, 1 (2011).
- [5] W. Wagner, *A convergence proof for Bird's direct simulation Monte Carlo method for the Boltzmann equation*, *Journal of Statistical Physics*, *Journal of Statistical Physics* **66**, 1011 (1992).
- [6] T. J. Scanlon, E. Roohi, C. White, M. Darbandi, and J. M. Reese, *An open source, parallel DSMC code for rarefied gas flows in arbitrary geometries*, *Computers & Fluids* **39**, 2078 (2010).
- [7] J. Maxwell, *On the Dynamical Theory of Gases*, *Philosophical Transactions of the Royal Society of London* **157**, 49 (1867).
- [8] Z. Li and H. Wang, *Gas-Nanoparticle Scattering: A Molecular View of Momentum Accommodation Function*, *Physical Review Letters* **95** (2005), 10.1103/physrevlett.95.014502.
- [9] I. A. Graur, P. Perrier, W. Ghoulani, and J. G. Méolans, *Measurements of tangential momentum accommodation coefficient for various gases in plane microchannel*, *Physics of Fluids* **21**, 102004+ (2009).
- [10] H. Yamaguchi, T. Imai, T. Iwai, A. Kondo, Y. Matsuda, and T. Niimi, *Measurement of thermal accommodation coefficients using a simplified system in a concentric sphere shells configuration*, *Journal of Vacuum Science & Technology A: Vacuum, Surfaces, and Films* **32**, 061602+ (2014).
- [11] J. Dendooven, D. Deduytsche, J. Musschoot, R. L. Vanmeirhaeghe, and C. Detavernier, *Modeling the Conformality of Atomic Layer Deposition: The Effect of Sticking Probability*, *Journal of The Electrochemical Society* **156**, P63 (2009).
- [12] H. C. M. Knoop, E. Langereis, M. C. M. van de Sanden, and W. M. M. Kessels, *Conformality of Plasma-Assisted ALD: Physical Processes and Modeling*, *Journal of The Electrochemical Society* **157**, G241 (2010).
- [13] M. Rose and J. W. Bartha, *Method to determine the sticking coefficient of precursor molecules in atomic layer deposition*, *Applied Surface Science* **255**, 6620 (2009).
- [14] M. Ritala, M. Leskela, L. Niinisto, and P. Haussalo, *Titanium isopropoxide as a precursor in atomic layer epitaxy of titanium dioxide thin films*, *Chem. Mater.* **5**, 1174 (1993).
- [15] S. M. George, *Atomic Layer Deposition: An Overview*, *Chemical Reviews*, *Chem. Rev.* **110**, 111 (2010).
- [16] D. P. Weaver, D. H. Campbell, and E. P. Muntz, eds., *Perception of Numerical Methods in Rarefied Gasdynamics*, in *Rarefied Gas Dynamics: Theoretical and Computational Techniques* (American Institute of Aeronautics and Astronautics, Washington DC, 1989) pp. 211–226.

- [17] S. S. Fisher, ed., *Monte-Carlo Simulation in an Engineering Context*, in *Rarefied Gas Dynamics, Parts I and II* (American Institute of Aeronautics and Astronautics, New York, 1981) pp. 239–255.
- [18] K. Koura and H. Matsumoto, *Variable soft sphere molecular model for air species*, *Physics of Fluids A: Fluid Dynamics* **4**, 1083 (1992).
- [19] W. G. Vincenti and C. H. Kruger, *Introduction to physical gas dynamics* (Krieger, 2002).
- [20] H. Motz and H. Wise, *Diffusion and Heterogeneous Reaction. III. Atom Recombination at a Catalytic Boundary*, *The Journal of Chemical Physics* **32**, 1893 (1960).
- [21] A. V. Filippov, M. Zurita, and D. E. Rosner, *Fractal-like Aggregates: Relation between Morphology and Physical Properties*, *Journal of Colloid and Interface Science* **229**, 261 (2000).
- [22] K. Skorupski, J. Mroczka, T. Wriedt, and N. Riefler, *A fast and accurate implementation of tunable algorithms used for generation of fractal-like aggregate models*, *Physica A: Statistical Mechanics and its Applications* **404**, 106 (2014).



3

A NEW CUT-CELL ALGORITHM FOR DSMC SIMULATIONS OF RAREFIED GAS FLOWS AROUND IMMERSED MOVING OBJECTS

Direct Simulation Monte Carlo (DSMC) is a widely applied numerical technique to simulate rarefied gas flows. For flows around immersed moving objects, the use of body fitted meshes is inefficient, whereas published methods using cut-cells in a fixed background mesh have important limitations. We present a novel cut-cell algorithm, which allows for accurate DSMC simulations around arbitrarily shaped moving objects. The molecule-surface interaction occurs exactly at the instantaneous collision point on the moving body surface, and accounts for its instantaneous velocity, thus precisely imposing the desired boundary conditions. A simple algorithm to calculate the effective volume of cut cells is presented and shown to converge linearly with grid refinement. The potential and efficiency of method is demonstrated by calculating rarefied gas flow drag forces on steady and moving immersed spheres. The obtained results are in excellent agreement with results obtained with a body-fitted mesh, and with analytical approximations for high-Knudsen number flows.

3.1. INTRODUCTION

The Direct Simulation Monte Carlo (DSMC) is a well-established, discrete particle based, numerical method for the computation of rarefied gas flows [2]. It is widely applied in fields such as aerospace engineering and Micro-Electro-Mechanical Systems (MEMS), where the rarefaction is important due to low pressures and small dimensions, respectively [3–5].

3

Compared to possible alternatives, such as Molecular Dynamics [6], multiple-particle collision dynamics [7], dissipative particle dynamics [8] and Lattice Boltzmann [9], DSMC has grown to be the most widely applied and validated method for simulating gas flows in the rarefied regime, i.e. the transition regime between continuum flow and free molecular flow.

In conventional DSMC simulations, the flow domain is discretized into a number of fixed shape grid cells, wherein the simulated gas molecules can move freely. The grid cells are used exclusively in process of randomly selecting pairs of gas molecules as collision partners, and for calculating average flow properties. When the walls of solid objects contribute as part of the flow boundaries, boundary conditions at those walls are imposed by prescribing appropriate molecule-wall collision laws. Here, the object walls may (i) be approximated by staircases with local grid refinement [2, 10], (ii) coincide with grid cell faces (requiring the use of non-Cartesian, body fitted meshes to accommodate complexly shaped immersed bodies), or (iii) cut through grid cells.

The first approach can be seen as a special case of the coincided grid with an additional staircase approximation to the walls. The last approach has been called the cut-cell method [11, 12]. It is somewhat similar to the so-called immersed boundary method (IBM), proposed by Peskin [13] to impose boundary conditions on the walls of immersed objects in continuum based flow simulations. However, whereas in IBM fictitious external forces, localized near the boundary, have to be imposed to satisfy boundary conditions, in DSMC cut-cell methods such fictitious forces are not needed, as the boundary conditions are imposed explicitly and exactly through the molecule-wall collision laws. On the other hand, the cell effective volume has to be computed for the cut cells in order to achieve the correct molecular collision probabilities.

The cut-cell method is particularly advantageous over the use of body fitted meshes when the immersed object moves with respect to the grid, e.g. when studying gas flows in MEMS with oscillating parts, or Brownian aerosol particle movement in gas flows. In such situations, the use of body fitted meshes would require body fitted grids to be regenerated at each time step, which is computationally inefficient.

For simply shaped moving immersed objects, of which the surface is limited to flat planes aligned with the cell faces, the cut-cell method has been demonstrated for applications with 1-D moving piston [14] and turbomolecular pumps [15]. The cut-cell

method has also been demonstrated for applications with 2-D static immersed bodies [16].

For complexly shaped 3-D immersed objects, two main approaches for cut-cell DSMC simulations have been proposed [11, 12], which mainly differ by the way in which the immersed solid object surfaces are represented numerically. Both approaches make use of random markers to distinguish between the inside and outside of the immersed object.

The first approach [11, 12] represents the approximate shape of the immersed surface by small contiguous triangular facets. Molecules interact with these facets during the molecular streaming step in the DSMC algorithm. In this approach, the facet size determines the accuracy by which the surface, and thus the location of the boundary, is being represented, whereas the grid size determines the resolution of the flow field simulations. The effective volume of cut cells, which is needed during the molecule-molecule collision step of the algorithm, is computed either by polyhedral decomposition utilizing the facets and the cell faces, or by Monte Carlo random markers. [17] have applied the latter to a 3-D moving object, and simulated the Brownian motion of a spherical particle immersed in a rarefied gas. It is stated that the random marker based approach is easy to implement but computationally expensive.

The second approach [12] uses an analytical expression for the immersed surface shape as an input. This shape is subsequently approximated by planar faces, which are determined by finding the two smallest possible cuboids which respectively contain all random points inside, and outside, of the immersed object. This method may result in gaps between the faces, which become significant when the ratio of the surface curvature radius to the cell size is small.

Summarizing the present state-of-art, there is a clear need for a computationally efficient DSMC cut-cell algorithms that allow for an accurate, gap-free representation of immersed surfaces and the cell effective volumes. In the present work, we present, demonstrate and validate such an algorithm.

Compared to earlier cut-cell methods, (i) our algorithm utilizes an exact analytical representation of the immersed surface for computing the DSMC particle streaming step and thus the particle-surface interaction. Therefore, this step does not rely on a triangulated surface representation and does not leave gaps between approximated surface elements; (ii) in our algorithm both the flow resolution and the accuracy of the cut-cell effective volume scale with cell size; (iii) the molecules collide and interact exactly at the instantaneous location of the moving surface; (iv) our algorithm avoids the use of expensive Monte Carlo methods in calculating the effective volume of cut cells. Thus, like IBM methods in continuum flow simulations, our method explicitly imposes the correct boundary conditions exactly at the instantaneous location of the analytically expressed moving surface. On the other hand, our method is limited to geometries of which the surface can be expressed by analytical expressions. Also, the current implementation of

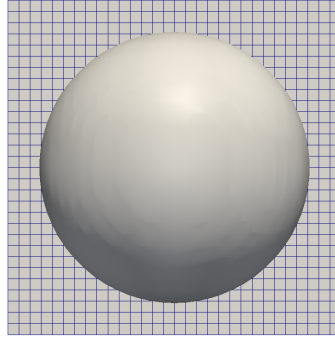


Figure 3.1: An immersed sphere in a fixed grid (clipped).

our method does not take into account the possibility of the occurrence of split cells, i.e. cells which are divided into multiple independent regions by the immersed object. Rather, we only focus on objects of which the local curvature is larger than the local cell size.

3.2. CUT-CELL ALGORITHM IN DSMC

For the sake of simplicity, a perfect sphere is selected as an immersed object for the illustration of the algorithm. Later we will discuss more complex body shapes.

Figure 3.1 shows an immersed sphere in a fixed Cartesian grid. In DSMC, there are two main steps for gas molecular dynamics: 1) the molecular streaming step and 2) the molecular collision step, which are decoupled from each other at each time step as the essential assumption of the method. For an immersed body with a pre-known and analytically expressed shape, the interaction of the particles with the immersed boundary is calculated exactly at the landing point of the particle on the analytically expressed boundary, as shown later in section 3.4. On the other hand, the intermolecular collision step requires computation of the cell volume for a correct collision probability between two simulated molecules in a cell. Equation (3.1) [2] shows this probability P and the empty volume of the occupied cell is required as the denominator:

$$P = F_N \sigma_T c_r \Delta t / V_c \tag{3.1}$$

Here, F_N is the number of real molecules that is represented by one simulated molecule, σ_T is the total collision cross-section, c_r is the relative velocity between the two molecules, Δt is the time step and V_c is the empty volume of the cell.

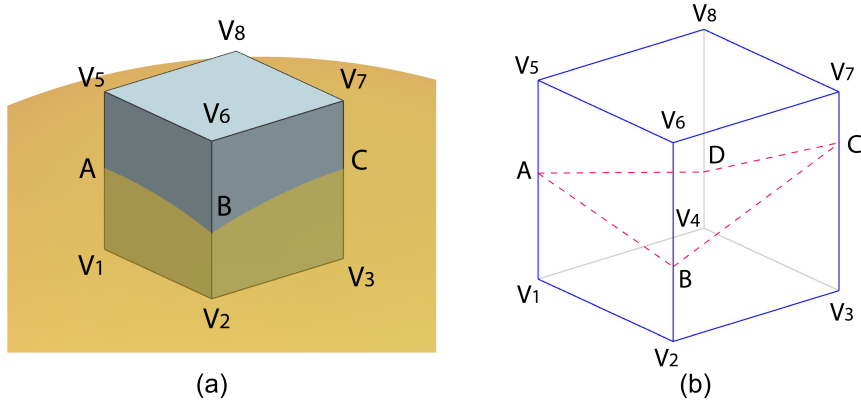


Figure 3.2: (a) A grid cell intersected by an immersed sphere and (b) polyhedra generated using intersecting points. The latter is only used for effective volume calculation in determining particle-particle collisions, not for surface reconstruction in calculating particle-surface interactions.

When an immersed boundary intersects the grid cells, the cut cells are partially overlapped by the immersed body and therefore the overlap volume should be subtracted from the original cell volume to provide an effective empty volume V_c and thus correct collision probability.

3.2.1. OVERLAP VOLUME COMPUTATION ALGORITHM

Figure 3.2 shows a grid cell that is intersected by an immersed sphere. In this example, there are four intersected edges from the cell. Nevertheless, in other cases with different number of intersected edges the computation of overlap volume follows the same algorithm summarized below:

1. Find all the intersected edges of the cell and compute the coordinates of the intersecting points at each edge, namely A , B , C and D in Figure 3.2.
2. Generate polyhedra using A , B , C , D , V_1 , V_2 , V_3 and V_4 as vertices. Since A , B , C and D are not necessarily on the same plane, there are more than one possible polyhedra from the configuration depending on either using \overline{AC} or \overline{BD} as one of the edges of the polyhedron.
3. Each of the possible polyhedra is decomposed into a number of pyramids by connecting its faces with the center of volume. Then the volume of each pyramid is computed and summed up to yield the volume of each initial polyhedron.
4. In this example, since a sphere is a convex body, the maximum volume from the above possible polyhedra could serve as the best approximation for the overlap

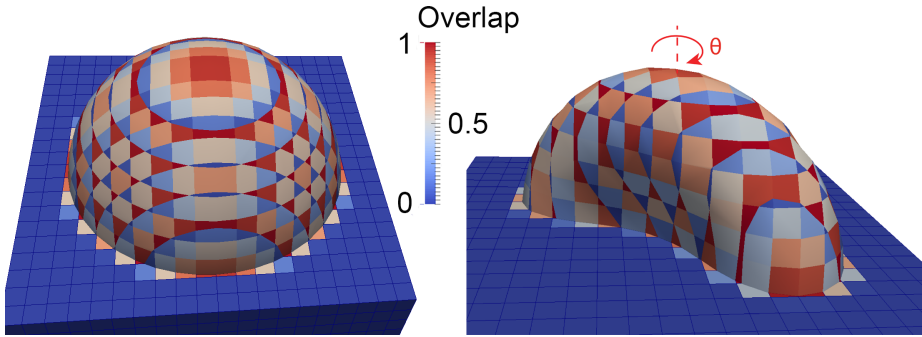


Figure 3.3: Immersed sphere (left) and red blood cell (right) reproduced from contours of 50% overlap. The color map shows the overlap fraction of each grid cell.

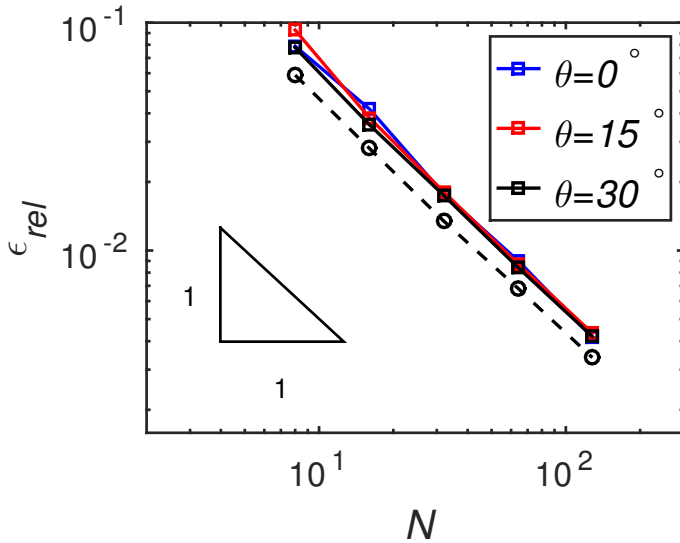


Figure 3.4: Relative error in the computed overlap volume against different grid resolutions for the sphere (circles) and the red blood cell (squares).

volume. However, to be more general, we use an average over the maximum and minimum as a good approximation, as shown later in this section.

In this example, the grid resolution is defined by $N = d/\Delta x$, where d is the sphere diameter and Δx is the cell size. Figure 3.3 (left) shows an immersed sphere reproduced by the contour of 50% overlap using the average volume of the polyhedra at $N = 16$, which renders an excellent spherical surface. The color map on the surface indicates

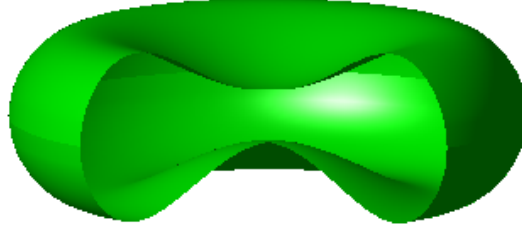


Figure 3.5: Red blood cell shape expressed by Equation (3.3) (a quarter is clipped out).

how the boundary cells are intersected by the sphere surface.

Since it is the effective volume of the boundary cells that directly contributes to the molecular collision probability, the relative error in the reconstructed sphere volume is defined as,

$$\epsilon_{rel} = \frac{V_{IB} - \sum_{all\ cells} V_{overlap}}{\sum_{boundary\ cells} V_{overlap}} \quad (3.2)$$

Here, V_{IB} is the actual volume of the immersed body, $V_{overlap}$ is the calculated overlap volume of each cell including the ones that are completely enclosed by the sphere and $V_{overlap, boundary}$ is the overlap volume of a partially overlapped boundary cell.

Figure 3.4 shows ϵ_{rel} for different grid resolutions. The relative error in the computed overlap volume decreases linearly with increasing N .

In order to illustrate that the same algorithm works for any other arbitrary shape, a red blood cell shaped body is chosen as a second example. The shape can be expressed by Equation (3.3) [18] and is plotted in Figure 3.5.

$$z(r) = 1/2 \sqrt{1 - \left(\frac{r}{R}\right)^2} \left(C_0 + C_2 \left(\frac{r}{R}\right)^2 + C_4 \left(\frac{r}{R}\right)^4 \right) \quad (3.3)$$

Here, R is $3.91 \mu\text{m}$, C_0 is $0.81 \mu\text{m}$, C_2 is $7.83 \mu\text{m}$ and C_4 is $-4.31 \mu\text{m}$. The major diameter of the red blood cell is $d = 2R$ and again the grid resolution is defined as $N = d/\Delta x$.

Figure 3.3 (right) shows a red blood cell reproduced by the contour of 50% overlap at $N = 16$, which agrees well with the shape shown in Figure 3.5. ϵ_{rel} is again defined by Equation (3.2). To study the sensitivity of the method to the alignment of the body with the grid, the immersed red blood cell is tilted at different angles θ with respect to the background grid, as shown in Figure 3.3 (right). Figure 3.4 shows ϵ_{rel} against different

grid resolutions. The results for $\theta = 0^\circ, 15^\circ$ and 30° are very close to each other and they all converge linearly in N . Since the resolution is defined based on the major diameter d , the minor axis is relatively poorly resolved, which explains the higher relative errors compared to that of the sphere.

Thus it is concluded that the presented algorithm works for any arbitrarily shaped immersed objects and ϵ_{rel} converges with order 1 for the grid refinement N .

3

3.3. VALIDATION WITH DRAG COMPUTATION

The above overlap volume calculation algorithm has been implemented into an open source DSMC solver "dsmcFoam" in OpenFOAM [19] and the drag exerted on an immersed sphere in a creeping flow is computed for rarefied gas flows with Knudsen number larger than 0.2. The result is then validated by comparing with the drag computed from the conventional DSMC with a body-fitted grid, and with the analytical approximations.

3.3.1. COMPUTATIONAL SETUP

For the following simulations, a sphere with diameter d is located at the center of a $(10d)^3$ cubic domain with free stream boundary conditions at two opposite planes, and periodic boundary conditions at the rest of boundaries. The simulated gas is argon of which the molecular properties are taken from [2] with the variable hard sphere (VHS) collision model.

The direct input parameters are:

1. sphere diameter: $d = 2R = 5.0 \cdot 10^{-7}$ m
2. grid size: $\Delta x = \frac{d}{N}, 8 \leq N \leq 19$
3. domain size: $L = 10 \times d = 5.0 \cdot 10^{-6}$ μm
4. number of cells: $N_{cells} = 10^3 \cdot N^3$
5. number of DSMC particles: $N_{particles} > 10 \cdot N_{cells}$
6. temperature: $T = 300$ K
7. pressure: $P = 3.13 \cdot 10^3 \sim 5.0 \cdot 10^4$ Pa
8. reference viscosity: $\mu_{ref} = 2.12 \cdot 10^{-5}$ $\text{kg m}^{-1} \text{s}^{-1}$ at $T_{ref} = 273.15$ K
9. viscosity index: $\omega = 0.81$

10. free stream gas velocity: $u = 40 \sim 1.25 \text{ m s}^{-1}$

The derived parameters are:

1. mean thermal velocity: $\overline{c_m} = \sqrt{\frac{8k_b T}{\pi m}} = 398.75 \text{ m s}^{-1}$
2. mean free path: $\lambda = \frac{2\mu}{\overline{c_m}\rho} = \frac{2\mu k_b T}{\overline{c_m} m} \cdot \frac{1}{P} = 1.43 \cdot 10^{-7} \sim 2.29 \cdot 10^{-6} \text{ m}$
3. viscosity: $\mu = \mu_{ref} \left(\frac{T}{T_{ref}}\right)^\omega = 2.29 \cdot 10^{-5} \text{ kg m}^{-1} \text{ s}^{-1}$
4. Knudsen number: $Kn = \frac{\lambda}{R} = \frac{2\mu k_b T}{\overline{c_m} m R} \cdot \frac{1}{P} = 0.28 \sim 9.18$
5. Reynolds number: $Re = \frac{u\rho R}{\mu} = \frac{Rm}{\mu k_b T} \cdot (u \cdot P) = 0.022$

where k_b is the Boltzmann constant, m is the gas molecular mass and ρ is the gas density. The mean free path is calculated in the same way as [20] in order to keep consistency. In all the simulations we fulfill the common DSMC criteria, i.e. time step $\Delta t < \frac{1}{8} \lambda / \overline{c_m}$, $\Delta x < \frac{1}{3} \lambda$ and each cell contains on average at least 10 DSMC molecules to ensure a well resolved simulation [21, 22]. The gas in the domain at time $t = 0$ is initialized with the mass-averaged velocity of u .

A fully diffusive boundary condition has been employed at the sphere surface as it is the most commonly used boundary condition in literature. The drag force is directly computed at each time step from the momentum difference of the reflected molecules before and after the reflection. The drag force F_d exerted on the sphere is normalized by the Stokes drag as

$$F_d^* = \frac{F_d}{F_{Stokes}} = \frac{F_d}{6\pi\mu Ru} \quad (3.4)$$

We verified that the calculated drag values at consecutive time steps in our simulations are nearly uncorrelated, with the autocorrelation function dropping to values below 10^{-2} at $t = \Delta t$. We took the viscous diffusion time $t_\mu = \frac{(\frac{1}{2})^2 \rho}{\mu}$ as an estimate for the time needed for the flow to reach quasi-steady state. And the drag is computed by averaging over 10,000 time steps, starting from $t = 4 \times t_\mu$.

3.3.2. KN DEPENDENCE

First, Kn is varied by changing the pressure of the gas while keeping Re constant by changing the free stream velocity accordingly.

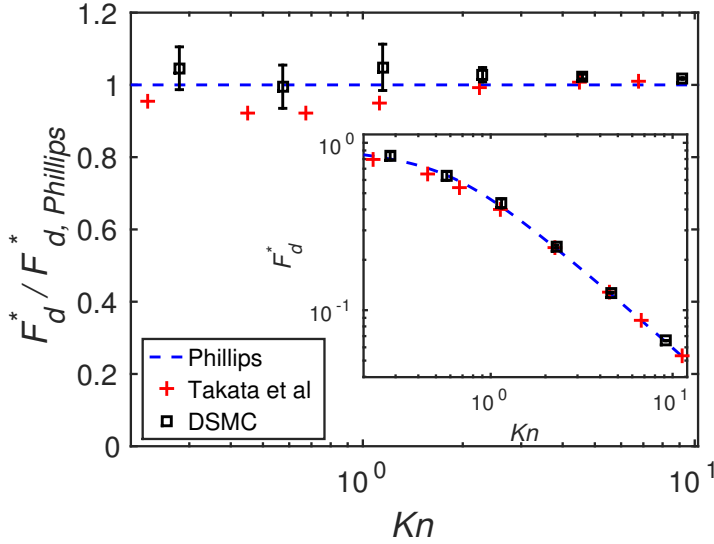


Figure 3.6: Drag force on a sphere as a function of Knudsen number, for the cut-cell DSMC simulations compared to analytical approximations by [20] and [23]. The DSMC data with $Kn = 0.28$ is averaged over 400,000 time steps; $Kn = 0.57$ is averaged over 50,000 time steps; while the rest are averaged over 10,000 time steps. Main panel: Forces are normalized by the corresponding analytical approximations from [20], plotted on a log-lin scale. Inset: Forces are normalized by the Stokes drag and plotted on a log-log scale.

F_d^* values for a sphere simulated with the cut-cell method at different Kn are shown in Figure 3.6, compared with the analytical approximations from [20] and [23]. All the error bars in the figures of this paper indicate 95% confidence intervals based on the standard deviation of mean. The drag force predicted by our DSMC simulation agrees well with the analytical results for all the shown Knudsen numbers.

3.3.3. COMPARISON WITH BODY-FITTED MESH DSMC

In this section, F_d^* calculated from the presented cut-cell method is compared to that from DSMC with a conventional body-fitted mesh. A typical body-fitted grid is shown in Figure 3.7. The sphere surface is meshed with triangular elements which are inflated two layers outwards. The rest of flow domain is meshed with tetrahedron cells. For the body-fitted mesh we define

$$N = \frac{d}{\sqrt{A_{tet,surface}}} \tag{3.5}$$

where $A_{tet,surface}$ is the area of the surface triangular elements.

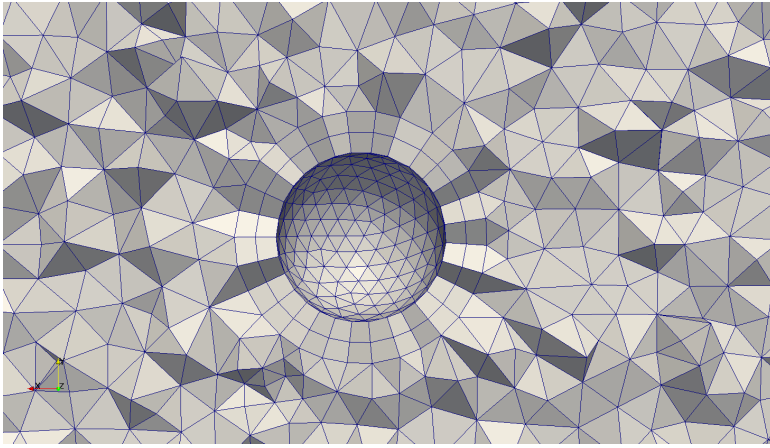
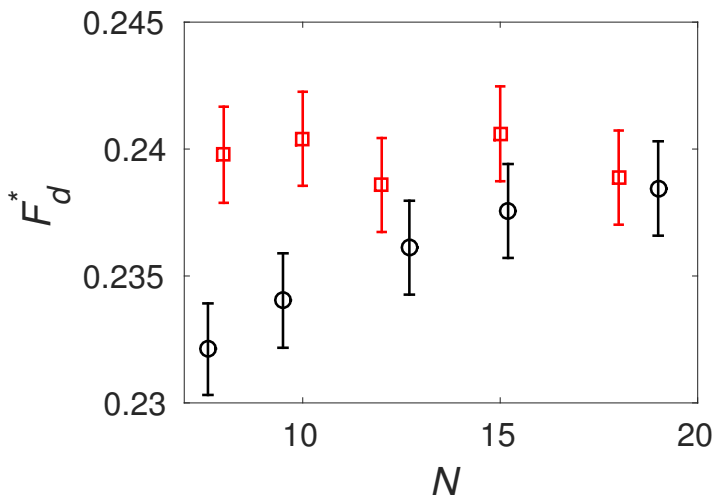


Figure 3.7: Body-fitted mesh for conventional DSMC

Figure 3.8: Normalized drag force computed from DSMC with the cut-cell method (red squares) and from the body-fitted grid (black circles), for $Kn = 2.29$.

A comparison between the body-fitted mesh results and the cut-cell method results at $Kn = 2.29$ is shown in Figure 3.8. Here, the total number of simulated molecules is kept the same for different N , in order to render similar confidence intervals. F_d^* values from the cut-cell method show less grid dependency than that from the body-fitted grid, probably due to the utilization of the exact analytic surface for the bounce back of the molecules.

3.3.4. STATIONARY AND MOVING SPHERE WITH IMMERSED BOUNDARIES

In this section, the presented cut-cell method is demonstrated with a fully three-dimensional moving immersed object. A moving sphere with a predefined velocity $\vec{u} = -u \cdot \vec{e}_x$ is simulated with the cut-cell method in a stationary gas, where \vec{e}_x is the unit vector in the streamwise direction. The sphere velocity is constant during the simulation, assuming that the sphere mass is infinitely large compared to that of the gas molecule. The computed drag F_d^* is compared with that from a steady sphere in a moving flow with velocity $+u \cdot \vec{e}_x$.

The computational domain is elongated in the stream-wise direction by $u \cdot t_{total}$ to allow the movement of the sphere, where t_{total} is the total simulation time. The sphere moves over a distance $-u \cdot \Delta t$ at each time step and the incoming molecules need to be reflected at the exact, analytically calculated, landing point P_{coll} as shown in Figure 3.9. This is achieved by switching back and forth between the steady observer reference frame and the reference frame of the moving sphere. First, the molecule streaming is calculated in the moving sphere reference frame by adding a velocity $-u$ to each molecule's thermal velocity \vec{c}_m . Since the sphere is steady in its own reference frame, the calculation procedure of the post reflection molecular velocities and positions is exactly the same as that for a steady sphere. Subsequently, the velocities and positions of the molecules are transferred back to the steady observer frame of reference by taking into account the movement of sphere during Δt .

The simulations are conducted at $Kn = 2.29$. Figure 3.10 shows the comparison of the

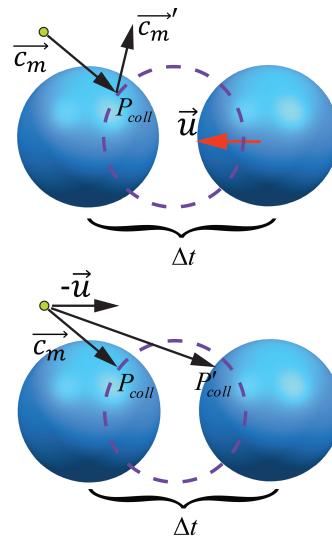


Figure 3.9: Transfer of the reference frame between the sphere and the flow domain.

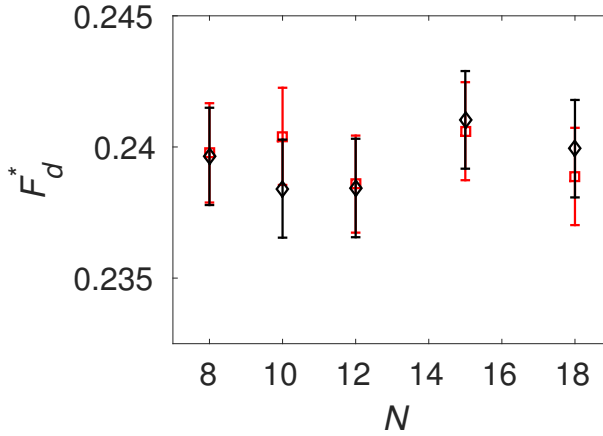


Figure 3.10: Normalized drag force computed from DSMC with the cut-cell method for a steady sphere (red squares) and for a moving sphere (black diamonds), for $Kn = 2.29$.

scaled drag force F_d^* between the moving sphere and the steady sphere, both calculated with the cut-cell method. The two results agree well with each other, illustrating that this method works for a fully three-dimensional immersed moving body.

3.4. CONCLUSION

A new cut-cell algorithm has been implemented and demonstrated in conjunction with DSMC for simulating rarefied gas flow around an immersed moving body. Based on the presented study, the following conclusions are drawn:

1. An analytically expressed surface is used to accurately bounce back the molecules. The cut cell effective volume is computed by representing the immersed boundary with the Lagrangian intersecting points and thus reconstructing all the possible polyhedra and take the mean average. It has been shown that for any arbitrary immersed bodies, the relative error in the computed overlap volume decreases linearly with the grid refinement.
2. The drag force on a sphere computed with the present cut-cell method converges to the same value as that calculated with a conventional body-fitted grid, both in good agreement with approximate analytical solutions. However, with the cut-cell method grid-independent results are obtained for coarser grids as compared to the body-fitted grid method.
3. The drag on a moving sphere in a stagnant gas computed with the cut-cell method agrees well with that of a steady sphere in a flowing gas. Thus it is shown that the

present method can apply to fully three-dimensional immersed moving bodies in a rarefied gas flow.

REFERENCES

- [1] W. Jin, Ommen, and C. R. Kleijn, *A new cut-cell algorithm for DSMC simulations of rarefied gas flows around immersed moving objects*, Computer Physics Communications **212**, 146 (2017).
- [2] G. A. Bird, *Molecular gas dynamics and the direct simulation of gas flows*, 2nd ed. (Clarendon Press, 2003).
- [3] E. S. Oran, C. K. Oh, and B. Z. Cybyk, *DIRECT SIMULATION MONTE CARLO: Recent Advances and Applications*, Annual Review of Fluid Mechanics **30**, 403 (1998).
- [4] Z. C. Hong, C. E. Zhen, and C. Y. Yang, *Fluid Dynamics and Heat Transfer Analysis of Three Dimensional Microchannel Flows with Microstructures*, Numerical Heat Transfer, Part A: Applications **54**, 293 (2008).
- [5] H. Akhlaghi, E. Roohi, and S. Stefanov, *A new iterative wall heat flux specifying technique in DSMC for heating/cooling simulations of MEMS/NEMS*, International Journal of Thermal Sciences **59**, 111 (2012).
- [6] D. Frenkel and B. Smit, *Understanding molecular simulation : from algorithms to applications*, (2002).
- [7] G. Gompper, T. Ihle, D. M. Kroll, and R. G. Winkler, *Multi-Particle Collision Dynamics – a Particle-Based Mesoscale Simulation Approach to the Hydrodynamics of Complex Fluids*, *Advanced Computer Simulation Approaches for Soft Matter Sciences III*, Advances in Polymer Science, **221**, 1 (2008), arXiv:0808.2157 .
- [8] P. J. Hoogerbrugge and J. M. V. A. Koelman, *Simulating Microscopic Hydrodynamic Phenomena with Dissipative Particle Dynamics*, Europhysics Letters (EPL) **19**, 155 (1992).
- [9] S. Chen and G. D. Doolen, *Lattice boltzmann method for fluid flows*, Annual Review of Fluid Mechanics **30**, 329 (1998).
- [10] S. Zabelok, R. Arslanbekov, and V. Kolobov, *Adaptive kinetic-fluid solvers for heterogeneous computing architectures*, Journal of Computational Physics **303**, 455 (2015).
- [11] C. Zhang and T. E. Schwartzentruber, *Robust cut-cell algorithms for DSMC implementations employing multi-level Cartesian grids*, Computers & Fluids **69**, 122 (2012).

- [12] J. M. Burt, E. Josyula, and I. D. Boyd, *Novel Cartesian Implementation of the Direct Simulation Monte Carlo Method*, *Journal of Thermophysics and Heat Transfer* **26**, 258 (2012).
- [13] C. S. Peskin, *The immersed boundary method*, *Acta Numerica* **11**, 479 (2002).
- [14] D. J. Rader, M. A. Gallis, and J. R. Torczynski, *DSMC Moving-Boundary Algorithms for Simulating MEMS Geometries with Opening and Closing Gaps*, in *American Institute of Physics Conference Series*, American Institute of Physics Conference Series, Vol. 1333 (AIP, 2011) pp. 760–765.
- [15] R. Versluis, R. Dorsman, L. Thielen, and M. E. Roos, *Numerical investigation of turbomolecular pumps using the direct simulation Monte Carlo method with moving surfaces*, *Journal of Vacuum Science & Technology A* **27**, 543 (2009).
- [16] M. C. Lo, C. C. Su, J. S. Wu, and F. A. Kuo, *Development of parallel direct simulation Monte Carlo method using a cut-cell Cartesian grid on a single graphics processor*, *Computers & Fluids* **101**, 114 (2014).
- [17] S. Shrestha, S. Tiwari, A. Klar, and S. Hardt, *Numerical simulation of a moving rigid body in a rarefied gas*, *Journal of Computational Physics* **292**, 239 (2015).
- [18] E. Evans and Y.-C. Fung, *Improved measurements of the erythrocyte geometry*, *Microvascular Research* **4**, 335 (1972).
- [19] T. J. Scanlon, E. Roohi, C. White, M. Darbandi, and J. M. Reese, *An open source, parallel DSMC code for rarefied gas flows in arbitrary geometries*, *Computers & Fluids* **39**, 2078 (2010).
- [20] W. F. Phillips, *Drag on a small sphere moving through a gas*, *Physics of Fluids* (1958-1988) **18**, 1089 (1975).
- [21] A. L. Garcia and W. Wagner, *Time step truncation error in direct simulation Monte Carlo*, *Physics of Fluids* **12**, 2621 (2000).
- [22] Z.-X. Sun, Z. Tang, Y.-L. He, and W.-Q. Tao, *Proper cell dimension and number of particles per cell for DSMC*, *Computers & Fluids* **50**, 1 (2011).
- [23] S. Takata, Y. Sone, and K. Aoki, *Numerical analysis of a uniform flow of a rarefied gas past a sphere on the basis of the Boltzmann equation for hard sphere molecules*, *Physics of Fluids A: Fluid Dynamics* **5**, 716 (1993).



4

SIMULATION OF ATOMIC LAYER DEPOSITION ON NANOPARTICLE AGGLOMERATES

Coated nanoparticles have many potential applications; production of large quantities is feasible by atomic layer deposition (ALD) on nanoparticles in a fluidized bed reactor. However, due to the cohesive interparticle forces, nanoparticles form large agglomerates, which influences the coating process. In order to study this influence, the authors have developed a novel computational modeling approach which incorporates (1) fully resolved agglomerates; (2) a self-limiting ALD half cycle reaction; and (3) gas diffusion in the rarefied regime modeled by direct simulation Monte Carlo. In the computational model, a preconstructed fractal agglomerate of up to 2048 spherical particles is exposed to precursor molecules that are introduced from the boundaries of the computational domain and react with the particle surfaces until these are fully saturated. With the computational model, the overall coating time for the nanoparticle agglomerate has been studied as a function of pressure, fractal dimension, and agglomerate size. Starting from the Gordon model for ALD coating within a cylindrical hole or trench [Gordon et al., Chem. Vap. Deposition 9, 73 (2003)], the authors also developed an analytic model for ALD coating of nanoparticles in fractal agglomerates. The predicted coating times from this analytic model agree well with the results from the computational model for $D_f = 2.5$. The analytic model predicts that realistic agglomerates of $O(10^9)$ nanoparticles require coating times that are 3–4 orders of magnitude larger than for a single particle.

This chapter has been published as Journal of Vacuum Science and Technology A **35**, 01B116 (2017) [1].

4.1. INTRODUCTION

Modifying the surface of nano and micron-sized particles results in new functionalities that have applications in many diverse fields, such as catalysis, medicine and energy conversion and storage [2–5]. Atomic layer deposition (ALD) is one such technique that can tune the particle surface by depositing precisely controlled thin film layers. It relies on two self-limiting surface reactions applied in an alternating sequence, which allows for atomic control over the film thickness and composition [6]. ALD coating on nanoparticles has been demonstrated in several experimental studies utilizing a fluidized bed [7, 8]. In fluidized bed ALD, an amount of particles is suspended in an upward gas stream containing the precursor molecules. It is a useful technique for large scale processing of particles. However, when fluidizing nanoparticles, they form agglomerates with sizes up to a few hundred microns due to the cohesive inter-particle forces. These agglomerates are (highly) porous and their complex geometries have been commonly described as fractal for their self-similarity under different length scales [9–11]. Typical fractal dimensions have been found to range from 1.8 to 2.7. When applying ALD to such agglomerates of nanoparticles, the precursor molecules need to be transported into the porous agglomerates and then react with the particle surfaces. This introduces a time scale for the gas transport which may influence the overall coating time. A good understanding of this phenomenon is important for the optimization of the ALD process cycles and an efficient utilization of the precursors [12].

4

Reaction–diffusion problems in porous media, such as catalyst particles, polymer networks, and particle assemblies, have been studied for many decades following the seminal work by Thiele [13]. There now exists an extensive body of literature [14–22] addressing reaction–diffusion in porous media for various types of reactions (e.g., homogeneous and heterogeneous reactions, first and nonfirst order reactions), various treatments of the porous structure geometry (e.g., by treating the porous structure as a single material with an effective diffusivity, or by explicitly taking into account the geometric details of the pores) and various pore geometries (e.g., cylindrical pores, packed beds). For gases, another distinction is that between the molecular diffusion regime (when the typical length scale L of the pores is much larger than the mean free path λ of the gas molecules, or the Knudsen number $Kn = \frac{\lambda}{L} \ll 1$), the free molecular regime ($Kn \gg 1$) and the transitional or the Knudsen diffusion regime ($0.1 < Kn < 10$). For ALD coating of nanoparticle agglomerates, depending on the operating pressure, it is generally necessary to account for gas rarefaction as the mean free path can be comparable to or larger than that of the particles and the pores ($\lambda \sim 10 - 100$ nm for atmospheric pressure, and $\lambda \sim 10 - 100$ μm for 1 mbar).

Reaction–diffusion problems in particle agglomerates have been studied for numerically generated agglomerates constructed from an assembly of particles with predefined assembling rules [23–26]. However, some of these studies only focus on the molecular diffusion regime ($Kn \ll 1$) [23–25], whereas others do not address self-limiting reactions in fractal geometries [23–26]. On the other hand, self-limiting ALD reactions and rar-

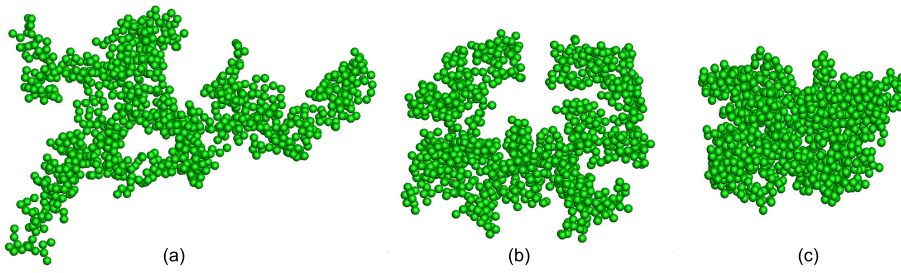


Figure 4.1: Numerically constructed fractal agglomerate with $k_f = 1.1$, $N = 1024$ for $D_f =$ (a) 2.1, (b) 2.3, and (c) 2.5.

efied gas diffusion have been studied inside very simple pore geometries such as narrow trenches and cylindrical pores [27–29].

In the present paper, we develop and demonstrate a computational model for the rarefied reaction–diffusion problem in ALD coating of agglomerated nanoparticles which, in deviation from all previous studies, combines models for (1) a fully resolved fractal agglomerate; (2) self-limiting half cycle ALD reactions; and (3) diffusion in the transition regime. Each of these aspects has been studied in literature, but to the best of our knowledge, the combination of these three is novel. With our computational model, the overall coating time is studied, focusing on the influence of pressure, agglomerate size, and agglomerate fractal dimension. We also present an analytic model which predicts the scaling of the coating time with agglomerate size, allowing for the extrapolation of our results to realistically large agglomerates.

4.1.1. NUMERICAL CONSTRUCTION OF FRACTAL AGGLOMERATES

It is commonly agreed in literature [9, 30] that a fractal agglomerate can be characterized by its size and fractal dimension as

$$N = k_f \left(\frac{R_g}{a} \right)^{D_f} \quad (4.1)$$

where N is the total number of particles in an agglomerate, k_f is a constant prefactor, a is the radius of the primary particle, and R_g the gyration radius of the agglomerate. Here, R_g is computed as,

$$R_g^2 = \frac{1}{N} \sum_{i=1}^N (r_i - r_c)^2 \quad (4.2)$$

where r_i and r_c are the coordinates of i th particle and the agglomerate mass center respectively.

Filippov et al. [31] proposed a tunable algorithm to numerically generate agglomerates for any given combination of N , k_f and D_f . This algorithm generates fractal agglomerates by a series of steps combining two different fractal sub-agglomerates, until the final agglomerate has the preset N number of particles. At each step, both the sub-agglomerates and the generated new agglomerate exactly fulfill Eq. (4.1) with prescribed k_f and D_f . Skorupski et al. [32] further improved this algorithm and developed a fast computational implementation. In this work, we have implemented the improved algorithm by following Skorupski et al. Figure 4.1 gives examples of the constructed fractal agglomerate with different D_f . Note that an increase in fractal dimension leads to a more dense structure of the agglomerate.

4

4.1.2. DIRECT SIMULATION MONTE CARLO

Direct simulation Monte Carlo (DSMC) [33] is a well-developed and widely applied technique for simulating rarefied gas flows, such as in aerodynamics in aerospace applications [34] and in microscale devices [35, 36]. In DSMC, the gas molecules are represented by so called DSMC parcels, with each parcel representing a usually very large number N_{eq} of real molecules. These parcels move and collide with each other in the simulated physical space. One essential feature of DSMC is the decoupling between the parcel movement and parcel–parcel collisions over a sufficiently small time interval. Upon collision, the parcels interchange momentum and energy according to a given collision model. Earlier work has extensively shown that DSMC gives a good representation of real rarefied gas flows [37]. For our model, we have chosen the variable soft sphere (VSS) [33] collision model for its accuracy in reproducing both the viscosity and diffusivity for the gas mixture.

4.1.3. MODELING ALD SURFACE REACTION

In reality, the ALD surface chemistry is rather complex, including nonideal ALD behaviors, such as the readsorption of gaseous products [38] and non-self-limiting behavior due to the decomposition of the surface species [6]. However, the aim of this work is to study the influence of fractal structure and gas rarefaction on the overall coating time. Therefore, here we adopt the ideal self-limiting ALD model based on the widely used concept of sticking coefficient. The sticking coefficient is defined as the reaction probability of a single precursor molecule with a reactive site on the surface. In order to mimic the self-limiting behavior, we use a similar methodology as adopted in earlier publications [27–29], based on the surface book-keeping approach. In this approach, the substrate surface is first divided into a number of surface elements. If one DSMC parcel, which represents N_{eq} number of real molecules, has reacted with a surface element, then the corresponding number of sites will be marked as “reacted” and extracted from the list of available sites of the element. Thus, for a parcel that hits a surface element, the

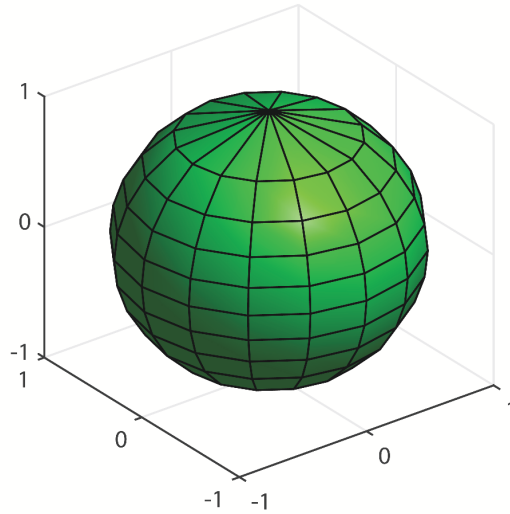


Figure 4.2: Surface of the nanoparticle is divided into 16×10 surface elements, each having the same surface area.

probability P_{rct} of it reacting with the element is

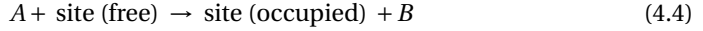
$$P_{rct} = f_i \cdot \gamma \quad (4.3)$$

where γ is the sticking coefficient and f_i is the number fraction of unoccupied sites among the total number of sites in the i th surface element. Therefore, when $f_i = 0$, the surface element is completely saturated and no more DSMC parcels can react with the element. In the present study, the surface of the spherical particle is divided into 160 surface elements as shown in Fig. 4.2, such that each element has the same surface area and thus the same number of sites.

4.2. COMPUTATIONAL SETUP

We have made the computational domain a cuboid box large just enough to contain the constructed agglomerate. Our simulation results proved to be insensitive to the precise size of the box, with coating times increasing by less than 2% for a 20% larger box size. During the simulation, the precursor is released from the boundaries of the domain with a fixed concentration and allowed to react with the agglomerate surface. The gas phase in an ALD reactor is typically a mixture of different gas species, such as the precursors, carrier gas, and gaseous products. Although it is possible to include all these different gas species in a DSMC simulation, the aim of the present study is not to model one particular

ALD process but rather to generically study the influence of fractal structure and gas rarefaction on the coating time. Therefore, we model the following generalized ALD half cycle reaction:



where A is the precursor which is transported with an inert carrier gas C , and B is the gaseous product. We use identical molecular properties (those of Argon [33]) for all three gas species A , B , and C for the sake of the simplicity. The computational domain is initially filled with gas molecules of C , and as the simulation starts, A is introduced from the domain boundaries with a constant number fraction of 10%. The number density of surface sites is set to $\rho_{\text{site}} = 1.132 \times 10^{18} / \text{m}^2$. Precise values of sticking coefficients are rarely found in literature, in spite of the wide use of the concept. Moreover, the sticking coefficient strongly depends on the substrate material and the operating temperature, which makes it even harder to obtain consistent data from literature. Rose et al. [39] reported that the sticking coefficient of tetrakis(ethylmethylamino)hafnium on hydroxyl groups depends exponentially on the substrate temperature, rendering 0.56 at 270 °C. We adopt these values for the sticking coefficient and temperature in our modeling. For such a high sticking coefficient, reaction is fast compared to diffusion for large N , and as a result, coating times are rather insensitive to the precise value of γ . This was confirmed in our study by increasing γ from 0.56 to 1.0, leading to small changes in coating time for large N .

The simulated spherical nanoparticles have a diameter of $2a = 90$ nm. With these particles, a series of fractal agglomerates are constructed by varying N from 4 to 2048, D_f from 2.1 to 2.5, with $k_f = 1.1$. For each combination of N and D_f , one realization of the agglomerate was studied. To check the sensitivity to geometrical differences between different realizations, we studied three different realizations for $N = 128$ and $D_f = 2.5$. Once constructed, each agglomerate is embedded in one computational domain using the DSMC cut-cell method [40, 41], which allows each and every single particle to be fully resolved. In all the conducted simulations, we fulfil the common DSMC criteria [42, 43] to ensure the accuracy of the results.

4.3. RESULTS AND DISCUSSIONS

4.3.1. INFLUENCE OF PRESSURE ON COATING TIME

ALD on particles can be carried out at low pressure [7] as well as at atmospheric pressure [44]. The level of gas rarefaction, i.e., the ratio between the mean free path and pore size, increases for decreasing pressure. Therefore, we first study the influence of pressure. For a fixed agglomerate with $k_f = 1.1$, $N = 1024$, and $D_f = 2.5$, the pressure is varied from 0.22 to 2.0 bar ($\lambda = 562 \sim 61.8$ nm). The overall coating time is non-dimensionalized with the time t_0 in which a surface element would be 99% coated when the precursor concentration at the surface would be kept the same as that of the domain boundaries.

This reference time t_0 can be computed by solving the following differential equation of f :

$$-\rho_{site} \frac{df}{dt} = \frac{1}{4} u_t C_A \gamma f \quad (4.5)$$

where ρ_{site} is the number density of surface sites, f is the number fraction of active sites, u_t is the molecular thermal velocity, and C_A is the precursor molecule number density. Equation (4.5) leads to the following expression for t_0 :

$$t_0 = \frac{\rho_{site}}{\frac{1}{4} u_t C_A \gamma} \ln(100) \quad (4.6)$$

which is of the order of 100 ns for 0.1 bar partial pressure of species A .

The choice of the length scale L in the definition of the Knudsen number is not so obvious: an agglomerate is a multi-scale structure with its smallest length scale being of the order of the particle radius a , and largest length scale being of the order of the overall agglomerate size R_g . To the best of our knowledge, it is not clear so far in literature what is the proper choice for L for this particular problem. Therefore, we have simply chosen the particle radius a as the reference length scale and the gas mean free path is non-dimensionalized into a Knudsen number by a . The molecular mean free path λ is computed from the variable soft sphere model as [33]

$$\lambda = \frac{\alpha(5-2\omega)(7-2\omega)}{5(\alpha+1)(\alpha+2)} u_t \frac{\mu}{P} = \frac{k}{P}, \quad k = 0.01236 \text{ (kg/s}^2\text{)} \quad (4.7)$$

where α is the exponent in the VSS model determined by the molecular properties, ω is the temperature exponent of viscosity, μ is the viscosity, and P is the pressure. As can be seen, λ is inversely proportional to P , and for the given range of P , it varies from $1.37a$ to $12.5a$.

Figure 4.3 shows the surface coverage of each particle of an agglomerate at time $t = 0.65t_0$ for $P = 0.22$ bar. It shows that the surface is not coated uniformly throughout the agglomerate. The outer particles are coated faster than the inner particles as can be expected intuitively. Figure 4.4 shows the overall surface coverage ϕ against the time t for different λ . As a reference case, a free molecular simulation is conducted by removing the molecular collisions from DSMC, i.e., $\lambda = \infty$. In general, when λ decreases, the overall coating time, normalized by that of a single particle, increases. The deviation from the free molecular results is only observable when λ is less than about $10a$. This suggests that for pressures below 0.1 bar, diffusion is well in the free molecular regime. Figure 4.5 shows the 99% overall saturation time $t_{99\%}$ against the different λ . It again shows that the normalized coating time decreases with increasing λ , and for $\lambda = 12.5a$, the saturation time is very close to that in the free molecular flow.

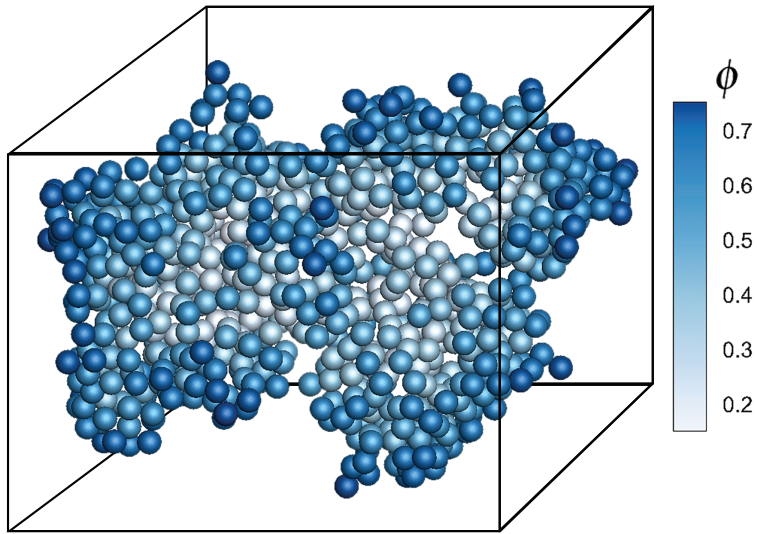


Figure 4.3: Surface coverage of each particle of the agglomerate, at $t = 0.65t_0$ for $P = 0.22$ bar. The cuboid outline represents the computational domain.

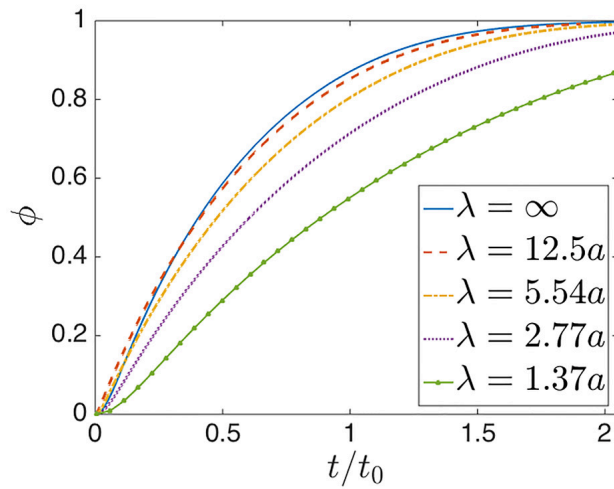


Figure 4.4: Overall surface coverage ϕ of the agglomerate against time t normalized by t_0 . $\lambda = \infty$ denotes a free molecular simulation where the molecular collision is not taken into account.

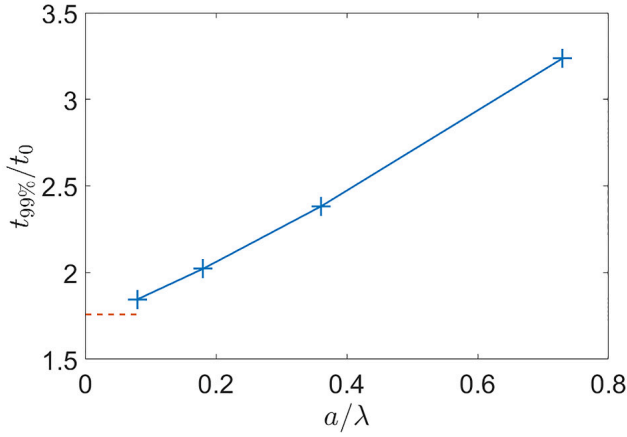


Figure 4.5: 99% saturation time $t_{99\%}$ normalized by t_0 , against the particle radius a normalized by the gas mean free path λ . The red dashed line represents the normalized $t_{99\%}$ in the free molecular regime, i.e., $\lambda = \infty$.

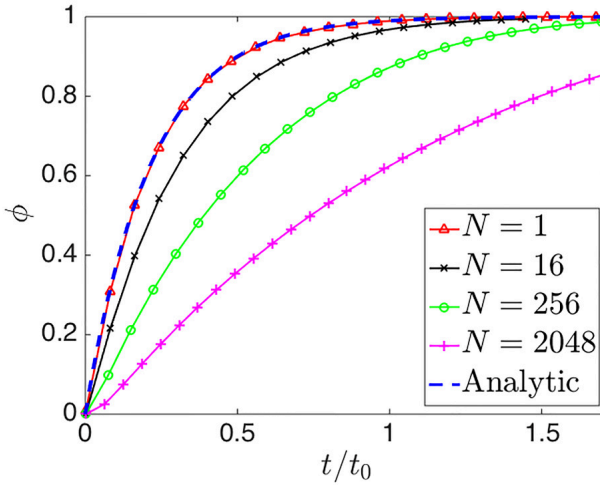


Figure 4.6: Overall surface coverage ϕ of the agglomerate against time t normalized by t_0 for a single particle, in comparison with the analytic expression in Eq. (4.5).

4.3.2. INFLUENCE OF AGGLOMERATE SIZE ON COATING TIME

In this section, the pressure is fixed at 1 bar ($\lambda = 2.77a$), and agglomerates with different number of particles ($1 \ll N \ll 2048$) are simulated with $k_f = 1.1$ and $D_f = 2.5$.

Figure 4.6 shows the overall surface coverage ϕ against time t for agglomerates with

different number of particles, in comparison with the analytic expression for ALD coating in the absence of diffusion limitations given in Eq. (4.5). The simulation results for $N = 1$ match very well with those analytic results, which indicates that for a single particle the system is well in the reaction-limited regime and can be accurately described by the analytic expression. As for the agglomerates, the overall coating time increases for increasing number of particles.

In order to analyze our results, and considering the resemblance between the gas diffusion in narrow holes and that in the pores of a porous agglomerate, we utilize the Gordon model [45], which was developed to predict ALD coating times in narrow holes and trenches.

The Gordon model analyzes a self-limiting ALD surface coating reaction in a long, narrow, cylindrical hole or trench. As time progresses, the length of the coated part of the hole wall increases from the hole mouth downward. The increment of time dt needed for coating an additional length dl in the hole is computed from the balance between the local flux and consumption by the hole side walls, i.e.,

$$F(l)A_{\perp}(l) \cdot dt = \rho_{site}a_v(l)A_{\perp}(l) \cdot dl \quad (4.8)$$

Here, $F(l)$ is the molecular precursor net flux entering the hole at depth l , A_{\perp} is the cross sectional area of the hole, ρ_{site} is the number of surface sites to be covered per unit area, and a_v is the wall surface area to be coated per unit volume of the hole. Thus, the total coating time T for the side walls of a hole of depth L is obtained as

$$T = \int_0^L dt = \rho_{site} \int_0^L \frac{1}{F(l)} a_v(l) dl \quad (4.9)$$

In the Gordon model for a cylindrical hole with radius r_p , a_v is not a function of l and equal to $a_v = 2/r_p$, and the precursor flux $F(l)$ inside the hole is expressed as a function of depth l as

$$F(l) = \frac{F_0}{1 + C_{CL} \frac{l}{r_p}} \quad (4.10)$$

with $F_0 = \frac{1}{4} u_t C_A$ the molecular flux at the mouth of the hole. The denominator in Eq. (4.10) is called Clausing factor [46], and it indicates how much the flux is reduced at a given depth l , compared to that at the entrance. The order 1 constant C_{CL} equals $3/8$ for cylindrical holes, and varies for different hole cross sectional shapes [47].

For quasi-spherical fractal agglomerates with $D_f > 2$ and radius of gyration R_g , we now consider the above model in a spherical coordinate system, with its origin ($r = 0$) defined at the center of mass of the agglomerate. Then, the coating penetration depth l is replaced by $(R_g - r)$. In a fractal agglomerate, the amount of reactive surface per unit

volume $a_v(r)$, as a function of radial position, is computed from

$$\begin{aligned} a_v(r) &= \frac{4\pi a^2 dN}{4\pi r^2 dr} \\ &= \frac{4\pi a^2 k_f D_f a^{-1} \left(\frac{r}{a}\right)^{D_f-1} dr}{4\pi r^2 dr} \\ &= k_f D_f a^{2-D_f} r^{D_f-3} \end{aligned} \quad (4.11)$$

This shows that in fractal agglomerates with $D_f < 3$, $a_v(r)$ decreases with increasing r , as the agglomerate becomes less dense with increasing r .

The aspect ratio $\frac{l}{r_p}$ of an agglomerate pore is estimated as

$$\begin{aligned} \frac{l}{r_p} &= \frac{a_v}{2} (R_g - r) \\ &= \frac{4\pi a^2 k_f \left(\frac{R_g}{a}\right)^{D_f}}{2 \cdot \frac{4}{3}\pi R_g^3} (R_g - r) \\ &= \frac{3}{2} k_f a^{2-D_f} R_g^{D_f-3} (R_g - r) \end{aligned} \quad (4.12)$$

By substituting Eqs. (4.11) and (4.12) into Eq. (4.9), and integrating from 0 to R_g , we get

$$\begin{aligned} t &= \int_0^t dt' \\ &= \frac{\rho_{site}}{F_0} \int_0^{R_g} \left[k_f D_f a^{2-D_f} r^{D_f-3} + \frac{3}{2} C_{CL} k_f^2 D_f a^{4-2D_f} R_g^{D_f-3} r^{D_f-3} (R_g - r) \right] dr \\ &= \frac{\rho_{site} k_f D_f}{F_0} \left(\frac{1}{D_f-2} \left(\frac{R_g}{a}\right)^{D_f-2} + \frac{3}{2} C_{CL} \frac{k_f}{(D_f-1)(D_f-2)} \left(\frac{R_g}{a}\right)^{2D_f-4} \right) \end{aligned} \quad (4.13)$$

with Eq. (4.1), this can be rewritten as

$$\begin{aligned} t &= \frac{\rho_{site}}{F_0} \left[\frac{D_f}{D_f-2} k_f^{\frac{2}{D_f}} N^{\frac{D_f-2}{D_f}} + \frac{3}{2} C_{CL} \frac{D_f}{(D_f-2)(D_f-1)} k_f^{\frac{4}{D_f}} N^{\frac{2D_f-4}{D_f}} \right] \\ &= k_1 N^{\frac{D_f-2}{D_f}} + k_2 N^{\frac{2D_f-4}{D_f}} \end{aligned} \quad (4.14)$$

In the Gordon model for a hole, the coating time for the bottom wall is added to Eq. (4.9) as a separate term, which gives the asymptotic value of $t = t_0$ when $l = 0$, i.e., when the hole depth is zero and deposition takes place on a flat surface. Similarly, in our model for deposition on a fractal agglomerate, this asymptotic value of $t = t_0$ should hold for $N = 1$. Therefore, we add a similar additional term to Eq. (4.14) to fulfill this requirement as

$$t/t_0 = k_1 N^{\frac{D_f-2}{D_f}} + k_2 N^{\frac{2D_f-4}{D_f}} + (1 - k_1 - k_2) \quad (4.15)$$

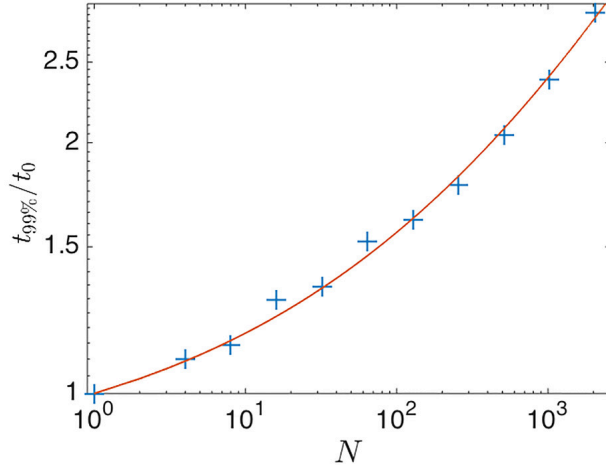


Figure 4.7: 99% saturation time $t_{99\%}$ normalized by t_0 against the number of particles N in an agglomerate. For $N = 128$, the saturation times for three different realizations of the agglomerates are shown, which are virtually identical. For all other N , only one realization is included. The red line represents a fitting according to Eq. (4.15) with $k_1 = 0.1414$ and $k_2 = 0.0655$.

with

$$\begin{aligned} k_1 &= \frac{\rho_{site}}{F_0} \frac{1}{D_f - 2} k_f^{\frac{2}{D_f}} D_f \frac{1}{t_0} \\ &= \frac{\gamma}{\ln(100)} \frac{D_f}{D_f - 2} k_f^{\frac{2}{D_f}} \end{aligned} \quad (4.16)$$

and

$$\begin{aligned} k_2 &= \frac{3}{2} C_{CL} \frac{\rho_{site}}{F_0} \frac{1}{(D_f - 2)(D_f - 1) k_f^{\frac{4}{D_f}} D_f \frac{1}{t_0}} \\ &= \frac{3}{2} C_{CL} \frac{\gamma}{\ln(100)} \frac{1}{(D_f - 2)(D_f - 1)} k_f^{\frac{4}{D_f}} D_f \end{aligned} \quad (4.17)$$

The ratio k_1/k_2 depends only on the geometrical properties of the fractal agglomerates, as

$$\frac{k_1}{k_2} = \frac{2}{3} \frac{1}{C_{CL}} (D_f - 1) k_f^{-\frac{2}{D_f}} \quad (4.18)$$

Our model predicts that for fractal agglomerates with $2 < D_f < 3$ and large N [when the last term in Eq. (4.13) dominates] the coating time t scales less than quadratically with the size of the agglomerate R_g (for example, for $D_f = 2.5$, t scales linearly with R_g). For nonfractal agglomerates (i.e., $D_f = 3$) and large N , our model predicts that the

coating time t scales quadratically with the size of the agglomerate R_g . This difference is due to the fact that for fractal agglomerates with $D_f < 3$ the void fraction increases when moving away from the center, while for $D_f = 3$ the void fraction is independent of radial position. It should be noted that for $D_f = 3$, our model is identical to the original Gordon model for a hole, which predicts a coating time proportional to the square of the hole depth.

For $D_f = 2.5$, Eq. (4.15) predicts $t/t_0 = k_1 N^{1/5} + k_2 N^{2/5} + (1 - k_1 - k_2)$. We fitted the constants k_1 and k_2 to simulated 99% saturation times $t_{99\%}$ for agglomerates with different number of particles ($1 \leq N \leq 2048$), $k_f = 1.1$ and $D_f = 2.5$, as shown in Fig. 4.7. As can be seen, the fitted curve matches the simulation data very well. It indicates that our generalized form of the Gordon model accurately predicts the scaling of the coating time of fractal agglomerates with increasing particle number. From our fitting to the data in Fig. 4.7, we find $k_1/k_2 = 2.16$, suggesting [with Eq. (4.18)] a value $C_{CL} = 0.43$ in the Clausen factor for $D_f = 2.5$, which appears to be a very reasonable value for our highly irregular pores.

With our above model, we can now estimate that for realistic fractal agglomerates with $N \sim 10^9$ and $D_f = 2.5$, the coating time would exceed that of a single particle by a factor of around 4000, as opposed to a factor 10^6 for a nonfractal agglomerate. This estimate, obviously, is highly sensitive to the precise value of the exponent in the second term on the rhs of Eq. (4.15), which we could not validate for very large N . Nevertheless, it is clear that the coating time for fractal agglomerates is orders of magnitude smaller than that of nonfractal agglomerates.

4.3.3. INFLUENCE OF FRACTAL DIMENSION ON COATING TIME

In this section, the pressure is fixed at 1 bar, with $\lambda = 2.77a$, and the fractal dimension D_f is varied from 2.1 to 2.5 with $k_f = 1.1$ and $N = 1024$.

Figure 4.8 shows the overall surface coverage against time t for different fractal dimensions. In general, the coating time increases for increasing fractal dimension. We compare the simulated 99% saturation time $t_{99\%}$ with the analytic expression in Eq. (4.15). For $D_f < 2.5$, the values of k_1 and k_2 have been computed from the fitted values of k_1 and k_2 for $D_f = 2.5$, using Eqs. (4.16) and (4.17) in which C_{CL} was kept constant for all D_f . This comparison is shown in Fig. 4.9. As can be seen, the simulation results agree very well with our model for $D_f \geq 2.3$, while some deviations are observable for $D_f < 2.3$. This indicates that values of k_1 and k_2 obtained for large D_f are inaccurate for smaller D_f , probably due to (1) changes in pore shape, leading to different C_{CL} , (2) break down of the assumption of a quasi-spherical agglomerate shape with an average pore size depending on radial position only, rather than a fully three dimensional pore size distribution.

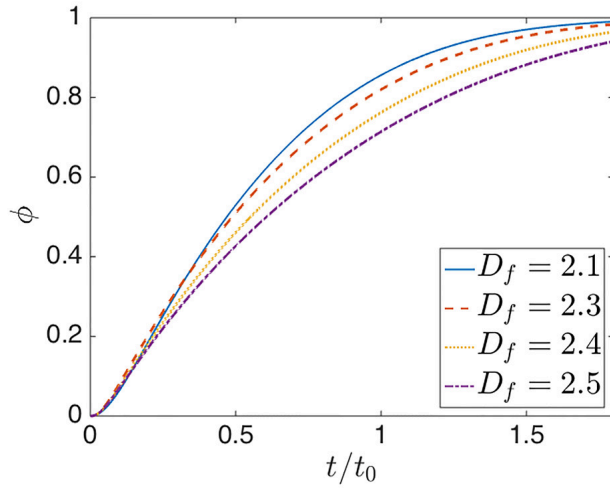


Figure 4.8: Overall surface coverage ϕ against time t normalized by t_0 for agglomerates with $k_f = 1.1$, $N = 1024$.

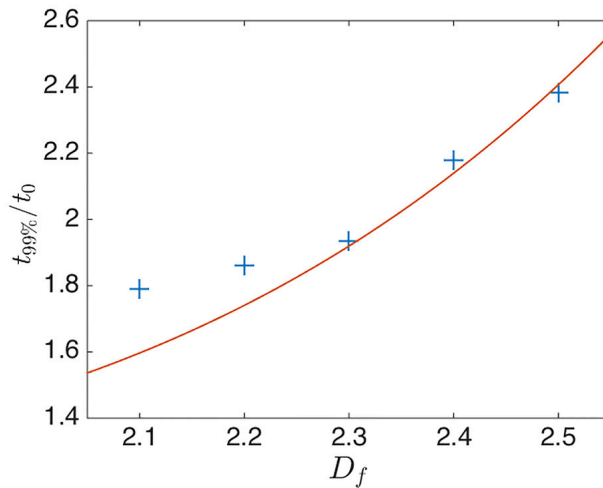


Figure 4.9: 99% saturation time normalized by t_0 against the fractal dimension D_f , for $k_f = 1.1$ and $N = 1024$. The red line represents the expression in Eq. (4.15), with the fitted k_1 and k_2 from Fig. 4.7.

4.4. SUMMARY AND CONCLUSIONS

We have developed a computational model for simulating atomic layer deposition on fractal nanoparticle agglomerates with fractal dimension $2 < D_f < 3$. This model accounts for a self-limiting ALD half cycle reaction and gas diffusion in the gas rarefied

regime within a fully resolved fractal agglomerate of spherical nanoparticles. We also derived a generalized form of the Gordon model which was developed for ALD coating within a cylindrical hole or trench. We extended this model to predict the ALD coating time within fractal agglomerates. Based on the present study with our model, we draw the following conclusions:

- The overall coating time of an agglomerate, normalized by that of a single particle, decreases for decreasing pressure, i.e., increasing gas mean free path λ , up to $\lambda \sim 10a$, whereas it becomes independent of the pressure for $\lambda > 10a$, with a the nanoparticle radius. This indicates that a is the proper length scale for calculating the Knudsen number for this particular problem. For pressures below 0.1 bar, diffusion in the simulated agglomerates is well in the free molecular regime, and further reduction of the pressure has a little influence on the normalized coating time.
- The overall coating time increases as the number of particles of an agglomerate increases. Our generalization of the Gordon model predicts the required coating time of a large agglomerate to scale with the number of particles to the power $(2D_f - 4)/D_f$, in excellent agreement with simulation results for agglomerates with $D_f = 2.5$. This model predicts that realistic agglomerates of $O(10^9)$ nanoparticles require coating times that are 3–4 orders of magnitude larger than for a single particle.
- The overall coating time increases for increasing fractal dimension D_f in agreement with our generalized Gordon model. The simulation results agree very well with our model for $D_f \geq 2.3$, while some deviations are observable for $D_f < 2.3$. The two model constants in our model were found to slightly depend on the fractal dimension.

REFERENCES

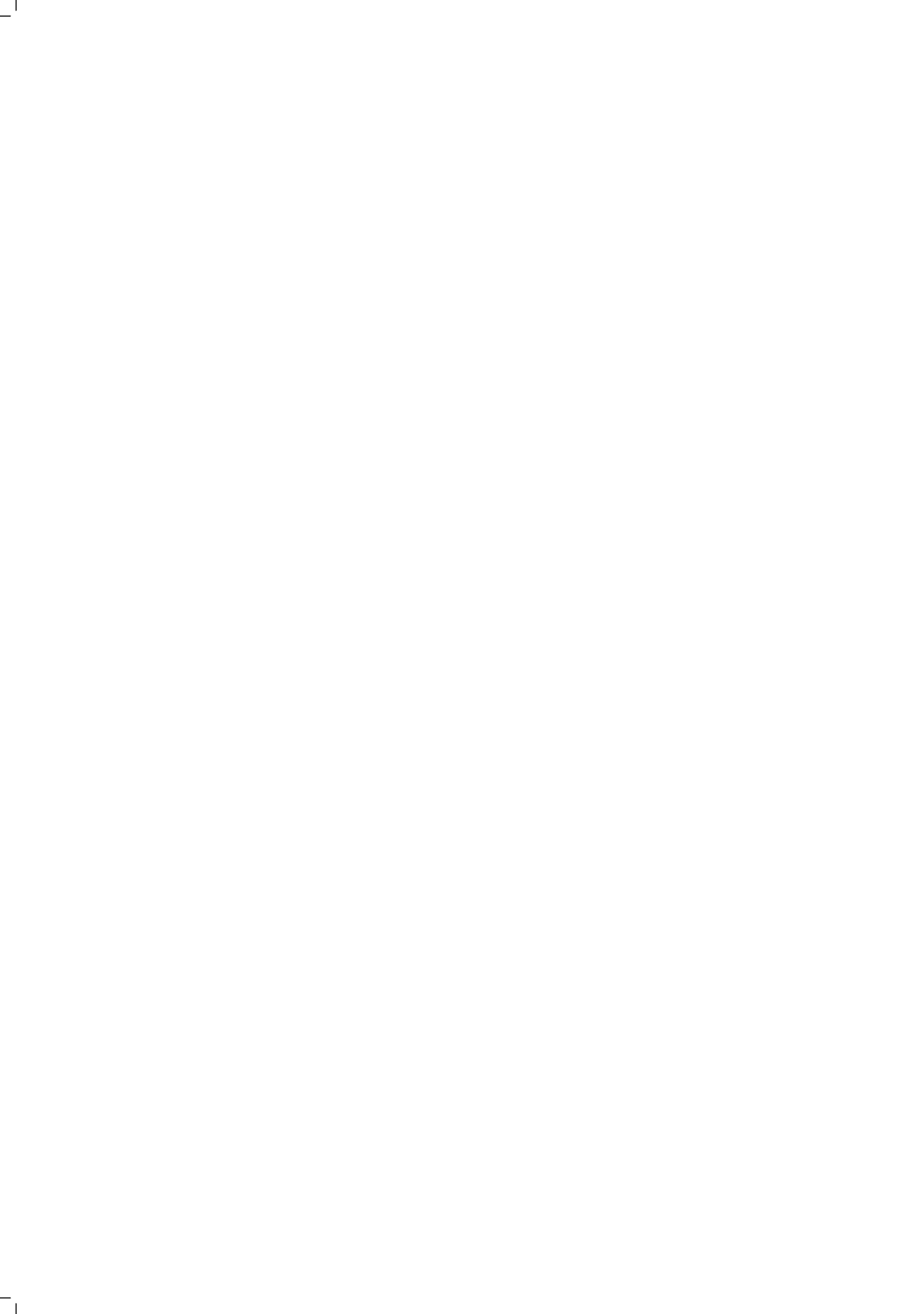
- [1] W. Jin, C. R. Kleijn, and J. R. van Ommen, *Simulation of atomic layer deposition on nanoparticle agglomerates*, Journal of Vacuum Science & Technology A: Vacuum, Surfaces, and Films **35**, 01B116+ (2017).
- [2] J. Li, X. Liang, D. M. King, Y.-B. Jiang, and A. W. Weimer, *Highly dispersed Pt nanoparticle catalyst prepared by atomic layer deposition*, Applied Catalysis B: Environmental **97**, 220 (2010).
- [3] A. Goulas and J. R. van Ommen, *Scalable Production of Nanostructured Particles using Atomic Layer Deposition*, KONA Powder and Particle Journal **31**, 234 (2014).
- [4] W. E. Bawarski, E. Chidlow, D. J. Bharali, and S. A. Mousa, *Emerging nanopharmaceuticals*, Nanomedicine: Nanotechnology, Biology and Medicine **4**, 273 (2008).

- [5] J. W. Elam, N. P. Dasgupta, and F. B. Prinz, *ALD for clean energy conversion, utilization, and storage*, MRS Bulletin **36**, 899 (2011).
- [6] S. M. George, *Atomic Layer Deposition: An Overview*, Chemical Reviews, Chem. Rev. **110**, 111 (2010).
- [7] L. F. Hakim, S. M. George, and A. W. Weimer, *Conformal nanocoating of zirconia nanoparticles by atomic layer deposition in a fluidized bed reactor*, Nanotechnology **16**, S375 (2005).
- [8] D. Valdesueiro, G. Meesters, M. Kreutzer, and J. van Ommen, *Gas Phase Deposition of Ultrathin Aluminium Oxide Films on Nanoparticles at Ambient Conditions*, Materials **8**, 1249 (2015).
- [9] van Ommen, J. Valverde, and R. Pfeffer, *Fluidization of nanopowders: a review*, Journal of Nanoparticle Research **14**, 1 (2012).
- [10] L. de Martín, A. Fabre, and J. R. van Ommen, *The fractal scaling of fluidized nanoparticle agglomerates*, Chemical Engineering Science **112**, 79 (2014).
- [11] L. de Martín, W. G. Bouwman, and J. R. van Ommen, *Multidimensional Nature of Fluidized Nanoparticle Agglomerates*, Langmuir **30**, 12696 (2014).
- [12] F. Grillo, M. T. Kreutzer, and J. R. van Ommen, *Modeling the precursor utilization in atomic layer deposition on nanostructured materials in fluidized bed reactors*, Chemical Engineering Journal **268**, 384 (2015).
- [13] E. W. Thiele, *Relation between Catalytic Activity and Size of Particle*, Ind. Eng. Chem. **31**, 916 (1939).
- [14] R. Krishna, *Describing the Diffusion of Guest Molecules Inside Porous Structures*, J. Phys. Chem. C **113**, 19756 (2009).
- [15] M.-O. Coppens and G. F. Froment, *Diffusion and reaction in a fractal catalyst pore—I. Geometrical aspects*, Chemical Engineering Science **50**, 1013 (1995).
- [16] F. J. Keil, *Diffusion and reaction in porous networks*, Catalysis Today **53**, 245 (1999).
- [17] F. J. Keil, *Multiscale Modelling in Computational Heterogeneous Catalysis*, in *Multiscale Molecular Methods in Applied Chemistry*, Topics in Current Chemistry, Vol. 307, edited by B. Kirchner and J. Vrabec (Springer Berlin Heidelberg, 2012) pp. 69–107.
- [18] M. Sahimi, G. R. Gavalas, and T. T. Tsotsis, *Statistical and continuum models of fluid-solid reactions in porous media*, Chemical Engineering Science **45**, 1443 (1990).

- [19] J. A. H. Dreyer, N. Riefler, G. R. Pesch, M. Karamehmedović, U. Fritsching, W. Y. Teoh, and L. Mädler, *Simulation of gas diffusion in highly porous nanostructures by direct simulation Monte Carlo*, *Chemical Engineering Science* **105**, 69 (2014).
- [20] G. L. Vignoles, *Modelling Binary, Knudsen and Transition Regime Diffusion Inside Complex Porous Media*, *Le Journal de Physique IV* **05**, C5 (1995).
- [21] N. Reuge and B. Caussat, *Modeling of Silicon CVD into Agglomerates of Sub-micrometer-size Particles in a Fluidized Bed*, *Chemical Vapor Deposition* **17**, 305 (2011).
- [22] A. M. Lankhorst, B. D. Paarhuis, H. J. C. M. Terhorst, P. J. P. M. Simons, and C. R. Kleijn, *Transient ALD simulations for a multi-wafer reactor with trenched wafers*, *Surface and Coatings Technology* **201**, 8842 (2007).
- [23] E. Chassaing and B. Sapoval, *Electrochemical Impedance of Blocking Quasi Fractal 3d Electrodes*, *Journal of The Electrochemical Society* **141**, 2711 (1994).
- [24] P. Meakin and B. Sapoval, *Random-walk simulation of the response of irregular or fractal interfaces and membranes*, *Physical Review A* **43**, 2993 (1991).
- [25] D. S. Grebenkov, M. Filoche, and B. Sapoval, *A simplified analytical model for laplacian transfer across deterministic prefractal interfaces*, *Fractals* **15**, 27 (2007).
- [26] G. R. Pesch, N. Riefler, U. Fritsching, L. Colombi Ciacchi, and L. Mädler, *Gas-solid catalytic reactions with an extended DSMC model*, *AIChE Journal* **61**, 2092 (2015).
- [27] J. Dendooven, D. Deduytsche, J. Musschoot, R. L. Vanmeirhaeghe, and C. Detavernier, *Modeling the Conformality of Atomic Layer Deposition: The Effect of Sticking Probability*, *Journal of The Electrochemical Society* **156**, P63 (2009).
- [28] H. C. M. Knoops, E. Langereis, M. C. M. van de Sanden, and W. M. M. Kessels, *Conformality of Plasma Assisted ALD: Physical Processes and Modeling*, *Journal of The Electrochemical Society* **157**, G241 (2010).
- [29] M. Rose and J. W. Bartha, *Method to determine the sticking coefficient of precursor molecules in atomic layer deposition*, *Applied Surface Science* **255**, 6620 (2009).
- [30] S. K. Friedlander, *Smoke, dust, and haze : fundamentals of aerosol dynamics*, 2nd ed. (Oxford Univ. Press, 2000).
- [31] A. V. Filippov, M. Zurita, and D. E. Rosner, *Fractal-like Aggregates: Relation between Morphology and Physical Properties*, *Journal of Colloid and Interface Science* **229**, 261 (2000).
- [32] K. Skorupski, J. Mrocza, T. Wriedt, and N. Riefler, *A fast and accurate implementation of tunable algorithms used for generation of fractal-like aggregate models*, *Physica A: Statistical Mechanics and its Applications* **404**, 106 (2014).

- [33] G. A. Bird, *Molecular gas dynamics and the direct simulation of gas flows*, 2nd ed. (Clarendon Press, 2003).
- [34] E. S. Oran, C. K. Oh, and B. Z. Cybyk, *DIRECT SIMULATION MONTE CARLO: Recent Advances and Applications*, *Annual Review of Fluid Mechanics* **30**, 403 (1998).
- [35] Z. C. Hong, C. E. Zhen, and C. Y. Yang, *Fluid Dynamics and Heat Transfer Analysis of Three Dimensional Microchannel Flows with Microstructures*, *Numerical Heat Transfer, Part A: Applications* **54**, 293 (2008).
- [36] H. Akhlaghi, E. Roohi, and S. Stefanov, *A new iterative wall heat flux specifying technique in DSMC for heating/cooling simulations of MEMS/NEMS*, *International Journal of Thermal Sciences* **59**, 111 (2012).
- [37] G. A. Bird, *Recent advances and current challenges for DSMC*, *Computers & Mathematics with Applications* **35**, 1 (1998).
- [38] M. Ritala, M. Leskela, L. Niinisto, and P. Haussalo, *Titanium isopropoxide as a precursor in atomic layer epitaxy of titanium dioxide thin films*, *Chem. Mater.* **5**, 1174 (1993).
- [39] M. Rose, J. W. Bartha, and I. Endler, *Temperature dependence of the sticking coefficient in atomic layer deposition*, *Applied Surface Science* **256**, 3778 (2010).
- [40] C. Zhang and T. E. Schwartzentruber, *Robust cut-cell algorithms for DSMC implementations employing multi-level Cartesian grids*, *Computers & Fluids* **69**, 122 (2012).
- [41] M. C. Lo, C. C. Su, J. S. Wu, and F. A. Kuo, *Development of parallel direct simulation Monte Carlo method using a cut-cell Cartesian grid on a single graphics processor*, *Computers & Fluids* **101**, 114 (2014).
- [42] A. L. Garcia and W. Wagner, *Time step truncation error in direct simulation Monte Carlo*, *Physics of Fluids* **12**, 2621 (2000).
- [43] Z.-X. Sun, Z. Tang, Y.-L. He, and W.-Q. Tao, *Proper cell dimension and number of particles per cell for DSMC*, *Computers & Fluids* **50**, 1 (2011).
- [44] R. Beetstra, U. Lafont, J. Nijenhuis, E. M. Kelder, and J. R. van Ommen, *Atmospheric Pressure Process for Coating Particles Using Atomic Layer Deposition*, *Chemical Vapor Deposition* **15**, 227 (2009).
- [45] R. G. Gordon, D. Hausmann, E. Kim, and J. Shepard, *A Kinetic Model for Step Coverage by Atomic Layer Deposition in Narrow Holes or Trenches*, *Chemical Vapor Deposition* **9**, 73 (2003).
- [46] P. Clausing, *The Flow of Highly Rarefied Gases through Tubes of Arbitrary Length*, *Journal of Vacuum Science and Technology* **8**, 636 (1971).

- [47] P. J. Lobo, F. Becheri, and J. Gómez-Goñi, *Comparison between Monte Carlo and analytical calculation of Clausing functions of cylindrical and conical tubes*, *Vacuum* **76**, 83 (2004).



5

MOVING REACTION FRONTS IN FRACTAL NANOPARTICLE AGGLOMERATES

Self-limiting gas-surface reactions lead to reaction fronts that penetrate nanoporous materials with a finite speed. We present a closed form theoretical model, validated against molecular simulations, that shows the influence of the fractal scaling law on the time needed to fully penetrate fractal agglomerates of nanoparticles. For very large agglomerate sizes, this penetration time scales with the number of particles N in the agglomerate as $N^{\frac{D_f-1}{D_f}}$. The penetration time for agglomerates with fractal dimensions $D_f < 3$ may therefore be orders of magnitude smaller than for non-fractal porous materials.

5.1. INTRODUCTION

The interplay between gaseous diffusion inside nanoporous solids, and self-limiting reactions at pore wall sites (i.e. reactions that render these sites inactive after they have been occupied by a reacted gas molecule) is of great relevance for applications in for instance catalyst deactivation [1], CO₂ storage [2] and conformal coating of agglomerated nanoparticles [3–5]. In these applications, the time needed for the reacting gas to fully penetrate the porous solid and saturate its surfaces is vital to the efficiency of the material and the process.

The time required for gas molecules to be transported through straight narrow pores with diameters that are small compared to the mean free path of the gas was first analysed in the seminal work by Knudsen [6], and extended to more complex pore networks and wall surface morphologies in many later studies [7, 8]. When the gas molecules react with the pore walls, a chemical reaction time scale is added to the problem [9, 10] and the ratio between the two time scales, the so-called Thiele modulus [11], governs the effective reactivity of the pore in applications such as in porous catalysts [9], adsorption [12] and separation [13] processes.

For self-limiting surface processes, however, the interaction between Knudsen diffusion and surface reaction is of a different nature, as it now leads to a moving front between reacted and unreacted wall surface. The time needed for this front to travel through the material was analysed for simple straight pores, particularly because of its relevance in micro electronics processing [14–17], but has not been studied for the complex pore networks found in most natural or fabricated nanoporous materials [18].

In this paper, we focus on agglomerates of mono-sized spherical nanoparticles as an important class of nanoporous materials. Unlike regularly structured nanoporous materials [19], such agglomerates possess intrinsic randomness in their microscopic geometrical construction and do not exhibit closed pores [20], causing gas diffusion inside to be normal. Also, such agglomerates have been found to possess a fractal nature [21, 22]. The number of particles N in the agglomerate scales with the size of the agglomerate according to

$$N = k_f \left(\frac{R_g}{a} \right)^{D_f} \quad (5.1)$$

where k_f is an $O(1)$ constant, R_g is the agglomerate gyration radius, a is the radius of the primary nanoparticles, and D_f is the fractal dimension. It is important to note that Eq. (5.1) does not uniquely define an agglomerate. In fact, $O(3N)$ particle center coordinates are needed to fully define the microscopic arrangement of the N particles in an agglomerate. As a result, many different agglomerates are characterized by the same N , D_f , k_f and (R_g/a) . All these agglomerates will be different in respect to the detailed arrangement of their constituent particles, and as a result will exhibit different microscopic diffusion behavior at the particle and void scale. However, in this paper we will demonstrate that for the prediction of the overall saturation time it is sufficient to char-

acterize the agglomerate on a low-dimensional parameter space, since to first order the saturation time is determined by the scale invariance D_f and the agglomerate size N , in addition to the parameters k_f and (R_g/a) . We present a theoretical model showing this dependence, validated by molecular simulations inside agglomerates, as well as regime maps that teach how t_{agg} scales with N and D_f .

5.2. THEORY

We first derive a theoretical model for predicting the overall agglomerate saturation time t_{agg} , defined here as the time required to saturate 99% of all nanoparticle surface sites within the agglomerate. For a single nanoparticle exposed to a fixed reactant concentration C_0 at its surface, such a 99% surface coverage is reached in a time $t_0 = \frac{\rho_{site}}{\frac{1}{4}u_t C_0 \gamma} \ln(100)$ (a detailed derivation is shown in section 4.2.1), where ρ_{site} is the number density of surface sites, u_t is the molecular mean thermal velocity and γ is the surface reaction sticking coefficient.

For a multi-particle agglomerate, t_{agg} increases from t_0 due to the uneven exposure of the particle surfaces. This is governed by the interplay between two independent time scales namely 1) the time t_M in which molecules, in the absence of reactions, diffuse to the core of the agglomerate, and 2) the time t_F in which the reaction front reaches the core of the agglomerate, assuming that gas molecules travel infinitely fast. In the following, we will derive expressions for both t_F and t_M , combined into a closed form theoretical model for the agglomerate saturation time t_{agg} .

Our model for t_F is inspired by Gordon's model [14] for simple straight pores and trenches¹. For a narrow cylindrical pore with radius r_p and length L , Gordon computes t_F based on a local mass balance between the gas molecule flux $F(l)$ and the consumption of gas molecules at the pore walls, both taken at a depth l inside the pore, with $0 \leq l \leq L$, as:

$$F(l)A_{\perp}(l) \cdot dt = \rho_{site}a_v(l)A_{\perp}(l) \cdot dl \quad (5.2)$$

where $A_{\perp}(l)$ is the cross sectional area of the hole and $a_v(l)$ is the wall surface area per unit volume of the pore. Thus, t_F for a pore is obtained as

$$t_F = \rho_{site} \int_0^L \frac{1}{F(l)} a_v(l) dl \quad (5.3)$$

An approximate expression for $F(l)$ has been proposed by Clausing [23], and is reformulated here in terms of the Knudsen diffusivity D_k as

$$F(l) = \frac{F_0}{1 + \frac{u_t l}{4D_k}} \quad (5.4)$$

¹It should be noted that, in Gordon's model, it is implicitly assumed that $t_F \gg t_M$, and thus t_F equals the total saturation time.

where $F_0 = \frac{1}{4} u_t C_0$ is the flux at the entrance of the hole, and for a long cylindrical hole $D_k = \frac{2}{3} r_p u_t$ [6].

We now develop a model for computing t_F inside fractal agglomerates, again starting from the mass balance as in Eq. (5.2) that leads to Eq. (5.3). Thus, we need to compute $F(l)$ and $a_v(l)$ for fractal agglomerates.

In order to compute $F(l)$ from Eq. (5.3), we first derive an approximate expression for D_k , taking into account the high degree of randomness in naturally grown nanoparticle agglomerates. For a system consisting of large number ($N \gg 1$) of randomly dispersed hard spheres, it has been shown in literature [24, 25] that the diffusion is normal and D_k can be expressed as,

$$D_k = \frac{1}{3} \langle \lambda \rangle u_t \left(\frac{\langle \lambda^2 \rangle}{2 \langle \lambda \rangle^2} - \beta \right) \quad (5.5)$$

where λ is the chord length defined as the length of a segment that entirely lies in the void space with two ends on particle surfaces, β is the angular factor which accounts for the average angle between two consecutive molecular trajectories, and $\langle \dots \rangle$ denotes average over the entire domain. For fully diffusive surfaces, it has been shown that $\beta = \frac{4}{13}$ [24]. For randomly dispersed hard spheres, the distribution of λ is well expressed with an exponential form [26, 27] which leads to

$$\frac{\langle \lambda^2 \rangle}{2 \langle \lambda \rangle^2} = 1 \quad (5.6)$$

and

$$\langle \lambda \rangle = \frac{4a(1 - \phi_s)}{\phi_s} \quad (5.7)$$

where ϕ_s is the solid volume fraction. For a homogeneous system, such as the randomly dispersed spheres, ϕ_s is independent of the location and thus D_k is uniform everywhere. Although, this may not strictly hold for a fractal agglomerate due to the constraint from D_f . We use Eqs. (5.5)-(5.7) using a global value of ϕ_s to compute a global D_k .

In order to compute the global ϕ_s , we evaluate the total space taken by the agglomerate as the volume of an equivalent sphere with radius R . Here, the choice of R is somewhat arbitrary due to the irregular shape of fractal agglomerates. Nevertheless, R is a linear measure of the size of the agglomerate, much alike R_g , and thus we argue that $R = \alpha R_g$, with α being an $O(1)$ constant for fixed D_f . This α is the only fitting parameter in our model and the choice of α will be discussed later. Now we can compute ϕ_s as,

$$\phi_s = \frac{\frac{4}{3} \pi a^3 N}{\frac{4}{3} \pi R^3} \quad (5.8)$$

We now consider the agglomerate in spherical coordinates with its origin ($r = 0$) at the mass center of the agglomerate. We model this system as such that the propagation

of reaction fronts start from $r = R$ and ends at $r = a$. Then, using Eq. (5.4), $F(r)$ can be computed as,

$$F(r) = \frac{F_0}{1 + \frac{u_t}{4 \cdot 3 D_k} (R - r)} \quad (5.9)$$

Here following [28], compared to Eq. 5.4, D_k is multiplied by a factor 3 to account for the fact that diffusion takes place in 3 dimensions rather than along the radial direction only.

The amount of reactive surface per unit void volume $a_v(r)$, as a function of the radial position r , can be computed as

$$\begin{aligned} a_v(r) &= \frac{4\pi a^2 dN}{4\pi r^2 dr - \frac{4}{3}\pi a^3 dN} \\ &= \frac{1}{\frac{\alpha^{D_f} a^{D_f-2}}{k_f D_f} r^{3-D_f} - \frac{1}{3} a} \end{aligned} \quad (5.10)$$

Now we can compute t_F by substituting Eqs. (5.5)-(5.10) into Eq. (5.3),

$$\begin{aligned} t_F &= \frac{\rho_{site}}{F_0} \int_a^R \frac{1}{\frac{\alpha^{D_f} a^{D_f-2}}{k_f D_f} r^{3-D_f} - \frac{1}{3} a} \cdot \\ &\quad \left[1 + \frac{13}{48} \frac{1}{\frac{\alpha^{D_f} a^{D_f-2}}{k_f} R^{3-D_f} - a} (R - r) \right] dr + T_F \end{aligned} \quad (5.11)$$

where T_F is calculated from the condition that $t_F = 0$ at $N = 1$. This term addresses the discontinuity in the fractal scaling law at small N , i.e. when $N \rightarrow 1$, $R \neq a$.

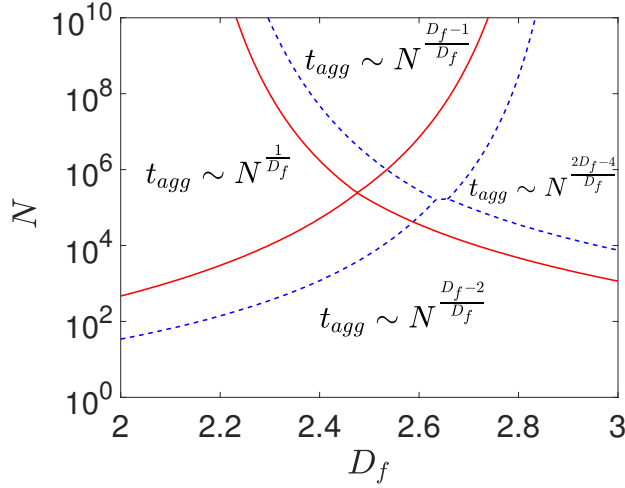
For large agglomerates with $N^{\frac{3-D_f}{D_f}} \gg k_f^{\frac{3}{D_f}} \alpha^{-3}$ and $2 < D_f < 3$, Eq. (5.11) can be simplified to (see Appendix for detailed derivations),

$$t_F = k_1 N^{\frac{D_f-2}{D_f}} + k_2 N^{\frac{2D_f-4}{D_f}} \quad (5.12)$$

with constants $k_1 = \frac{\rho_{site}}{F_0} k_f^{\frac{2}{D_f}} \frac{D_f}{D_f-2} \alpha^{-2}$ and $k_2 = \frac{13}{48} \frac{\rho_{site}}{F_0} k_f^{\frac{4}{D_f}} \frac{D_f}{(D_f-2)(D_f-1)} \alpha^{-4}$. Eq. (5.12) clearly shows the scaling of t_F with N for large fractal agglomerates.

For the computation of t_M , the surface reactions are not taken into account. When R is of the same order as λ , reactant molecules almost directly reach the central particles without colliding with other particles, thus $t_M = \frac{R-a}{u_t}$, whereas when $R \gg \lambda$, the molecules undergo pure diffusive paths and thus $t_M = \frac{1}{6} \frac{(R-a)^2}{D_k}$. Therefore, for any given R , t_M is computed as,

$$t_M = \frac{R-a}{u_t} + \frac{1}{6} \frac{(R-a)^2}{D_k} + T_M \quad (5.13)$$



5

Figure 5.1: Regime map for the scaling of the agglomerate saturation time t_{agg} with the agglomerate size N . The division lines between the four regimes have been calculated from the non-simplified model Eqs. (5.11), (5.13) and (5.15), using $\alpha = 1.47$ and $a = 45$ nm with $k_f = 1.1$ (red lines) and $k_f = 0.57$ (blue dashed lines).

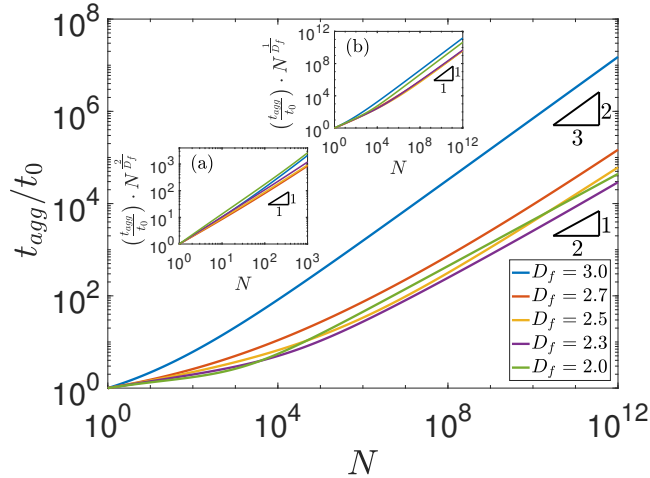


Figure 5.2: Main panel: Agglomerate saturation time t_{agg} , normalized by t_0 , against N . Inset (a): illustration of $t_{agg} \sim N^{\frac{D_f-2}{D_f}}$ for small N . Inset (b): illustration of $t_{agg} \sim N^{\frac{D_f-1}{D_f}}$ for large N . For all cases $k_f = 1.1$, $a = 45$ nm; $\alpha = 1.47$ for $2.0 \leq D_f \leq 2.7$ and $\alpha = 1.29$ for $D_f = 3.0$.

where T_M is calculated from the condition that $t_M = 0$ at $N = 1$. Again, for large ag-

glomerates with $N^{\frac{3-D_f}{D_f}} \gg k_f^{\frac{3}{D_f}} \alpha^{-3}$ and $2 < D_f < 3$, Eq. (5.13) can be simplified to (see Appendix for detailed derivations),

$$t_M = k_3 N^{\frac{1}{D_f}} + k_4 N^{\frac{D_f-1}{D_f}} \quad (5.14)$$

with $k_3 = k_f^{-\frac{1}{D_f}} \alpha \frac{a}{u_t}$ and $k_4 = \frac{13}{72} k_f^{\frac{1}{D_f}} \alpha^{-1} \frac{a}{u_t}$

Now, following the classical approach in analyzing confined reaction-diffusion problem [29], we consider molecular diffusion in the absence of reactions, and reaction front movement in the absence of diffusion limitations as two independent contributions to the time scale for reaction front penetration. Thus we find t_{agg} as

$$t_{agg} = \sqrt{t_M^2 + t_F^2} + t_0 \quad (5.15)$$

Eqs. (5.11), (5.13) and (5.15) constitute a closed form theoretical model for t_{agg} as a function of k_f , D_f , a and N . The only unknown is the $O(1)$ constant α . For non-fractal spherical agglomerates with $D_f = 3$, α can be exactly computed from that of a solid sphere as $\alpha = \frac{R}{R_g} = \sqrt{\frac{5}{3}} \sim 1.29$. For stochastically generated fractal agglomerates based on cluster-cluster aggregation [30] with $2.0 \leq D_f \leq 2.7$, we will show that $\alpha \sim 1.47$. For large agglomerates with $2 < D_f < 3$, our model simplifies to Eqs. (5.12), (5.14) and (5.15). This simplified model teaches that there are four different regimes for the scaling of the agglomerate saturation time t_{agg} with the agglomerate size N . These regimes are shown in

Fig. 5.1. For very large N and $2 < D_f < 3$, t_{agg} scales as $N^{\frac{D_f-1}{D_f}}$, and consequently fractal agglomerates are penetrated orders of magnitude faster than non-fractal agglomerates. This is illustrated in Fig 5.2. This figure also shows, in line with the regime map of Fig. 5.1, that t_{agg} scales with $N^{\frac{D_f-1}{D_f}}$ for large N , and approximately with $N^{\frac{D_f-2}{D_f}}$ for small N (small deviations in the latter are due to the fact that scaling law Eqs. (5.12) and (5.14) do not strictly hold for small N).

Here it should be noted that realistic nanoparticle agglomerates may easily contain over 10^{10} particles [31].

5.3. SIMULATIONS

We validated our theoretical model predictions by carrying out numerical simulations. We generated agglomerates for various sets of k_f , D_f and N , using three different particle agglomerate generation algorithms adopted from literature [30, 32].

First, we used the algorithm by Filippov [30] to generate randomly structured fractal agglomerates with prescribed k_f and D_f . Here an agglomerate is generated by repeating

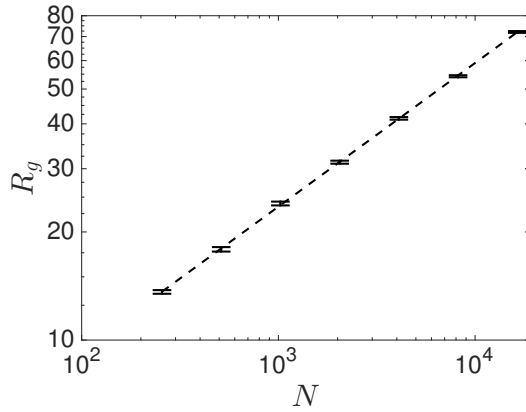


Figure 5.3: R_g against N , averaged over 40 different realizations of DLA agglomerates. The error bars denote 95% confidence interval for R_g and the fitted dashed line represents $k_f = 0.37$ and $D_f = 2.5$.

5

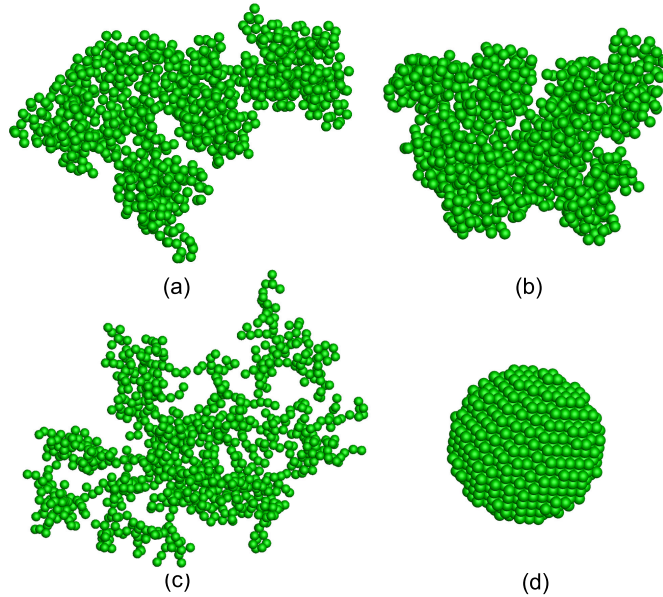


Figure 5.4: (a)-(b): Single realization of stochastically generated fractal agglomerates with $N = 1024$, $k_f = 1.1$ and $D_f = 2.3$ (a), $D_f = 2.5$ (b). (c): Single realization of a DLA agglomerate with $N = 1024$, $k_f = 0.37$ and $D_f = 2.5$. (d): Deterministically generated spherical agglomerate, with body-centered cubic particle arrangement, for $N = 1067$, $k_f = 1.1$ and $D_f = 3$.

the process of combining two equally sized different sub-agglomerates until the desired

N is reached, subject to only two constraints: (i) the new agglomerate, after each combination, should exactly fulfill the fractal scaling law, and (ii) particles do not overlap with each other. All the other particle location parameters are chosen randomly. For each set of k_f , D_f and N , three different realizations of the agglomerate were generated and studied.

Secondly, we also generated agglomerates with a, more physically realistic, so called Diffusion-Limited Aggregation (DLA) [33, 34] algorithm². This method starts with a seed particle at the center of the domain, and injects Brownian particles into the domain one by one. Each injected particle will then either hit and stick to the seed particle and become part of the agglomerate, or escape the domain without hitting the seed particle(s). This procedure is continued until the number of particles in the agglomerate reaches pre-specified N . Unlike the random agglomerates, using DLA algorithm one cannot exactly control k_f and D_f for each individual realization of agglomerate, but rather the reported k_f and D_f are ensemble averages over many different realizations. In this work, we have averaged over 40 different realizations of each N , which renders $k_f = 0.37$ and $D_f = 2.5$, as shown in Fig 5.3.

Thirdly, we also deterministically constructed non-fractal ($D_f = 3$) spherical agglomerates with body-centered cubic and simple cubic particle arrangements, for different solid volume fractions $\phi_s = (\frac{3}{5})^{\frac{3}{2}} k_f$.

Fig. 5.4 shows examples of constructed agglomerates with all three agglomerate generation algorithms described above and different D_f .

Once generated, an agglomerate is placed in a cuboid domain which is large just enough to contain it. We then perform free molecular simulations, using a direct simulation Monte Carlo (DSMC) code for rarefied gas flows with intermolecular collisions switched off [35, 36]. Molecules are released from the domain boundaries and undergo ballistic trajectories into the agglomerate until either sticking to a particle surface, or escaping the domain. Upon collision with a particle, molecules have a probability γ to react with the surface. For bookkeeping their surface site occupancy, the surface of each nano-particle is partitioned into 160 equal sized elements. After reacting with one simulated molecule, a surface element is occupied and will diffusively bounce back all subsequent impinging molecules. Following the common DSMC philosophy, one simulated molecule represents a number N_M of real molecules, with $N_M = O(10^2)$ in the present study. When, correspondingly, one surface element represents N_M surface sites, our results do not depend on the value of N_M . Fig. 5.5 shows an instantaneous overall surface coverage fraction per particle for an agglomerate from one such simulation.

Now we compare our theoretical results (computed from Eqs. (5.11), (5.13) and (5.15)) with our numerical simulations. For this comparison, we have set $a = 45$ nm and $\gamma = 1$ (see Supplemental Material² for discussion on $\gamma < 1$).

²<http://markjstock.org/dla-nd/>

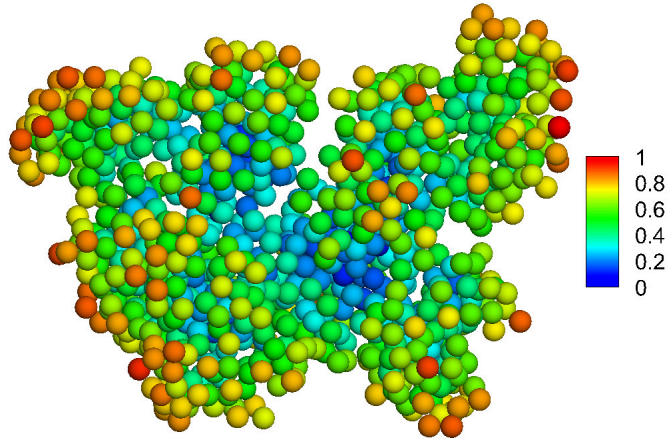


Figure 5.5: Overall surface coverage per particle for $k_f = 1.1$, $D_f = 2.5$ and $N = 1024$, at $t = t_0$, showing about 50% overall coverage. A movie showing the evolution of the surface coverage in time is provided in the Supplemental Material [30].

5

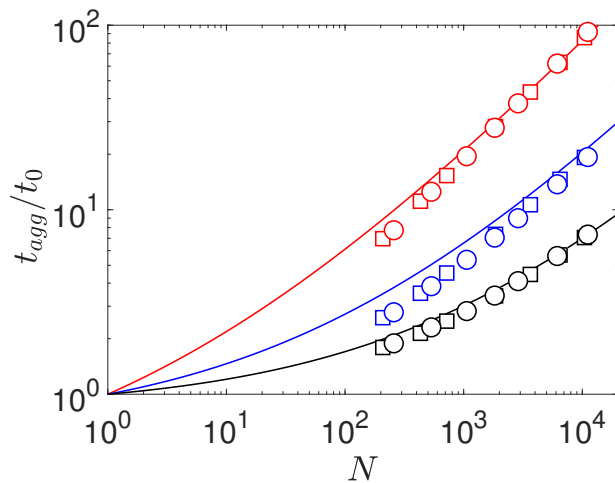


Figure 5.6: Agglomerate saturation time t_{agg} , normalized by t_0 , against N for $D_f = 3$ deterministically generated spherical agglomerates. Solid lines denote the theoretical results for $k_f = 1.1$ (red), $k_f = 0.57$ (blue) and $k_f = 0.22$ (black); symbols denote the simulation data for body centered cubic (circles) and simple cubic (squares), with different k_f indicated by the corresponding colors.

Fig. 5.6 shows t_{agg}/t_0 obtained from numerical simulations with non-fractal agglomerates ($D_f = 3.0$), as a function of N . Our theoretical model, using the theoretically derived $\alpha = \sqrt{\frac{5}{3}}$, accurately predicts the simulation results, including changes in scaling

behavior from small to large N . For $D_f < 3$, no theoretical value for α is available, but we find good agreement between the theoretical model and numerical simulations with random agglomerates when using $\alpha = 1.47$ for all cases, as shown in Fig. 5.7. For DLA agglomerates, when using $\alpha = 1.47$, we found that, although the predictions are not exact, the theoretical results successfully capture the scaling law in t_{agg} against N , as shown in Fig. 5.8.

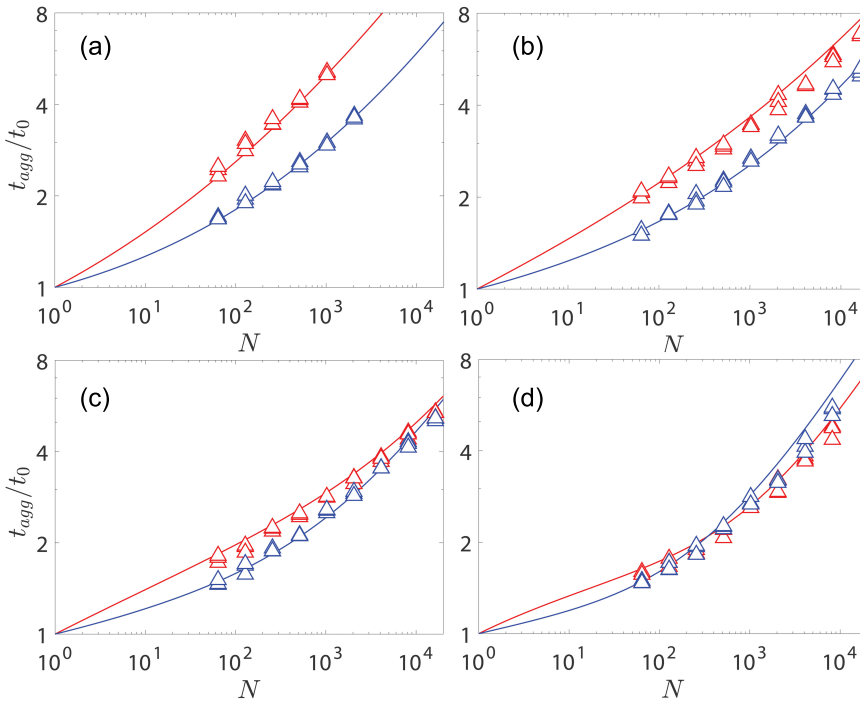


Figure 5.7: Agglomerate saturation time t_{agg} , normalized by t_0 , against N for random agglomerates with $D_f = 2.7$ (a), $D_f = 2.5$ (b), $D_f = 2.3$ (c) and $D_f = 2.0$ (d). Red lines (theoretical results) and symbols (simulation data) denote $k_f = 1.1$; blue lines and symbols denote $k_f = 0.57$. For each combination of N , k_f and D_f , three different realizations of the agglomerates are simulated, as indicated in the plots.

5.4. CONCLUSION

In summary, we have presented a closed form theory, validated against molecular simulations, showing the scaling of the moving reaction front penetration time inside nanoporous solids, due to the interplay between Knudsen diffusion and self-limiting gas-surface reactions. Complementary to classical theory [11] on non self-limiting reactions in porous materials, the theory presented in this paper importantly increases our understanding of gas diffusion with reaction processes inside porous materials. We focused on agglomerates of mono-sized nanoparticles as an important class of nanoporous materials, and

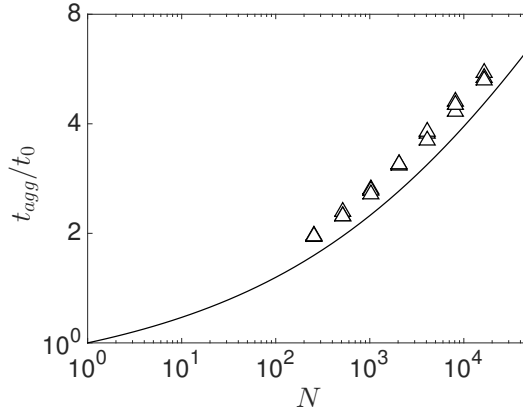


Figure 5.8: Agglomerate saturation time t_{agg} , normalized by t_0 , against N for DLA agglomerates with $k_f = 0.37$ and $D_f = 2.5$. The solid line denotes the theoretical result and symbols denote simulation results. For each N , three different realizations of the agglomerates are simulated, as indicated in the plots.

have shown that in such materials the penetration time is governed by four different time scales each with its own scaling behaviour. The dominating time scale is dictated by both the size and the fractal dimension of the agglomerate. For the large agglomerate sizes frequently encountered in practice, the penetration time scales with the number of particles N in the agglomerate as $N^{\frac{D_f-1}{D_f}}$. The penetration time for agglomerates with fractal dimensions $D_f < 3$, in which the surface-to-volume ratio decreases (the average void fraction increases) with distance from the center of mass, thus may be orders of magnitude smaller than for simple, i.e. constant void fraction, materials. Such a varying void fraction fractal structure may be the result of natural processes in agglomeration [22], but may also be purposely manufactured [37], and here our model allows for optimal structure design. We believe that the presented approach may readily be extended to other classes of nanoporous materials. This requires adaptation of our expressions for the surface-to-volume ratio and the mean molecular travel distance in the porous material. We have found indications that our model also holds for diffuse reaction fronts due to smaller-than-one reaction probabilities, but this requires further study, as does the extension of our model to situations in which the relevant length scale is not large compared to the mean free path, such as in high pressure processes and in macroporous materials.

REFERENCES

- [1] M. Milina, S. Mitchell, P. Crivelli, D. Cooke, and J. Pérez-Ramírez, *Mesopore quality determines the lifetime of hierarchically structured zeolite catalysts*, *Nature Communications* (2014), 10.1038/ncomms4922.
- [2] P. Canepa, N. Nijem, Y. J. Chabal, and T. Thonhauser, *Diffusion of Small Molecules in Metal Organic Framework Materials*, *Phys. Rev. Lett.* **110**, 026102+ (2013), arXiv:1212.1935.
- [3] S. M. George, *Atomic Layer Deposition: An Overview*, *Chemical Reviews*, *Chem. Rev.* **110**, 111 (2010).
- [4] D. M. King, X. Liang, and A. W. Weimer, *Functionalization of fine particles using atomic and molecular layer deposition*, *Powder Technology* **221**, 13 (2012).
- [5] H. Van Bui, F. Grillo, and J. R. van Ommen, *Atomic and molecular layer deposition: off the beaten track*, *Chem. Commun.* **53**, 45 (2017).
- [6] M. Knudsen, *Die Gesetze der Molekularströmung und der inneren Reibungsströmung der Gase durch Röhren*, *Ann. Phys.* **333**, 75 (1909).
- [7] J. Kärger and D. M. Ruthven, *Diffusion in zeolites and other microporous solids* (Wiley, 1992).
- [8] K. Malek and M. O. Coppens, *Effects of surface roughness on self- and transport diffusion in porous media in the Knudsen regime*. *Physical review letters* **87**, 125505+ (2001).
- [9] R. Aris, *The Mathematical Theory of Diffusion and Reaction in Permeable Catalysts: Vol. 1: The Theory of the Steady State (Oxford Studies in Physics) (v. 1)* (Oxford University Press, 1975).
- [10] D. M. Ackerman, J. Wang, and J. W. Evans, *Generalized Hydrodynamic Treatment of the Interplay between Restricted Transport and Catalytic Reactions in Nanoporous Materials*, *Phys. Rev. Lett.* **108**, 228301+ (2012).
- [11] E. W. Thiele, *Relation between Catalytic Activity and Size of Particle*, *Ind. Eng. Chem.* **31**, 916 (1939).
- [12] H. Sato, W. Kosaka, R. Matsuda, A. Hori, Y. Hijikata, R. V. Belosludov, S. Sakaki, M. Takata, and S. Kitagawa, *Self-Accelerating CO Sorption in a Soft Nanoporous Crystal*, *Science* **343**, 167 (2014).
- [13] H. W. Kim, H. W. Yoon, S.-M. Yoon, B. M. Yoo, B. K. Ahn, Y. H. Cho, H. J. Shin, H. Yang, U. Paik, S. Kwon, J.-Y. Choi, and H. B. Park, *Selective Gas Transport Through Few-Layered Graphene and Graphene Oxide Membranes*, *Science* **342**, 91 (2013).

- [14] R. G. Gordon, D. Hausmann, E. Kim, and J. Shepard, *A Kinetic Model for Step Coverage by Atomic Layer Deposition in Narrow Holes or Trenches*, *Chemical Vapor Deposition* **9**, 73 (2003).
- [15] H. C. M. Knoop, E. Langereis, M. C. M. van de Sanden, and W. M. M. Kessels, *Conformality of Plasma-Assisted ALD: Physical Processes and Modeling*, *Journal of The Electrochemical Society* **157**, G241 (2010).
- [16] J. Dendooven, D. Deduytsche, J. Musschoot, R. L. Vanmeirhaeghe, and C. Detavernier, *Modeling the Conformality of Atomic Layer Deposition: The Effect of Sticking Probability*, *Journal of The Electrochemical Society* **156**, P63 (2009).
- [17] A. M. Lankhorst, B. D. Paarhuis, H. J. C. M. Terhorst, P. J. P. M. Simons, and C. R. Kleijn, *Transient ALD simulations for a multi-wafer reactor with trenched wafers*, *Surface and Coatings Technology* **201**, 8842 (2007).
- [18] C. Detavernier, J. Dendooven, S. Pulinthanathu Sree, K. F. Ludwig, and J. A. Martens, *Tailoring nanoporous materials by atomic layer deposition*, *Chemical Society Reviews* **40**, 5242+ (2011).
- [19] M.-O. Coppens and G. F. Froment, *Diffusion and reaction in a fractal catalyst pore—I. Geometrical aspects*, *Chemical Engineering Science* **50**, 1013 (1995).
- [20] W. Yao, G. Guangsheng, W. Fei, and W. Jun, *Fluidization and agglomerate structure of SiO₂ nanoparticles*, *Powder Technology* **124**, 152 (2002).
- [21] T. Schwager, D. E. Wolf, and T. Pöschel, *Fractal Substructure of a Nanopowder*, *Phys. Rev. Lett.* **100**, 218002+ (2008).
- [22] L. de Martín, A. Fabre, and J. R. van Ommen, *The fractal scaling of fluidized nanoparticle agglomerates*, *Chemical Engineering Science* **112**, 79 (2014).
- [23] P. Clausing, *The Flow of Highly Rarefied Gases through Tubes of Arbitrary Length*, *Journal of Vacuum Science and Technology* **8**, 636 (1971).
- [24] B. Derjaguin, *measurement of the specific surface of porous and disperse bodies by their resistance to the flow of rarefied gas*, *C. R. Acad. Sci. URSS* **53**, 623+ (1946).
- [25] A. Berson, H. W. Choi, and J. G. Pharoah, *Determination of the effective gas diffusivity of a porous composite medium from the three-dimensional reconstruction of its microstructure*, *Physical Review E* **83**, 026310+ (2011).
- [26] A. Pavlovitch, R. Jullien, and P. Meakin, *Geometrical properties of a random packing of hard spheres*, *Physica A: Statistical Mechanics and its Applications* **176**, 206 (1991).
- [27] B. Lu and S. Torquato, *Chord length and free path distribution functions for many body systems*, *The Journal of Chemical Physics* **98**, 6472 (1993).

- [28] J. M. Zalc, S. C. Reyes, and E. Iglesia, *The effects of diffusion mechanism and void structure on transport rates and tortuosity factors in complex porous structures*, Chemical Engineering Science **59**, 2947 (2004).
- [29] O. Levenspiel, *Chemical reaction engineering [Hauptbd.]. [Hauptbd.]*. (Wiley, 1999).
- [30] A. V. Filippov, M. Zurita, and D. E. Rosner, *Fractal-like Aggregates: Relation between Morphology and Physical Properties*, Journal of Colloid and Interface Science **229**, 261 (2000).
- [31] van Ommen, J. Valverde, and R. Pfeffer, *Fluidization of nanopowders: a review*, Journal of Nanoparticle Research **14**, 1 (2012).
- [32] K. Skorupski, J. Mroczka, T. Wriedt, and N. Riefler, *A fast and accurate implementation of tunable algorithms used for generation of fractal-like aggregate models*, Physica A: Statistical Mechanics and its Applications **404**, 106 (2014).
- [33] T. A. Witten and L. M. Sander, *Diffusion-Limited Aggregation, a Kinetic Critical Phenomenon*, Physical Review Letters **47**, 1400 (1981).
- [34] K. R. Kuijpers, L. de Martín, and J. R. van Ommen, *Optimizing off-lattice Diffusion-Limited Aggregation*, Computer Physics Communications **185**, 841 (2014).
- [35] G. A. Bird, *Recent advances and current challenges for DSMC*, Computers & Mathematics with Applications **35**, 1 (1998).
- [36] T. J. Scanlon, E. Roohi, C. White, M. Darbandi, and J. M. Reese, *An open source, parallel DSMC code for rarefied gas flows in arbitrary geometries*, Computers & Fluids **39**, 2078 (2010).
- [37] G. Wang, E. Johannessen, C. R. Kleijn, S. W. de Leeuw, and M.-O. Coppens, *Optimizing transport in nanostructured catalysts: A computational study*, Chemical Engineering Science **62**, 5110 (2007).



APPENDIX

5.A. SIMPLIFICATION OF EXPRESSIONS FOR t_F AND t_M

For large agglomerates with $R \gg a$, $D_f < 3$ and $k_f^{-1} \alpha^{D_f} a^{D_f-2} R^{3-D_f} \gg a$, i.e.

$$N^{\frac{3-D_f}{D_f}} \gg k_f^{\frac{3}{D_f}} \alpha^{-3} \quad (S1)$$

we neglect T_F as well as the $\frac{1}{3}a$ and a terms in the denominators in Eq. (5), which is thus simplified to

$$t_F = \frac{\rho_{site}}{F_0} \int_a^R k_f D_f \alpha^{-D_f} a^{2-D_f} r^{D_f-3} \left[1 + \frac{13}{48} k_f \alpha^{-D_f} a^{2-D_f} (R^{D_f-2} - R^{D_f-3} r) \right] dr \quad (S2)$$

When $D_f > 2$, Eq. (S2) has an analytical solution as,

$$\begin{aligned} t_F &= \frac{\rho_{site}}{F_0} \left[\frac{k_f D_f \alpha^{-D_f} a^{2-D_f}}{D_f - 2} r^{D_f-2} + \frac{13}{48} \frac{k_f^2 D_f \alpha^{-2D_f} a^{4-2D_f}}{(D_f - 1)(D_f - 2)} R^{D_f-3} (R \cdot r^{D_f-2} - r^{D_f-1}) \right] \Big|_a^R \\ &\approx \frac{\rho_{site}}{F_0} \left[\frac{k_f D_f \alpha^{-D_f} a^{2-D_f}}{D_f - 2} r^{D_f-2} + \frac{13}{48} \frac{k_f^2 D_f \alpha^{-2D_f} a^{4-2D_f}}{(D_f - 1)(D_f - 2)} R^{D_f-3} (R \cdot r^{D_f-2} - r^{D_f-1}) \right] \Big|_0^R \\ &= \frac{\rho_{site}}{F_0} \left(\frac{k_f D_f \alpha^{-D_f} a^{2-D_f}}{D_f - 2} R^{D_f-2} + \frac{13}{48} \frac{k_f^2 D_f \alpha^{-2D_f} a^{4-2D_f}}{(D_f - 1)(D_f - 2)} R^{2D_f-4} \right) \quad (S3) \end{aligned}$$

By substituting R with N using Eq. (1), Eq. (S5.17) can be written as,

$$t_F = k_1 N^{\frac{D_f-2}{D_f}} + k_2 N^{\frac{2D_f-4}{D_f}} \quad (6)$$

with constants $k_1 = \frac{\rho_{site}}{F_0} k_f^{\frac{2}{D_f}} \frac{D_f}{D_f-2} \alpha^{-2}$ and $k_2 = \frac{13}{48} \frac{\rho_{site}}{F_0} k_f^{\frac{4}{D_f}} \frac{D_f}{(D_f-2)(D_f-1)} \alpha^{-4}$.

From Eq. (7), using

$$D_k = \frac{12a(1-\phi_s)u_t}{13\phi_s} \quad (S4)$$

and

$$\phi_s = k_f \alpha^{-D_f} a^{3-D_f} R^{D_f-3} \quad (S5)$$

we obtain,

$$t_M = \frac{R-a}{u_t} + \frac{13}{72} \frac{(R-a)^2}{\left(\frac{\alpha^{D_f} a^{D_f-2}}{k_f} R^{3-D_f} - a\right) u_t} + T_M \quad (S6)$$

Again, for large agglomerates with $R \gg a$, $2 < D_f < 3$ and $k_f^{-1} \alpha^{D_f} a^{D_f-2} R^{3-D_f} \gg a$, i.e.

$$N^{\frac{3-D_f}{D_f}} \gg k_f^{\frac{3}{D_f}} \alpha^{-3} \quad (S7)$$

we neglect T_M and thus obtain,

$$t_M = \frac{1}{u_t} R + \frac{13}{72} k_f \alpha^{-D_f} a^{2-D_f} \frac{1}{u_t} R^{D_f-1} \quad (S8)$$

By substituting R with N using Eq. (1), Eq. (S8) can be written as,

$$t_M = k_3 N^{\frac{1}{D_f}} + k_4 N^{\frac{D_f-1}{D_f}} \quad (8)$$

with $k_3 = k_f^{-\frac{1}{D_f}} \alpha \frac{a}{u_t}$ and $k_4 = \frac{13}{72} k_f^{\frac{1}{D_f}} \alpha^{-1} \frac{a}{u_t}$.

5.B. INFLUENCE OF THE RELAXATION OF THE PARTICLE ATTACHMENT CRITERIA

We have generated additional sets of agglomerates for $k_f = 1.1$ and $D_f = 2.5$, imposing an additional constraint that each particles touches at least one other particle. In order to investigate the influence of this additional constraint on the total reaction time t_{agg} , we have conducted the same simulations on these agglomerates. Fig. 5.B.1 shows the results in comparison to those of agglomerates generated without this additional constraint. We conclude that this constraint has negligible influence on t_{agg} for nanoparticle agglomerates.

5.C. INFLUENCE OF THE STICKING COEFFICIENT

Our model describes the progression of a sharp saturation front, as it will occur for a high sticking coefficient $\gamma \rightarrow 1$. For lower γ , the transition between saturated and unsaturated

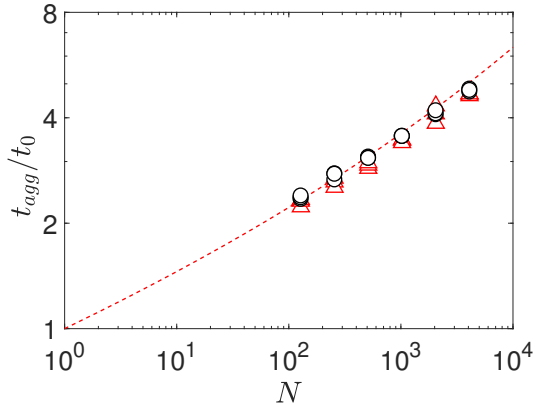


Figure 5.B.1: Total reaction time t_{agg} , normalized by t_0 , against N for $k_f = 1.1$ and $D_f = 2.5$ agglomerates generated with (red triangles) and without (black circles) the constraint that each particle in the agglomerate should touch at least one other agglomerate. The dashed line denotes the results from our theoretical model. For each N , three different realizations of the agglomerates are simulated, as indicated in the plot.

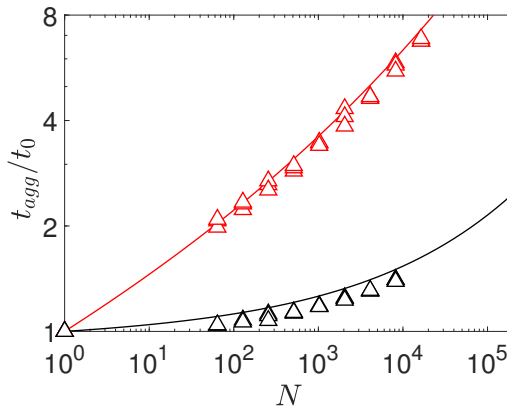


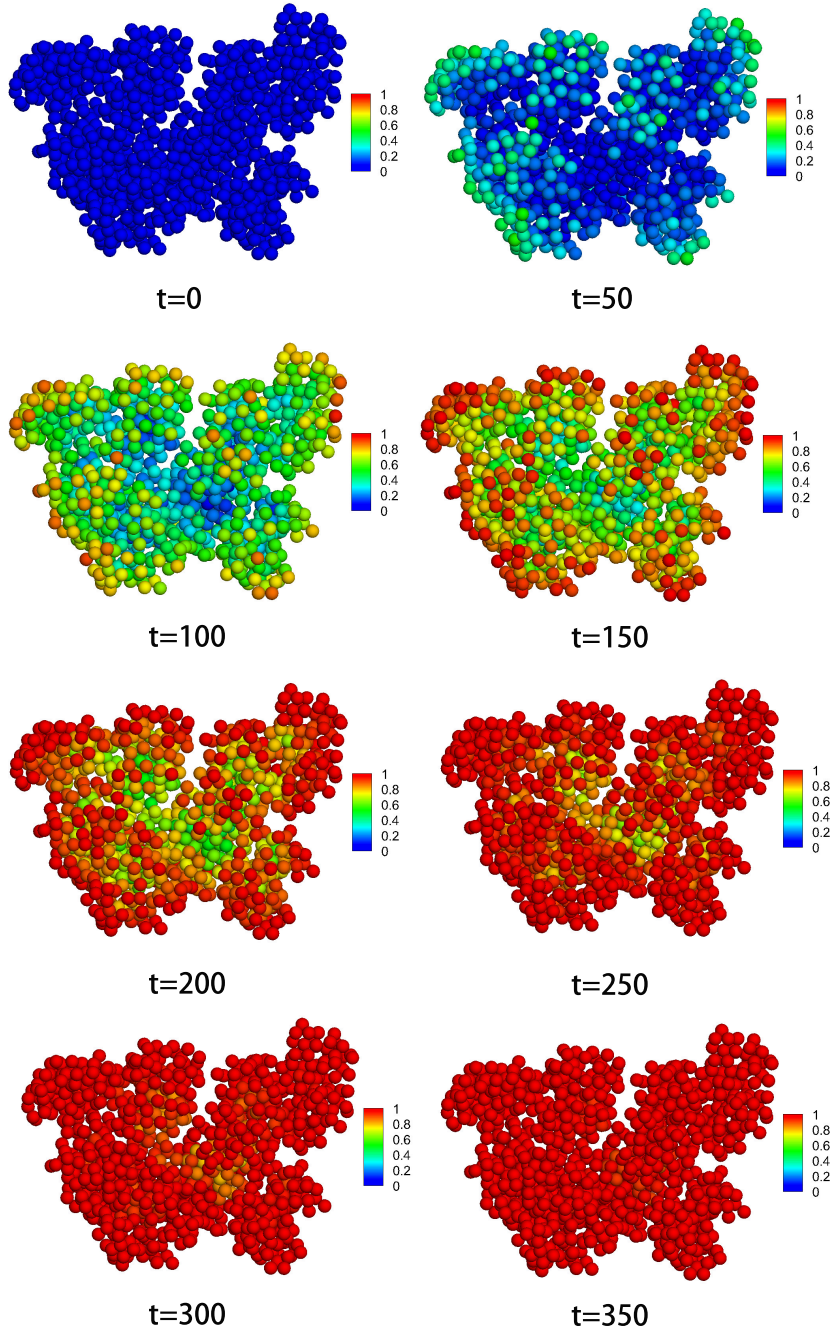
Figure 5.C.1: Total reaction time t_{agg} , normalized by t_0 , against N for agglomerates with $k_f = 1.1$, $D_f = 2.5$, for $\gamma = 0.1$ (black triangles) and $\gamma = 1$ (red triangles). The lines (red for $\gamma = 1$ and black for $\gamma = 0.1$) denote results from our theoretical model. For each N , three different realizations of the agglomerates are simulated, as indicated in the plot.

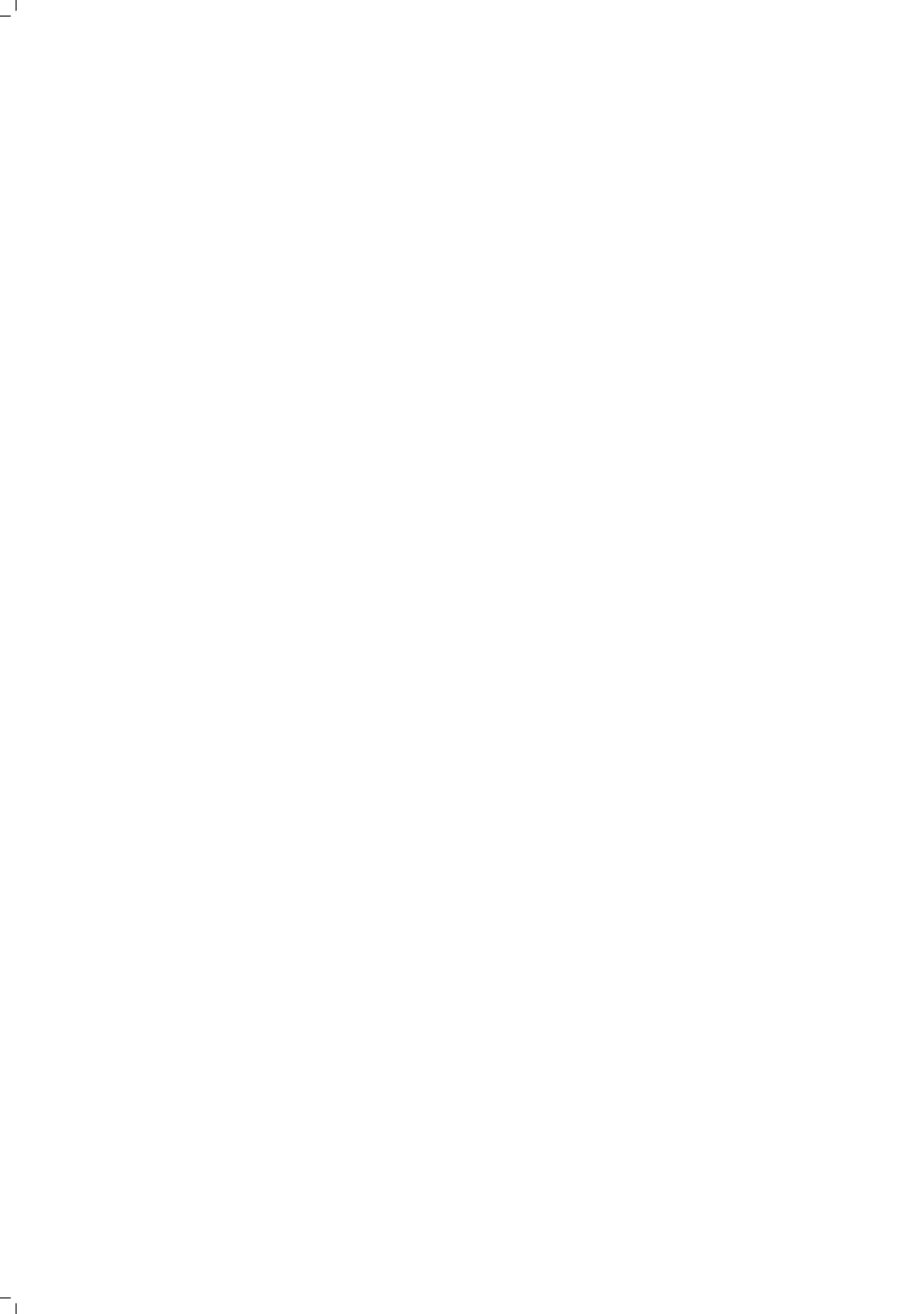
areas will become less steep [16]. Here we investigate the influence of $\gamma < 1$ on the validity of our model and on the total coating time t_{agg} . In order to do so, we conducted simulations with $\gamma = 0.1$ for agglomerates with $k_f = 1.1$ and $D_f = 2.5$, and compared to the results for $\gamma = 1$ as shown in Fig. 5.C.1. t_{agg} for $\gamma = 0.1$ are, on average, slightly overpredicted by our model, however, the differences are rather small. We conclude that our theoretical model still holds, at least qualitatively, for non-sharp reaction fronts as

obtained for $0.1 \leq \gamma < 1$.

5.D. EVOLUTION OF SURFACE COVERAGE IN TIME

Figure 5.D.1 shows the evolution of the surface coverage per particle in time.

Figure 5.D.1: A series of snapshots showing the evolution of the surface coverage in time (normalized with Δt).



6

CONCLUSIONS AND OUTLOOK

6.1. CONCLUSIONS

Agglomeration is an essential feature of nanoparticle fluidization. The complex morphology of the agglomerates introduces new challenges in understanding ALD coating processes of fluidized nanoparticles. This thesis presents new insights on this problem through numerical simulations as well as theoretical modeling based on the fractal characteristics of the agglomerates. Our main finding is how the ALD coating time scales with the size and fractal dimension of the agglomerate.

We first developed and implemented a new cut-cell method in conjunction with Direct Simulation Monte Carlo of rarefied gas flows (in Chapter 3). This is the foundation of the subsequent studies in this thesis, as it allows simulating rarefied gas flows with physical and chemical interactions with arbitrarily shaped immersed moving objects. More specifically, this cut-cell algorithm utilizes analytically expressed 3D immersed bodies, and thus accounts accurately for bounce back of the incident molecules. The cut cell effective volume is computed by representing the immersed boundary with the Lagrangian intersecting points and thus reconstructing all the possible polyhedra and taking the mean average. It has been shown that for arbitrary immersed body, the relative error in the computed overlap volume decreases linearly with the grid refinement. This new cut-cell method has been validated by computing the drag force on a (moving) sphere; the results agree very well with analytical solutions found in literature.

6

Using this new cut-cell method, we have simulated atomic layer deposition on fractal nanoparticle agglomerates with fractal dimension $2 < D_f < 3$ (in Chapter 4). In our simulations, we combine a self-limiting ALD half cycle reaction and gas diffusion in the gas rarefied regime, together with a fully resolved fractal agglomerate of spherical nanoparticles. We find that the overall coating time of an agglomerate, normalized by that of a single particle, increases for increasing pressure, i.e., decreasing gas mean free path λ , up to $\lambda \sim 10a$, whereas it becomes independent of the pressure for $\lambda > 10a$, with a the nanoparticle radius. This indicates that a is the proper length scale for calculating the Knudsen number for this particular problem. For pressures below 0.1 bar, diffusion in the simulated agglomerates is well in the free molecular regime, and further reduction of the pressure has little influence on the normalized coating time.

In Chapter 4, we also made our first attempt to develop a theoretical model by deriving a generalized form of the Gordon model [1], which was originally proposed for ALD coating within a simple cylindrical hole or trench. Our generalized Gordon model predicts the ALD coating time within fractal agglomerates, with two model constants k_1 and k_2 derived from the analogy between a narrow hole and a fractal agglomerate. According to our model, the overall coating time increases for increasing fractal dimension D_f , in good agreement with our simulation results for $D_f \geq 2.3$, while some deviations are observed for $D_f < 2.3$.

Based on our generalized Gordon model, we took a step further to develop a closed

form theory (in Chapter 5), showing the scaling of the coating time with agglomerate size, due to the interplay between Knudsen diffusion and self-limiting gas-surface reactions. Complementary to classical theory [2] on non self-limiting reactions in porous materials, the theory presented in this chapter importantly increases our understanding of gas diffusion with self-limiting reaction processes inside porous materials. We identified four main time scales that contribute to the overall coating time, and came up with a regime map that shows the dominating time scales for different combinations of number of particles N and D_f . For the large agglomerate sizes frequently encountered in practice, the coating time scales with N in the agglomerate as $N^{\frac{D_f-1}{D_f}}$. Thus, coating times for large fractal ($D_f < 3$) agglomerates may be orders of magnitudes smaller than for non-fractal ($D_f = 3$) agglomerates. The model predictions have been validated with our simulation results, and we have found good agreement for all the studied cases.

We believe that the presented theory may readily be extended to other classes of nanoporous materials. This requires adaptation of our expressions for the surface-to-volume ratio and the mean molecular travel distance in the porous material. We have found indications that our model also holds for diffuse reaction fronts as occurring for smaller-than-one reaction probabilities. This, however, requires further study, as does the extension of our model to situations in which the relevant length scale is not large compared to the mean free path, such as in high pressure processes and in macroporous materials.

6.2. OPPORTUNITIES FOR FUTURE RESEARCH

6.2.1. FIRST ORDER REACTION ON FRACTALS IN RAREFIED GAS REGIME

Throughout this thesis, we have discussed self-limiting surface reactions on fractal agglomerates. However, when we remove the self-limiting nature, the studied problem turns into the classic reaction-diffusion problem with its complexity arising from the fractal morphology. In this case, the steady state overall reaction rate ψ , defined as the total number of molecules that react on the agglomerate in a unit time, becomes the key property of the system. This ψ depends on the interplay between the gas phase transport and the surface consumption.

In the continuum flow regime, the gas transport is purely diffusive regardless of the problem length scale. In this regime, several researches in literature [3–6] have studied the scaling behavior of ψ as a function of the agglomerate size R_g , its fractal dimension D_f , and the gas molecule sticking coefficient γ . According to these studies, ψ scales differently in the reaction-limited and diffusion-limited regime:

$$\psi \sim \gamma R_g^{D_f}, \text{ reaction limited regime} \quad (6.1)$$

$$\psi \sim \gamma^{\frac{1}{D_f-1}} R_g^2, \text{ diffusion limited regime} \quad (6.2)$$

In the free molecular regime (the gas phase transport is fully ballistic), the scaling of ψ has been theoretically studied as a function of R_g and D_f , for $\gamma = 1$, leading to [7, 8]

$$\psi \sim R_g^2, \text{ for } D_f \geq 2 \quad (6.3)$$

and

$$\psi \sim R_g^{D_f}, \text{ for } D_f < 2 \quad (6.4)$$

However, a detailed and systematic study on the scaling of ψ in the gas rarefaction transition regime is still missing in literature, despite of its importance in bridging the continuum and free molecular regimes. Filling in this gap could be of great interest for applications such as nanoparticle catalysis. DSMC could be an excellent candidate for studying this problem, and the numerical methods developed in this thesis are suitable for simulating surface reactions on immersed fractal agglomerates as shown in Chapter 4 and 5. The well developed theories in the continuum flow regime [Eqs. (6.1) and (6.2)] could be a good starting point. Thus one could perform DSMC simulations with first order surface reactions on fractal nanoparticles and observe how ψ deviates from the continuum case as a function of Knudsen number which could be varied by changing the pressure of the gas.

6.2.2. AGGLOMERATE MOVEMENT IN A GAS FLOW

In this thesis we have focused on agglomerates that are static during the simulation time. However, in a fluidized bed the agglomerates keep moving around and collide with each other. In fact, even the movement of a single agglomerate in the gas flow is not fully understood in literature. The key to the study of the agglomerate movement is the drag force exerted on the agglomerate.

The most commonly used technique that measures the drag on agglomerates is the differential mobility analyzer [9]. In this technique, agglomerates with one elementary electrical charge are brought, along with the carrier gas, into a channel with an electrical field which is perpendicular to the gas velocity. Therefore, agglomerates with one specific drag force (mobility) can exit through a slit at the corresponding location in the channel. In this measurement, it is assumed that different orientations of the agglomerate are equally possible during the movement, and thus the measured drag is regarded as the orientationally averaged drag.

Recently, Zhang et al. [10] reported that the orientationally averaged drag force on an agglomerate in the transition regime can be computed with the same formula as that for a spherical sphere. The drag force exerted on a single sphere at low Reynolds number in

the continuum regime is expressed by the Stokes' law as

$$F_{cont} = 6\pi\mu au, \quad (6.5)$$

where a is the radius of the sphere, μ is fluid viscosity and u is the relative velocity between the fluid and sphere. For a sphere in a transition regime gas flow, the drag can be expressed as

$$F = \frac{6\pi\mu au}{C_c(Kn)}, \quad (6.6)$$

where $C_c(Kn)$ is the Cunningham correction factor which is a function of Knudsen number.

Zhang et al. proposed the length scale $l = \frac{A_p}{\pi R_s}$ for computing Kn for an agglomerate, where A_p is the orientationally averaged projected area of the agglomerate and R_s is the Smoluchowski radius [11]. With this newly defined Knudsen number, it was shown that drag forces of all arbitrarily shaped agglomerates follow Eq. (6.6) for varying Knudsen number.

Note that in all of the above discussions only the orientationally averaged drag was considered for the agglomerates. However, Binder [12] has proven with experiments that a descending agglomerate in oil has a strong preference in its orientation which minimizes the drag force. Whether this is also the case for an agglomerate in a (rarefied) gas flow still remains as a question. In general, the random kicks from the surrounding gas molecules on an agglomerate result in two kinds of effects: (1) they act as random driving force, which results in the Brownian motion of the agglomerate, and (2) they act as friction force that damps out the velocity difference between the mean flow and the agglomerate, and rotation of the agglomerate. The Brownian motion leads to arbitrary orientation of the agglomerate, whereas the drag force sets a preferred orientation. Simulations can help gain new insights on this problem. One can simulate a relatively small ($\sim O(10^3 - 10^4)$ particles) agglomerate (as found in the fluidization of micron-sized particles [13]), immersed in a gas flow and driven by an external body force, much alike our validation case with a moving sphere shown in Chapter 3. During the simulations the orientation of the agglomerate can be monitored, and one can perform parameter studies with different agglomerates. An interesting question to be answered here is: do fractal agglomerates have preferred orientation during the movement?

6.2.3. DYNAMIC AGGLOMERATION

In a fluidized bed, the agglomerates undergo a dynamic process of breakdown and re-agglomeration, which is not taken into account in this thesis. In order to study this phenomenon, we need to remove the previously assumed permanent bonds between particles or clusters of particles, and replace them with correct inter-particle forces. There have been continuous efforts in literature for measuring and modeling the inter-particle

forces [14–17]. This section will discuss the possible simulations of agglomeration dynamics.

The simulation of nanoparticle agglomeration can follow the molecular dynamics (MD) scheme. In this system a nanoparticle experiences three different forces, i.e. gravitational force, inter-particle force and the aerodynamic force. At each time step, the inter-particle force can be computed from the relative positions of the particles, and the aerodynamic force can be calculated from the momentum exchange with the bounced gas molecules. Thus, a total force F_i can be computed for the i th particle and, by following the Newton's second law, an incremental change is made to the particle velocity as

$$u_{i,t+\Delta t} = u_{i,t} + \frac{F_i}{m} \Delta t \quad (6.7)$$

Note that here the inclusion of a repulsive inter-particle force at short distance is necessary in order to avoid overlapping between particles. One can start the simulation with many nanoparticles randomly distributed in a periodic box. Then with an upward mean flow velocity, one can mimic the scenario inside the fluidized bed and thus dynamic agglomeration behavior is expected. By monitoring the life time of the agglomerates and analyzing the breakup scenarios, an important question to be answered here is: what is the main mechanism behind the breakup and formation of the dynamic agglomerates?

6

6.2.4. POLYDISPERSE NANOPARTICLES

Throughout this thesis we have focused on monodisperse nanoparticles, whereas in reality nanoparticles are more likely to be polydisperse following a certain distribution. In this section we will discuss the influence of polydispersity on our numerical and theoretical models.

In the numerical simulations, the inclusion of polydisperse nanoparticles is rather straightforward. When generating numerical agglomerates using the tunable algorithm, the fixed particle radius should be replaced with one that is randomly drawn from the distribution function, and the calculation of the rotation angles (described in Chapter 2) should be altered according to the distance based on the two attaching particles. Skorpinski et al. [18] have demonstrated numerically generated polydisperse agglomerates, as shown in Fig 6.1. The inclusion of the polydisperse nanoparticles in DSMC is identical to that of monodisperse nanoparticles, except that now we need to provide the radius for each particle.

A straightforward way to modify the theoretical model in Chapter 5 to account for polydispersity is to simply replace the particle diameter, surface area and volume a , a^2 and a^3 , by their respective average values $\langle a \rangle$, $\langle a^2 \rangle$ and $\langle a^3 \rangle$. Numerical simulations can be used to examine the validity of such simple modifications.

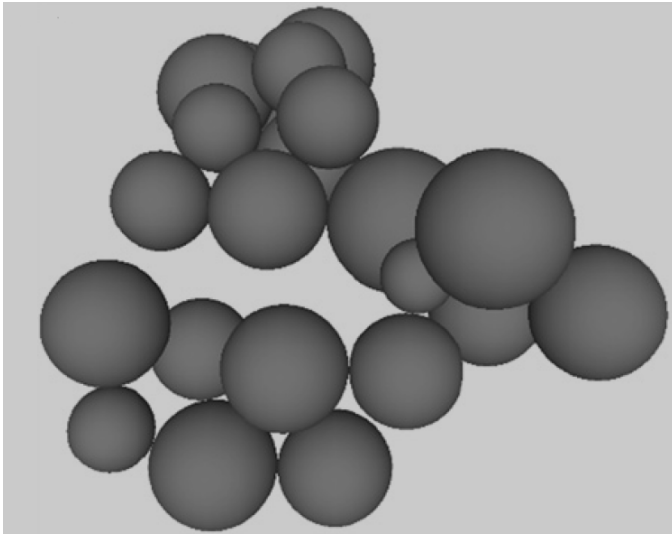


Figure 6.1: An agglomerate generated with disperse particles, with $N = 25$, $k_f = 1.5$ and $D_f = 2.0$. [18]

REFERENCES

- [1] R. G. Gordon, D. Hausmann, E. Kim, and J. Shepard, *A Kinetic Model for Step Coverage by Atomic Layer Deposition in Narrow Holes or Trenches*, *Chemical Vapor Deposition* **9**, 73 (2003).
- [2] E. W. Thiele, *Relation between Catalytic Activity and Size of Particle*, *Ind. Eng. Chem.* **31**, 916 (1939).
- [3] E. Chassaing and B. Sapoval, *Electrochemical Impedance of Blocking Quasi Fractal 3d Electrodes*, *Journal of The Electrochemical Society* **141**, 2711 (1994).
- [4] P. Meakin and B. Sapoval, *Random-walk simulation of the response of irregular or fractal interfaces and membranes*, *Physical Review A* **43**, 2993 (1991).
- [5] D. S. Grebenkov, *Scaling properties of the spreadharmonic measures*, *Fractals* **14**, 231 (2006).
- [6] D. S. Grebenkov, M. Filoche, and B. Sapoval, *A simplified analytical model for laplacian transfer across deterministicprefractal interfaces*, **15**, 27 (2007).
- [7] A. Coniglio and H. E. Stanley, *Screening of Deeply Invaginated Clusters and the Critical Behavior of the Random Superconducting Network*, *Physical Review Letters* **52**, 1068 (1984).

- [8] A. Schmidt-Ott, U. Baltensperger, H. W. G?ggeler, and D. T. Jost, *Scaling behaviour of physical parameters describing agglomerates*, *Journal of Aerosol Science* **21**, 711 (1990).
- [9] K. Cho, C. Hogan, and P. Biswas, *Study of the mobility, surface area, and sintering behavior of agglomerates in the transition regime by tandem differential mobility analysis*, *Journal of Nanoparticle Research*, **9**, 1003 (2007).
- [10] C. Zhang, T. Thajudeen, C. Larriba, T. E. Schwartzentruber, and C. J. Hogan, *Determination of the Scalar Friction Factor for Nonspherical Particles and Aggregates Across the Entire Knudsen Number Range by Direct Simulation Monte Carlo (DSMC)*, *Aerosol Science and Technology* **46**, 1065 (2012).
- [11] R. Gopalakrishnan, T. Thajudeen, and Jr, *Collision limited reaction rates for arbitrarily shaped particles across the entire diffusive Knudsen number range*, *The Journal of Chemical Physics* **135**, 054302+ (2011).
- [12] C. Binder, M. A. J. Hartig, and W. Peukert, *Structural dependent drag force and orientation prediction for small fractal aggregates*, *Journal of Colloid and Interface Science* **331**, 243 (2009).
- [13] J. M. Valverde, M. A. S. Quintanilla, A. Castellanos, D. Lepek, J. Quevedo, R. N. Dave, and R. Pfeffer, *Fluidization of fine and ultrafine particles using nitrogen and neon as fluidizing gases*, *AIChE J.* **54**, 86 (2008).
- [14] A. Fabre, S. Salameh, L. Ciacchi, M. Kreutzer, and van Ommen, *Contact mechanics of highly porous oxide nanoparticle agglomerates*, *Journal of Nanoparticle Research*, **18**, 1 (2016).
- [15] J. Laube, S. Salameh, M. Kappl, L. M?dler, and L. Colombi Ciacchi, *Contact Forces between TiO₂ Nanoparticles Governed by an Interplay of Adsorbed Water Layers and Roughness*, *Langmuir* **31**, 11288 (2015).
- [16] J. P. Pantina and E. M. Furst, *Elasticity and critical bending moment of model colloidal aggregates*. *Physical review letters* **94** (2005).
- [17] V. Becker and H. Briesen, *Tangential-force model for interactions between bonded colloidal particles*, *Physical Review E* **78** (2008), 10.1103/physreve.78.061404, arXiv:0808.3108 .
- [18] K. Skorupski, J. Mroczka, T. Wriedt, and N. Riefler, *A fast and accurate implementation of tunable algorithms used for generation of fractal-like aggregate models*, *Physica A: Statistical Mechanics and its Applications* **404**, 106 (2014).

LIST OF PUBLICATIONS

4. **W. Jin**, J. R. van Ommen, C. R. Kleijn, *Moving Reaction Fronts in Fractal Nanoparticle Agglomerates*, Physical Review E (under review).
3. **W. Jin**, C. R. Kleijn, J. R. van Ommen, *Simulation of atomic layer deposition on nanoparticle agglomerates*, Journal of Vacuum Science and Technology A **35**, 01B116 (2017).
2. **W. Jin**, J. R. van Ommen, C. R. Kleijn, *A new cut-cell algorithm for DSMC simulations of rarefied gas flows around immersed moving objects*, Computer Physics Communications **212**, 146-151 (2017).
1. **W. Jin**, J. R. van Ommen, C. R. Kleijn, *Direct simulation Monte Carlo calculation of rarefied gas drag using an immersed boundary method*, INTERNATIONAL CONFERENCE OF NUMERICAL ANALYSIS AND APPLIED MATHEMATICS (2015).



ACKNOWLEDGEMENTS

I still remember my interview day at TU Delft, got lost in the campus while Ruud was looking for me on a bike. It feels like yesterday, while this journey has come to an end. This four years of PhD has been such an unforgettable experience in my life, not only for the academic achievements, but also for the many people who have been the important and essential part of this journey and made my life in Delft so wonderful.

First of all, I would like to thank my promotor Chris Kleijn, and my co-promotor Ruud van Ommen. There was a time when I was not sure if I could complete my PhD, buried with stress and worries looking at the unsolved puzzles. Your valuable inputs as well as great patience made this thesis possible, for which I am forever grateful. Chris, thank you for the inspiring discussions and rigorous comments throughout this project. You taught me how to critically look at my own work, and analytically find explanations for the details. I really appreciate all the late night emails with the hand written sketches and equations, your dedication and enthusiasm has inspired me and greatly improved our papers. Ruud, thank you for your valuable guidance and constructive feedback. Thanks for all the comments and notes that followed many presentations and meetings we attended. I still remember the quick talks we had in my first year, which really helped me overcome the early fears I had towards my PhD. It was a wonderful experience to be a TA in your course, touching upon different topics and guiding students on home assignments was fun.

I would also like to thank the supporting staff in TP and PPE. Anita, Fiona, Elly and Caroline, thank you for keeping things well organized. Applying for a visa extension at the last minute was not a smart thing to do, but I am really happy that you made it a quick and smooth process, with all the calls and emails punching the, to me, very complicated system.

I was lucky to be part of both TP and PPE group, benefited from both groups, without having to double my workload. I would like to thank all the people who have contributed to the Journal club, group meetings, science club, lunch lectures, as well as the social activities such as the Friday afternoon drinks, barbeques and movie nights.

In particular I would like to thank a few people here, and please forgive me for not being able to mention everyone. Anton, my OpenFOAM and C++ guru, it is hard to imagine how tough my first year would have been without your kind help, and thanks for all the social activities you have organized. Bernhard, I am thankful for the early morning lec-

tures you gave me about Dutch culture and language, it is a pity that I did not continue learning Dutch, but I see a big possibility in the near future. Duong, I really miss the old days when we were working in the office until late at night and over the weekends, as well as the wonderful spring rolls we had at your place. Michiel, being a webmaster was way easier than I thought, all thanks to your previous contributions and unreserved sharing. David, thanks for all the dinner and poker nights that you organized at your place, and for the many impressive 'look at that' moments. Andrea and Fabio, it was nice to have you in the same project, and I will never forget the many discussions/complains we had in front of the whiteboard. Cees, thanks for being the most reliable source of the TP news and gossips, and for flying all the way north to my hometown. Sid, thank you for all the fantastic stories about art, for taking initiatives for the science club, and for the wonderful Indian dinner. Hrushi, haha, you are the most interesting officemate I have ever met, always enthusiastic and full of surprising ideas. Xiaogang, the afternoon chats we had in your office really helped me to regain new energy, and you introduced to me many wonderful things outside work. Aneekatrien, I really enjoyed all the interesting stories you shared over lunch, and of course all the awesome pies and cookies you brought. Samir, thank you for inviting me to Bremen, the trip along the river was both freezing and amazing. Kevin, I am certainly going to miss the many whiteboard discussions we had, and your impressive drawings. I would also like to thank my other colleagues: Volkert, Pouyan, Laurens, Dries, Rajat, Farzad, Evert, Lilian, Yogesh, Aris, Venky, Barbara, Rudi, Koen, Neils, Durgesh, Dayinta, Floris, Maulik, Hao, Yujie, Shaurya, Josette, Dominik, Anand, Ahad, Gerasimos, Chirag, Manu, Manas, Iman, Amit, Saeid, Snehal, Elin, Xu Fei, Daoming, for all the enjoyable moments we have shared.

6

Finally, I would like to thank my family. 我想感谢我的父母和家人。能生在这个家庭，有你们的陪伴，我已经很幸运了。漫漫求学路，如果没有你们的坚定支持，我不会走到这么远。这份亲情，是我一生不竭的动力和幸福的根源。我要感谢我的妻子，温颖融。无数个深夜里，你我捧着温暖的饭盒共同奋斗的画面，会一直温存于我的记忆里。此生挚爱，刻骨铭心。

CURRICULUM VITÆ

Wenjie JIN

17-02-1987 Born in Yanji, China.

EDUCATION

2006–2010 BSc in Mechanical Engineering
Tsinghua University, China

2010–2012 MSc in Fluid Mechanics
Royal Institute of Technology (KTH), Sweden

2012–2017 PhD. in Chemical Engineering
Delft University of Technology, the Netherlands
Thesis: Modeling of atomic layer deposition on nanoparticle
agglomerates
Promotor: Prof. dr. ir. Chris R. Kleijn and Prof. dr. ir. J. Ruud
van Ommen